

AD 741230

ARPA Order No. 1579 Amend. No. 2 Contract No. H0210008

Program Code No. 1F10

Contractor - Illinois Institute of Technology

Principal Investigator - Dr. James W. Dally

Semi-annual Technical Report

**A Dynamic Photoelastic Investigation of
Stress Wave Propagation in a Half-Plane with
Multiple Dilatational Sources**

Effective Date of Contract: Dec. 28, 1970
Contract Expiration Date: Dec. 28, 1971
Amount of Contract: \$25,900
Principal Investigator: J. W. Dally
(301-454-2410)
Project Scientist: S. S. Khorana
(301-225-9600)

Prepared for

U. S. Department of the Interior

Bureau of Mines

Twin Cities

Minnesota

Reproduced by
NATIONAL TECHNICAL
INFORMATION SERVICE
Springfield, Va. 22151



August 15, 1971

DISCLAIMER NOTICE

THIS DOCUMENT IS THE BEST
QUALITY AVAILABLE.

COPY FURNISHED CONTAINED
A SIGNIFICANT NUMBER OF
PAGES WHICH DO NOT
REPRODUCE LEGIBLY.

Unclassified
Security Classification

3200.8 (Att 1 to Encl 1)
Mar 7, 66

DOCUMENT CONTROL DATA - R & D		
(Security classification of title, body of abstract and indexing annotation must be entered when the overall report is classified)		
1. ORIGINATING ACTIVITY (Corporate author)		2a. REPORT SECURITY CLASSIFICATION
Illinois Institute of Technology 3300 South Federal Street Chicago, Illinois 60616		Unclassified
3. REPORT TITLE		2b. GROUP
A Dynamic Photoelastic Investigation of Stress Wave Propagation in a Half-Plane with Multiple Dilatational Sources		
4. DESCRIPTIVE NOTES (Type of report and inclusive dates)		
Semi-annual Technical Report		
5. AUTHOR(S) (First name, middle initial, last name)		
James W. Dally, S. S. Khorana		
6. REPORT DATE	7a. TOTAL NO. OF PAGES	7b. NO. OF REFS
August 15, 1971	122	7
8a. CONTRACT OR GRANT NO.	9a. ORIGINATOR'S REPORT NUMBER(S)	
H0210008	H0210008 - 1	
b. PROJECT NO.	9b. OTHER REPORT NO(S) (Any other numbers that may be assigned this report)	
1579		
c. Program Code 1F10		
d. Work Unit No. F53118		
10. DISTRIBUTION STATEMENT		
Distribution of this document is unlimited.		
11. SUPPLEMENTARY NOTES		12. SPONSORING MILITARY ACTIVITY
		Advanced Research Projects Agency 1400 Wilson Boulevard Arlington, Virginia 22209
13. ABSTRACT		
<p>A dynamic photoelastic study of stress waves generated by multiple dilatational sources in a half plane is described. The model material is CR-39 and lead azide charges are used to produce the dilatational waves. Fringe patterns are recorded by a multiple spark gap camera.</p> <p>Interactions between the waves before and after reflection from the free surface are studied. In the pre-reflection period, the incident dilatational wave tails reinforce and produce important tensile stresses along the center-line joining adjacent sources. Important features in the post-reflection phase include the interaction between incident and reflected dilatational waves, the generation and propagation of shear waves, interaction between shear waves and finally the interaction of the shear wave with the cracked region around source locations. The effect of varying the distance between sources and their depth below the free surface is investigated in some detail.</p>		

DD FORM 1473

Unclassified

Unclassified

Security Classification

3200.8 (Att 1 to Encl 1)
Mar 7, 66

14. KEY WORDS	LINK A		LINK B		LINK C	
	ROLE	WT	ROLE	WT	ROLE	WT
<p>Photoelasticity Multiple dilatational sources Stress waves Multiple spark gap camera Fringe patterns Modeling Explosives</p>						

Unclassified

Security Classification

ARPA Order No. 1579 Amend. No. 2 Contract No. H0210008

Program Code No. 1F10

Contractor - Illinois Institute of Technology

Principal Investigator - Dr. James W. Dally

Semi-annual Technical Report

A Dynamic Photoelastic Investigation of
Stress Wave Propagation in a Half-Plane with
Multiple Dilatational Sources

by J. W. Dally and S. S. Khorana

Prepared for
U. S. Department of the Interior
Bureau of Mines
Twin Cities
Minnesota



August 15, 1971

Sponsored by
Advanced Research Projects Agency
ARPA Order No. 1579, Amendment No. 2
Program Code No. 1F10

This research was supported by the
Advanced Research Projects Agency
of the Department of Defense and
was monitored by Bureau of Mines
under Contract No. H0210008

The views and conclusions contained in this document are those of the
authors and should not be interpreted as necessarily representing the
official policies, either expressed or implied, of the Advanced Research
Projects Agency or the U.S. Government.

TABLE OF CONTENTS

	Page
ABSTRACT	v
LIST OF TABLES	vii
LIST OF ILLUSTRATIONS	viii
 SECTION	
I. INTRODUCTION	1
II. EXPERIMENTAL PROCEDURE	6
Model Material	
Model Geometry	
High Speed Photographic Recording System	
Synchronization	
III. PHOTOELASTIC RESULTS: PRE-REFLECTION PERIOD. .18	
Propagation of the Incident P Wave	
Interaction of Two Dilatational Waves	
Conclusions (Pre-reflection period)	
IV. PHOTOELASTIC RESULTS: POST-REFLECTION PERIOD .41	
Stress Wave Reflection Due to a Single Dilata-	
tional Source in a Half-Plane ($h/\lambda = 1$ and	
2).	
Stress Wave Reflection Due to a Pair of Dila-	
tational Sources in a Half-Plane ($h/\lambda = 2$).	
Stress Wave Reflection Due to Three Dila-	
tational Sources in a Half-Plane ($h/\lambda = 2$).	
Stress Wave Reflection Due to a Pair of Dila-	
tational Sources in a Half-Plane ($h/\lambda = 1$).	
Stresses Along the Free Boundary	

V. CONCLUSIONS AND RECOMMENDATIONS.	104
APPENDIX	
A. FRINGE PATTERNS.	109
BIBLIOGRAPHY.	122

ABSTRACT

A dynamic photoelastic study of stress waves generated by multiple dilatational sources in a half plane is described. The model material is CR-39 and lead azide charges are used to produce the dilatational waves. Fringe patterns are recorded by a multiple spark gap camera.

Interactions between the waves before and after reflection from the free surface are studied. In the pre-reflection period, the incident dilatational wave tails reinforce and produce important tensile stresses along the centerline joining adjacent sources. Important features in the post-reflection phase include the interaction between incident and reflected dilatational waves, the generation and propagation of shear waves, interaction between shear waves and finally the interaction of the shear wave with the cracked region around source locations. The effect of varying the distance between sources and their depth below the free surface is investigated in some detail. Recommendations are made to extend this type of study to cover the interaction between the stress waves and the moving cracks by utilizing highly brittle birefringent models.

LIST OF TABLES

Table		Page
I.	Typical Properties for Three Different Rock Materials.	2
II.	Properties of CR-39	8
III.	Comparison of Maximum Fringe Orders in The PS _L , PS _R and the Combined PS _L + PS _R Waves (for $h/\lambda = 1$, $S = 2$).	83

LIST OF ILLUSTRATIONS

Figure	Page
2.1 Model Geometry.....	7
2.2 Fringe Patterns Showing Stress Waves in CR-39 and Homalite - 100.....	9
2.3 Schematic Drawing of Model.....	10
2.4 Multiple Spark Gap Camera.....	13
2.5 The Optical System.....	14
2.6 Control Circuits.....	17
3.1 Photoelastic Fringe Patterns Showing Wave Propaga- tion from a Single Source.....	19
3.2 Fringe Order as a Function of Position and Time. ($h/\lambda = 1$, $S/\lambda = 0$).....	21
3.3A Fringe Patterns Illustrating Interaction of P Waves (frames 1, 2 and 3).....	23
3.3B Fringe Patterns Illustrating Interaction of P Waves (frames 4, 5 and 6).....	24
3.4 Fringe Superposition Along the Centerline.....	26
3.5 Reinforcement of Fringe Patterns Along the Center- line ($h = 2$ in., $S = 4$ in.).....	27
3.6 Fringe Order as a Function of Position ($h/\lambda = 2$, $s/\lambda = 2$).....	29
3.7 Fringe Order as a Function of Position ($h/\lambda = 1$, $S/\lambda = 2$).....	31
3.8 Fringe Order at Center-Point Between Sources as a Function of Time.....	32

Figure	Page
3.9 Fringe Order as a Function of Position Along η ($h/\lambda = 2$, $S/\lambda = 2$).....	34
3.10 Fringe Order as a Function of Position Along η ($h/\lambda = 2$, $S/\lambda = 3$).....	36
3.11 Fringe Pattern Illustrating Low-Level Reinforce- ment when $S/\lambda \geq 4$	37
3.12 Fringe Order N_{MAX} along η as a Function of Time...	38
3.13 Fringe Patterns Indicating Influence of Free Boundary Reflections on Fringe Peaks Along the η Line.....	40
4.1 Early Interval in the Reflection of an Incident P Wave.....	43
4.2 Fringe Order as a Function of Position Along Vertical through Source ($h/\lambda = 2$, $S/\lambda = 0$).....	44
4.3 Mid-interval in the Reflection of an Incident P Wave.....	46
4.4 Fringe Order as a Function of Position Along Vertical through Source ($h/\lambda = 1$, $S/\lambda = 0$).....	47
4.5 Fringe Patterns Representing the Reflected Shear (PS) Wave.....	49
4.6 Fringe Order as a Function of Position x for the PS Wave ($h/\lambda = 1$, $S/\lambda = 0$, $d = 0.3$ in.).....	51
4.7 Fringe Order as a Function of Position x for the PS Wave ($h/\lambda = 1$, $S/\lambda = 0$, $d = 1.0$ in.).....	52
4.8 Fringe Order as a Function of Position x for the PS Wave ($h/\lambda = 2$, $S/\lambda = 0$, $d = 0.3$ in.).....	53

Figure	Page
4.9 Fringe Order as a Function of Position κ for the PS Wave.....	54
4.10A Pre-Reflection Reinforcement of the Incident P Wave ($h/\lambda = 2$, $S/\lambda = 1$).....	56
4.10B Post-Reflection Reinforcement ($h/\lambda = 2$, $S/\lambda = 1$)..	57
4.11 Fringe Order as a Function of Position Along Vertical Centerline before and after Reflection ($h/\lambda = 2$, $S/\lambda = 1$).....	58
4.12 Final Stages of the Reflection of the Reinforced P Waves with $S/\lambda = 1$	60
4.13A Reflection Behavior for the Model with $h/\lambda = 2$ and $S/\lambda = 2$ (frames 4 and 7).....	61
4.13B Reflection Behavior for the Model with $h/\lambda = 2$ and $S/\lambda = 2$ (frames 8 and 9).....	63
4.14 Rapid Attenuation of the Fringe Maxima along the Centerline.....	64
4.15 Fringe Order as a Function of Position ($h/\lambda = 2$, $S/\lambda = 2$, $d = 0.3$ in.).....	65
4.16 N_{MAX} as a Function of Position in the Region Near the Boundary.....	67
4.17 Representation of the Early Phase Response of the Model with Three Sources.....	69
4.18 Representation of the Late Phase Response of the Model with Three Sources.....	70
4.19 Fringe Order as a Function of Position x for the Three Source Model.....	72

Figure	Page
4.20A Early Portion of the Reflection Process with $h/\lambda = S/\lambda = 1$ (frames 6 and 9).....	74
4.20B Early Portion of the Reflection Process with $h/\lambda =$ $S/\lambda = 1$ (frames 10 and 11).....	75
4.21 Late Portion of the Reflection Process with $h/\lambda =$ $S/\lambda = 1$	76
4.22 Fringe Order as a Function of Position Along a Line Below the Boundary ($h/\lambda = S/\lambda = 1$).....	78
4.23 Distribution of the Fringe Order Along the Ridge Line of a PS Wave.....	80
4.24 Interacting Shear Waves with $h/\lambda = 1$ and $S/\lambda = 2$.	82
4.25 Reinforcement of the P, PP and PS Waves.....	84
4.26 PS Wave Interaction with the Sources.....	86
4.27 Reinforcement of P, PP and PS Waves with $S/\lambda = 3$.	87
4.28 Interaction of PS_L and PS_R Waves.....	88
4.29 Fringe Order as a Function of Position Along the Vertical Centerline ($h/\lambda = 1, S/\lambda = 3$).....	89
4.30 Comparison of Stresses Along the PS Waves.....	91
4.31 Maximum Fringe Order as a Function of Position. ($h/\lambda = 1, S/\lambda = 1, 2$ and 3).....	93
4.32 Fringe Order as a Function of Position Along the Boundary for $h/\lambda = 1, S/\lambda = 0$	94
4.33 Fringe Order as a Function of Position Along the Boundary for $h/\lambda = 2, S/\lambda = 0$	96
4.34 Fringe Order as a Function of Position Along the Boundary for $h/\lambda = 1, S/\lambda = 1$	97

Figure	Page
4.35 Fringe Order as a Function of Position Along the Boundary for $h/\lambda = 1$, $S/\lambda = 2$	99
4.36 Fringe Order as a Function of Position Along the Boundary for $h/\lambda = 1$, $S/\lambda = 3$	100
4.37 Influence of Parameters h/λ and S/λ on Maximum Stress at Point 0.....	102
4.38 Fringe Order as a Function of Position Along the Boundary for $h/\lambda = 2$, $S/\lambda = 2$	103
A-1 $h = 2"$, $S = 0$	110
A-2a $h = 2"$, $S = 2"$	111
A-2b $h = 2"$, $S = 2$	112
A-3 $h = 2"$, $S = 4"$	113
A-4 $h = 2"$, $S = 6"$	114
A-5 $h = 4"$, $S = 0"$	115
A-6 $h = 4"$, $S = 2"$	116
A-7 $h = 4"$, $S = 4"$	117
A-8 $h = 4$, $S = 6"$	118
A-9 $h = 4"$, $S = 8"$	119
A-10 $h = 4"$, $S = 10"$	120
A-11 $h = 4"$, $S_1 = S_2 = 2"$	121

1. INTRODUCTION

In the United States almost all of the metallic ores and rock aggregates are produced in open-pit operations and most of this material must be removed by blasting. The blasting techniques employed are extremely important since they markedly effect the economy and the safety of the operation. Since bore-hole layout design and the calculation of explosive charges control both the safety and economy of blasting it is imperative that the theory of blasting be improved as much as is possible.

To improve blasting techniques, it is necessary to establish the dynamic stress state which the explosives produce, to follow the stress wave propagation during the dynamic event, to note the initiation of cracks and the subsequent propagation of the cracks and finally to observe the interaction of the propagating cracks and stress waves.

Dynamic photoelasticity provides an experimental approach to study these dynamic phenomena. With dynamic photoelasticity whole field records of stress waves are obtained which give an outstanding visual display of the event at preselected times. One of the most fundamental dynamic problems related to the theory of blasting is the description of dilatational wave or waves generated at internal sources in a half-plane. As the reflection phenomena and the interaction due to multiple sources is extremely complex, the whole field data provided by photoelasticity is important in establishing an understanding

of the significant wave interactions.

In rock blasting the chemical energy of a concentrated explosive contained in a relatively small diameter bore hole is utilized to fragment the rock. The explosive is transformed into a gas with enormous pressures which exceed 10^5 bars [1.1]*. This high pressure shatters the rock in the area adjacent to the bore hole; however, this crushed area is surprisingly small being about the same in radial size as the original radius of the bore hole.

A dilatational type stress wave propagates radially away from the bore hole with a velocity which depends on the elastic constants of the rock material. Characteristic velocities of propagation for three common rock types are shown in Table 1.

Table 1. Typical Properties for Three Different Rock Materials

Rock Type	Dilatational Velocity ft/sec	Compressive Strength (psi)	Tensile Strength (psi)	Strength Ratio
Granite	11,400	28,000	110	68
Limestone	16,200	10,000	800	38
Sandstone	9,600	18,000	310	23

(after J.S. Macdonald, 1.2)

The state of stress associated with this outgoing dilatational wave is oscillatory with initial compression in the leading

* For all numerical references, see bibliography.

pulse and biaxial* tension in the first trailing pulse. These tensile stresses in the trailing pulse produce a system of radial cracks which extend for a few feet from the bore hole. The breakage in this first stage is limited as the stresses in the pulse attenuate rapidly with distance of propagation and some energy is lost by creating the fractures and by inelastically deforming the rock. In the absence of a free face, the stress wave propagates away from the source without further fracture.

With a free face of rock which is normally near the drill hole and parallel to its axis a second mode of breakage occurs. This breakage is due to scrubbing a layer of rock adjacent to the free face. The scrubbing mechanism is due to the reflection of the incident compression pulse from the free boundary. During the reflection process, the incident dilatational wave is converted into reflected dilatational and shear waves. In the reflected dilatational wave, the state of stress is biaxial tension and in the reflected shear wave the shear stress converts to a state of pure shear with $p_1 = -p_2$.

Both of these reflected waves can produce tensile stresses sufficiently large for fractures to occur. At the state of stress which induces fracture is a superposition of the incident dilatational and the two reflected waves, the net tensile stress occurs some distance away from the face

* Biaxial refers to the radial and circumferential directions.

and rock removal is in the form of layers.

The scabbing mechanism is important since rock exhibits a much higher compression strength than tensile strength. Strength ratios shown in Table 1 indicate that compressive strengths exceed tensile strengths by factors ranging from 25 to 68. Thus large amounts of energy can be carried by the dilatational wave far from the source in the compression pulse. Upon reflection, a significant portion of this energy is available in tensile pulses of sufficient amplitude to produce fractures adjacent to the face. Indeed, if the incident compression wave is of sufficient magnitude and duration, multiple scabbing can occur with removal of several layers of rock.

The role of stress waves clearly plays an important role in the construction of rock; however, extensive and detailed treatments of the dynamic aspect of stress near the free face has not been made. This study considers the problem of stress wave reflection from a free boundary and covers the region from a given distance prior to the onset of the compressional pulse to the onset of the reflected pulse, which includes the selection of the initial material, definition of initial conditions and the photographic recording system is described in Section 2 of this report. The analysis of the data is divided into two parts with the first part, covered in Section 3, covering the pre-reflection portion. In this portion, the interaction of the dilatational waves from multiple internal sources is examined as a function of the choice

spacing parameter s/λ . The second part of the data analysis, which is treated in Section 4, deals with the post reflection period for models containing one, two and three dilatational sources. Reflected wave forms are identified and several of the more important reinforcement processes are examined in detail. Finally, conclusions are drawn which pertain to the geometric parameters h/λ and s/λ for the design of a row of explosive charges, and recommendations are made to continue the study of the application of dynamic stress and fracture analysis to mining technology.

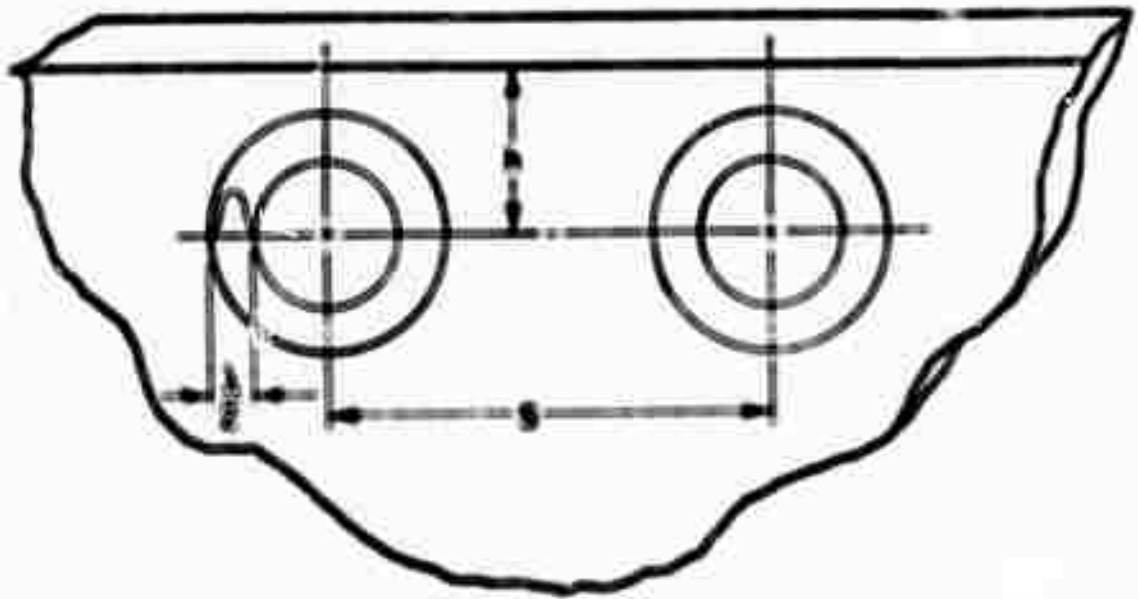
II. EXPERIMENTAL PROCEDURE

The experimental procedure involves the application of dynamic photoelasticity to problems of stress wave propagation related to mining technology. In the applications considered here, the procedure is the same for all cases. A two-dimensional model of the half plane is fabricated according to Fig. 2.1. The model is loaded by detonating one or more small explosive charges. The photoelastic fringe patterns representing the stress wave propagation are recorded using a high-speed photographic system especially designed for dynamic photoelastic applications. A brief description of each experimental unit is presented in subsequent subsections.

2.1 Model Material

The models were fabricated from large sheets $1/4 \times 24 \times 36$ in. of Columbia Form (CR-39). The utilization of this material for dynamic photoelasticity has been investigated by A. D. J. Clark [2.1] and several applications have been made by Dally and his associates. [2.2, 2.3, 2.4] The material is quite suitable for this investigation since it is readily available at a reasonable cost in the form of large flat sheets with surfaces of optical quality.

The low fracture strength of (CR-39) is a significant advantage in the current investigation. On detonation, the explosive produces a very high pressure which shatters the hole. The fracture is quite extensive when thousands



TEST NO.	h (m)	S (m)	NO. OF CHARGES
1	2	0	1
2	2	2	2
3	2	4	2
4	2	6	2
5	4	0	1
6	4	2	2
7	4	4	2
8	4	6	2
9	4	8	2
10	4	10	2
11	4	2	3

FIG. 2-1 MODEL GEOMETRY

of cracks uniformly distributed about the hole. Due to the symmetry of the fracture only a dilatational wave is produced and moreover the intensity of the dilatational wave is essentially independent of θ .

Some initial experiments were conducted with Nomalite 100, a polyester with high strength and toughness. In this material, the extent of fracture about the hole containing the charge was much less and the symmetry of the fracture pattern was not maintained. As a consequence both dilatation P and shear S waves were generated. An example of the incident stress waves produced in CR-39 and in Nomalite 100 is illustrated by the photoelastic patterns in Fig. 2.2.

The properties of CR-39 are tabulated below:

Table II. Properties of CR-39

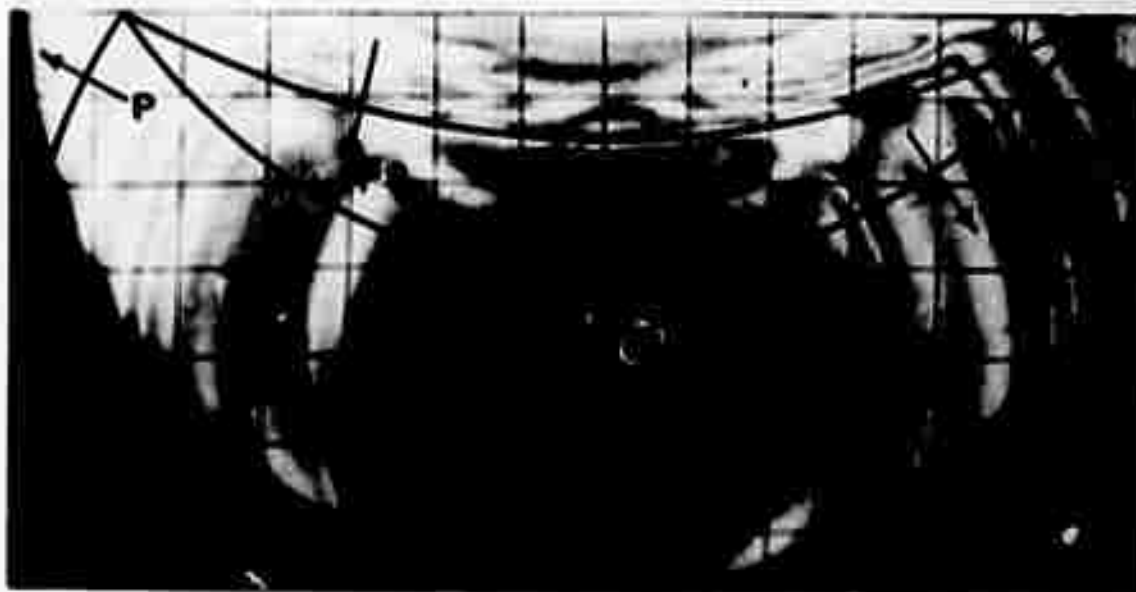
Specific Weight	ρ	1.39
Modulus of Elasticity (dynamic)	E_d	525,000 psi
Poisson's Ratio (dynamic)	ν_d	0.31
Tensile Strength	σ_u	5000-7000 psi
Material Fringe Value (dynamic)*	f_d	110 psi-in/fringe

* for light with a wave length of 5000 Angstroms

2.2 Model Geometry

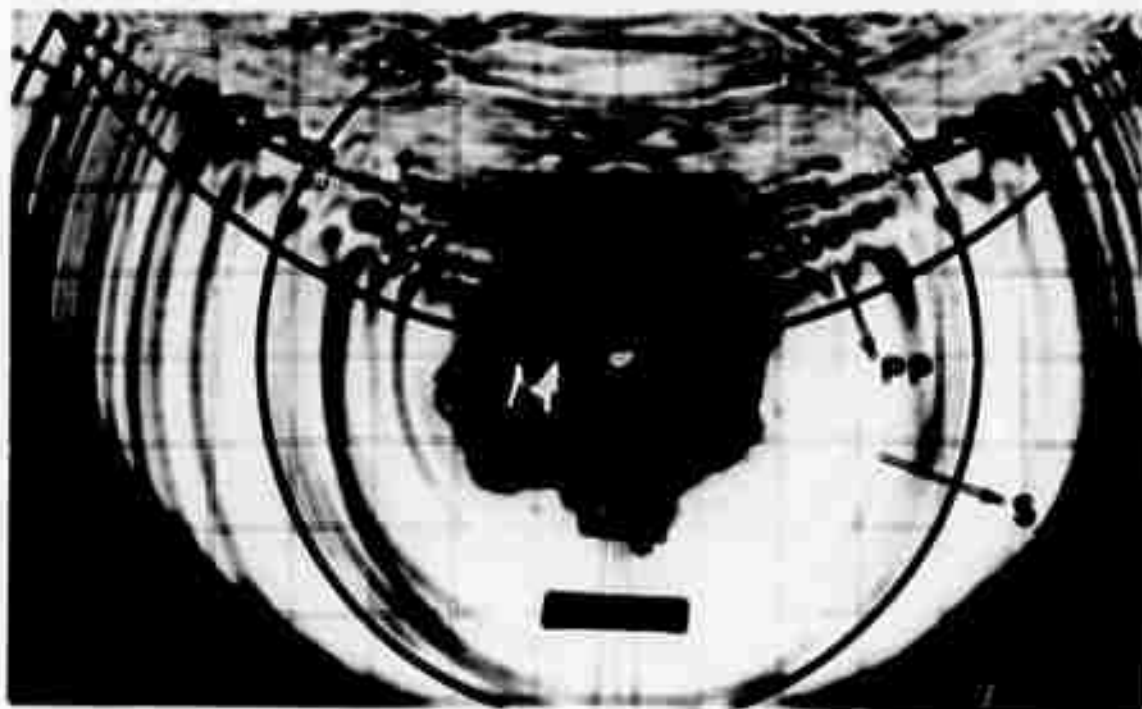
The model fabricated from a sheet of CR-39 $1/4 \times 24 \times 36$ " is shown schematically in Fig. 2.3. Several considerations determine the dimensions of the model. First, the thickness must be sufficiently small compared to the com-

$t=92$ microsec.



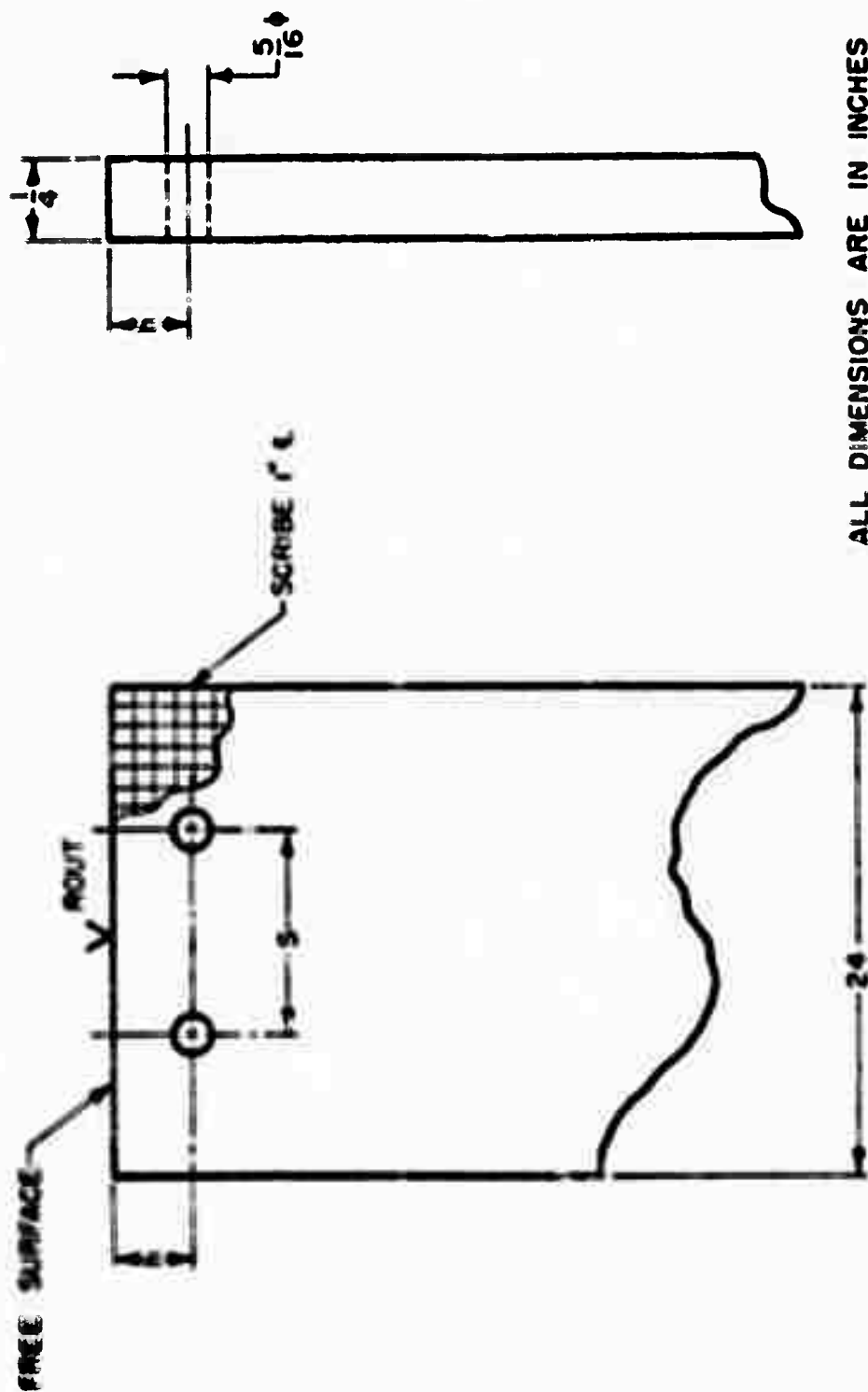
$t=92$ microsec.

$t=92$ microsec.



$t=92$ microsec.

Fig. 2.2 Fringe patterns showing stress waves in GaAs and Si (100)



ALL DIMENSIONS ARE IN INCHES
(NOT TO SCALE)

FIG. 2-3 SCHEMATIC DRAWING OF MODEL.

nate wave length λ of the stress pulse, so that the generalized plane stress approximation is valid. Also, the thickness must be large enough to provide an adequate photoelastic response. Finally, the lateral dimensions of the model are made large enough to eliminate reflections from non-essential boundaries during the period of observation.

The free surface of the half-plane was made by routing one edge of the model. The explosive was packed in 5/16 in. diameter holes drilled through the thickness of the CR-39 plate. The diameter was selected to give sufficient volume to tightly pack one bridge wire and 200 mg. of lead azide. The distance from the hole center to the free boundary was h , the distance between the hole was S and the width of the leading stress pulse was half the dominate wave length $\lambda/2$. Values of h selected were 2 and 4 while S was varied between 2 and 10 inches. The dominate wave length produced by the explosive charge was about $\lambda = 2$ inches. A rectangular grid was scribed on the model on one inch centers.

The lead azide explosive charge was 200 mg. for each source. This quantity was sufficient to produce a significant fracture zone about the hole in the CR-39 model and to generate a symmetrical outgoing dilatational wave. The explosive was ignited with a bridge wire (0.001 inches in diameter - 1/8 in. long of constantan) which was energized with a 5000 VDC - 62 joule firing pulse.

When detonating multiple charges, where it is important to obtain simultaneous ignition, it is necessary to match the resistance of the bridge wires to the third significant figure. If this matching is accomplished, the two charges can be detonated with less than one microsecond delay time between charges. The jitter time between activating the firing circuit and detonating the charges ranges from about 2 to 5 μ sec. The jitter time is minimized by reducing the bridge wire resistance which in turn increases the power dissipated across the wire.

2.3. The High Speed Photographic Recording System

In this phase of the investigation, a multiple spark gap camera^[2.5, 2.6, 2.7] was used to record the dynamic photoelastic fringe patterns produced in the half-plane models. This camera shown in Fig. 2.4 is capable of 16 frames and can be operated at framing rates which can be varied in discrete steps from 30,000 to 800,000 frames/sec. The resolution of the camera is a function of the fringe gradient and fringe velocity. Experiments indicate that gradients of 20 fringes/in. with velocities of 75,000 in./sec. represent the upper limit of the camera's resolution capability.

The optical system of the camera which is illustrated schematically in Fig. 2.5 performs three basic functions: polarization, image separation and magnification. The optical elements include a field lens (18 in. diameter with

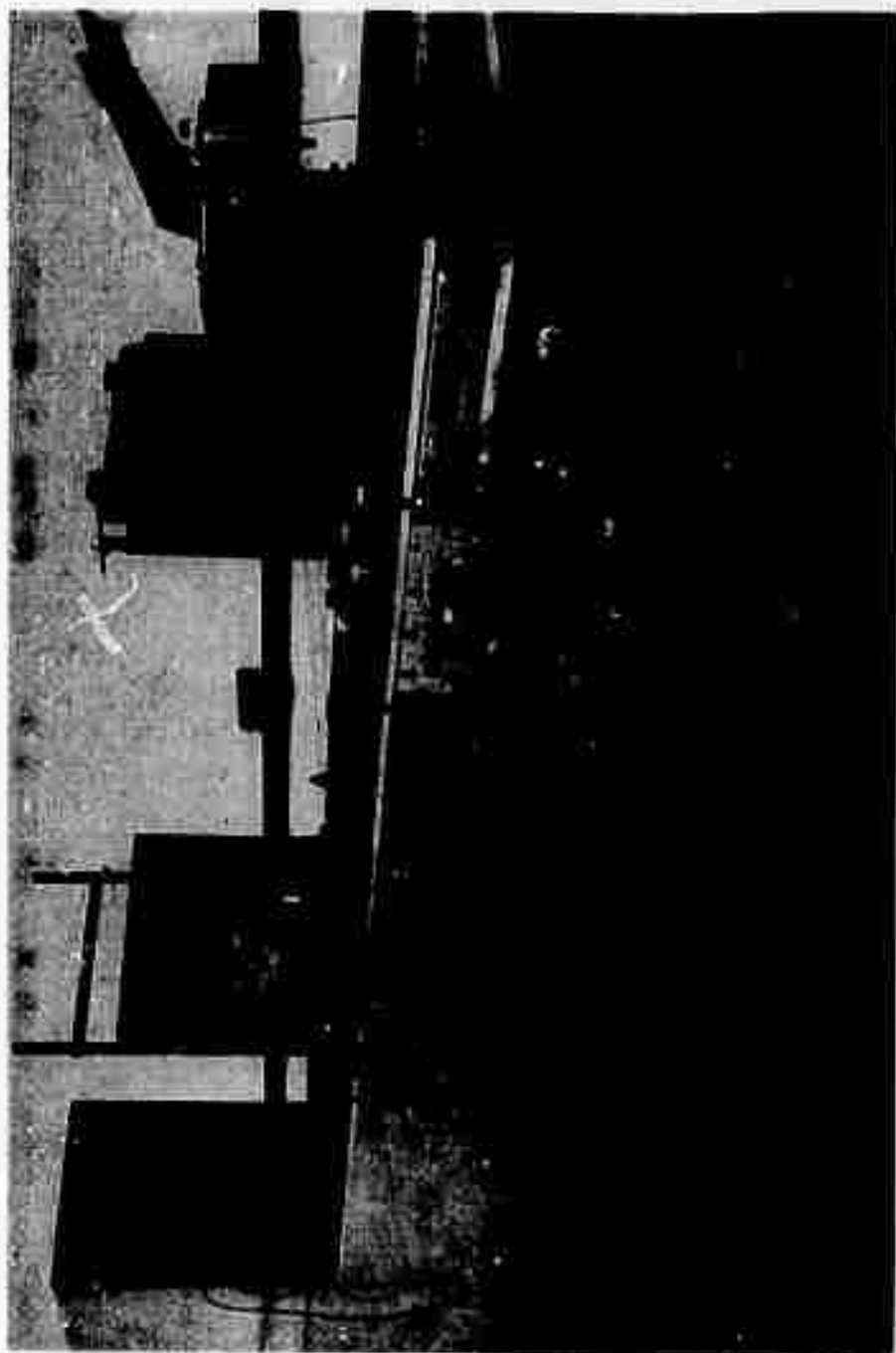


Fig. 2.4 Multiple Spark Gap Camera

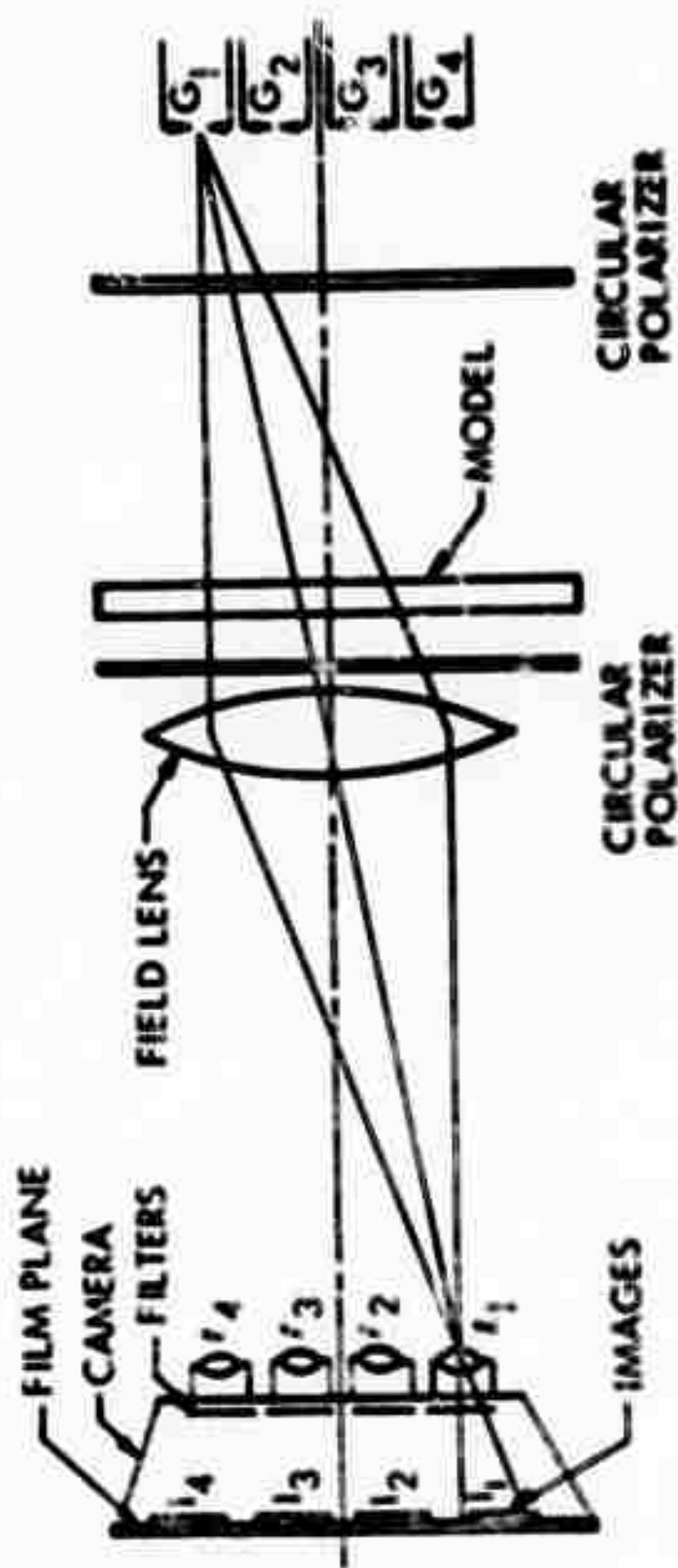


FIG. 2-5 THE OPTICAL SYSTEM

a focal length of 30 in.) and sixteen camera lenses each with focal lengths of 6.4 inches. Image separation is accomplished by positioning the spark-gaps and camera lenses relative to the optical axis of the bench. Magnification of the optical system is determined primarily by the focal lengths of the field and camera lenses and their relative spacing. In this instance the magnification factor was ≈ 0.12 which gave a 2.2 in. diameter image corresponding to the 18 in. diameter field.

A simple yet effective light-field polar scope is incorporated into the system by utilizing two circular polarizers (MCP-30) between the spark-gap light source and the field lens.

The film selected for recording the image was Kodak Gyrate Positive. This film has a relatively slow emulsion (ASA Tungsten-8) with a fine grain structure and is used extensively in the graphic arts. As it is sensitive to light between 3100 and 5100 angstroms (i.e., the blue region) and the output of the spark gaps peak in this region, its apparent speed is much higher than the ASA speed rating indicates. The film was employed with a Kodak K-2 filter which absorbs most of the light with wave lengths below 4900 angstroms. The combination of the film and filter yields a band width from 4900 to 5100 angstroms which is sufficiently narrow to approximate monochromatic light in dynamic photoelastic applications.

2.4. Synchronization

The initiation and the recording of the dynamic event was controlled by employing the synchronization circuit presented in Fig. 2.6. The event is initiated by the operator by activating switch S on the firing circuit. The firing circuit then simultaneously emits three pulses. The first is a 5kV pulse which ignites the lead aside, the second, a 50 V pulse, activates a time delay generator and the third, another 50 V pulse, triggers an oscilloscope.

At the end of the pre-selected delay interval the delay generator issues an output pulse which is amplified by a trigger module to about 20 kV. This amplified pulse is applied to the third electrode of the trigger gap causing it to ionize and initiate the firing sequence in the multiple spark-gap camera.

The light output from the spark-gaps is sensed by a high frequency photocell (EGG-Lite Mike). The voltage output from the photocell is recorded on the sweeping oscilloscope and an Intensity-Time trace is obtained which established the time during the event when each of the 16 photographs was exposed.

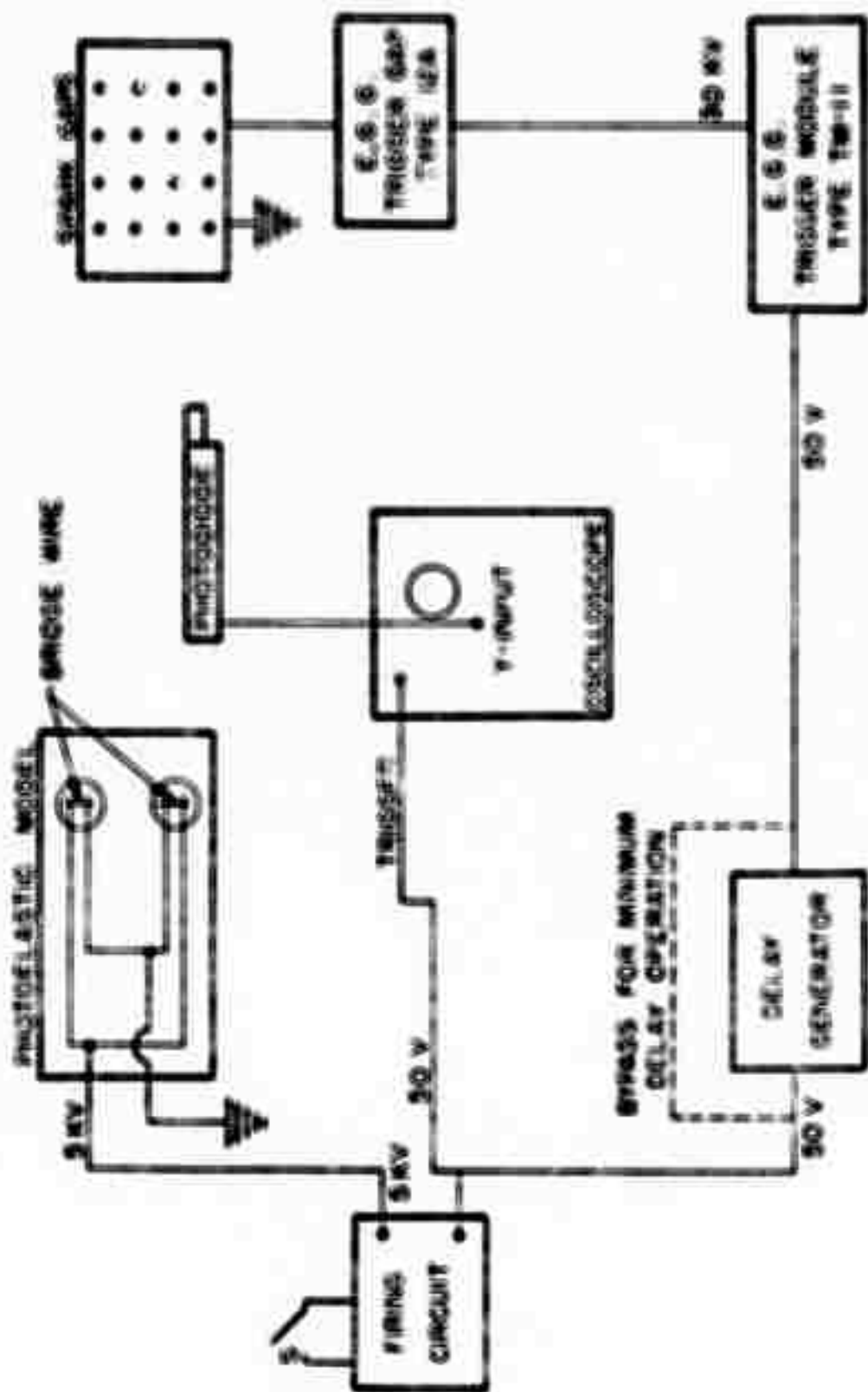


FIG. 2.5 CONTROL CIRCUITS

III. PHOTOELASTIC RESULTS: PRE-REFLECTION PERIOD

The dynamic photoelastic fringe patterns associated with each of the eleven experiments defined in Fig. 2.1 are shown in Figs. A-1 to A-11 in the Appendix A. As this body of data contains 176 individual fringe patterns, it is evident that a significant effort was involved in the data analysis. To facilitate the presentation of the data analysis, the dynamic event will be divided into two different portions. The first is related to the pre-reflection period where the dynamic event initially involves the generation and propagation of a single dilatational wave. Also involved is the interference of two dilatational waves generated from two internal sources.

The second portion of the data analysis is related to the post-reflection period where reflected dilatational and shear waves interact with the incident dilatational wave to produce very complex stress fields in the local region near the boundary.

The pre-reflection period is treated in this section and the post reflection period is covered in section 4.

3.1. Propagation of the Incident P Wave

The photoelastic representation of a dilatational P stress wave propagating from a single source to the free boundary of a half plane is shown in Fig. 3.1. Four fringe patterns are

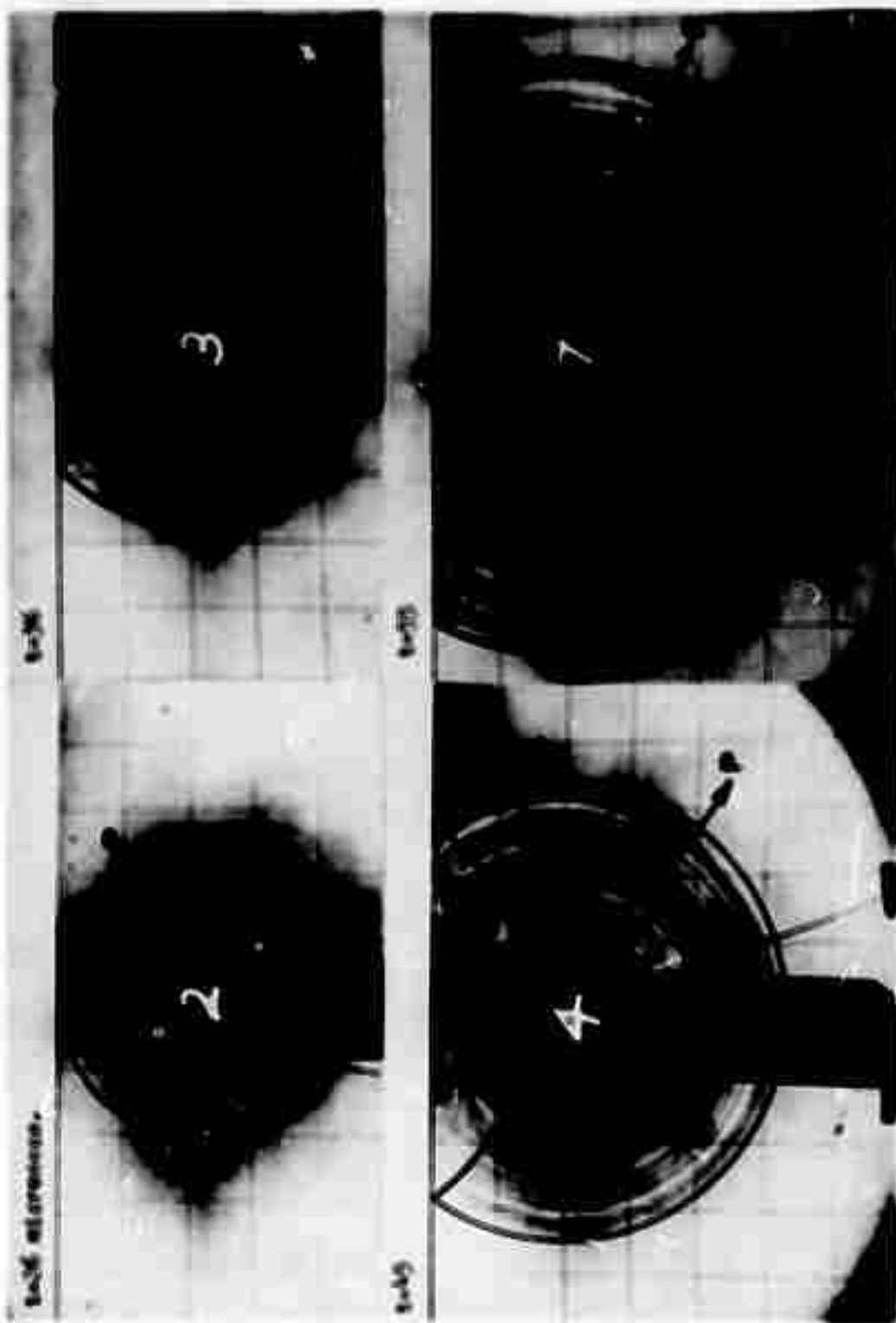


Fig. 3.1 Electrical Fire Damage Showing Wire Insulation from a Single Source

presented to illustrate the features of this event. The photoelastic fringe pattern in frame 2, shows concentric circular fringes corresponding to the outgoing P wave before boundary interaction. The stress optic law (3.1)

$$\sigma_1 - \sigma_2 = N f_c / h \quad (1)$$

where $\sigma_1 - \sigma_2$ is the principal stress difference

N is the order of the fringes

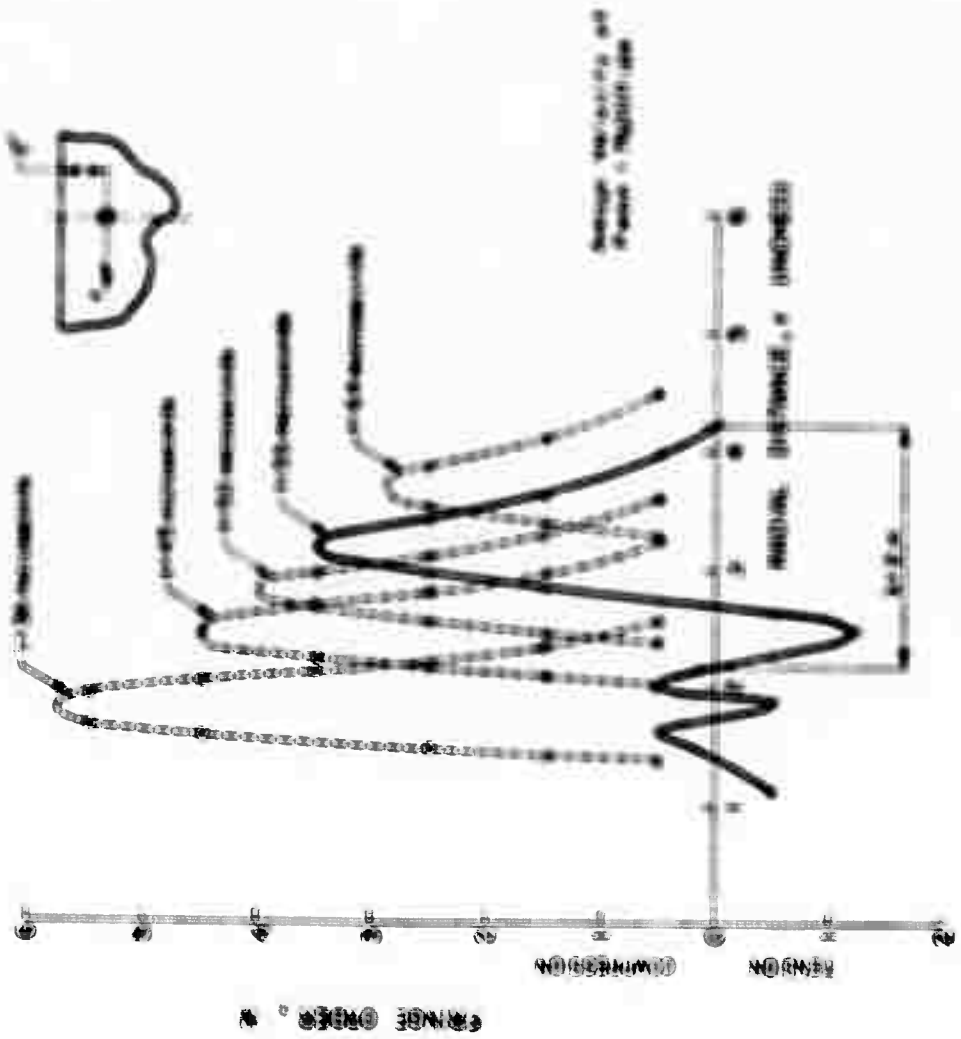
f_c is the material fringe value

h is the model thickness

gives a relation between the optical response (in terms of the order of interference of the fringe) and the principal stress difference in the plane of the model. The outgoing P wave in this fringe packet can be characterized by the graph showing fringe order as a function of the radial position r given in Fig. 3.2. As the fringe packet propagates out into the model, the peak fringe order attenuates from 5.75 fringes at 36 μ sec to 2.9 fringes at 64 μ sec. The stresses in this leading pulse are biaxial compression; however, a secondary pulse is evident in frame 7 at $t = 60 \mu$ sec. The stresses in this trailing pulse are biaxial tension. The velocity of the fringes as they propagate into the model is 76,000 in/sec. The characteristic wave length λ as shown in Fig. 3.2 is about 2 inches.

Returning now to Fig. 3.1, it is clear that the reflection process is beginning in frame 3 and 4 with the reflected

Figure 1. The effect of the concentration of the solution on the rate of the reaction.



dilatational wave PP predominate in this early stage. However, the magnitude of the reflected PP wave is not large and its influence on the fringe pattern is quickly diminished. The second reflected wave, the shear or PS wave clearly identified in frame 7 is the predominate reflected wave.

When the photoelastic pattern is due entirely to a shear wave, the state of stress is pure shear with $\sigma_1 = -\sigma_2$. In this case, the stress optic law of Eq. (1) reduces to:

$$\sigma_1 = -\sigma_2 = \frac{\Delta f_d}{2N} \quad (2)$$

and the individual values of the principal stresses σ_1 and σ_2 can be determined directly.

It is also important to note that the state of stress associated with the shear wave is biaxial with one component compressive and the other tensile. It is this tension component which produces the spallation and fragmentation so important in quarry operations.

3.2. Interaction of Two Dilatational Waves

The important aspect of the interaction between two dilatation waves is the reinforcement which occurs before any significant reflection with the free boundary of the half plane occurs. A typical example of the reinforcement phase of the two source dynamic event is shown in Fig. 3.3A and 3.3B. The two P waves are just beginning to interact in frame 1 and they quickly reinforce each other to produce the

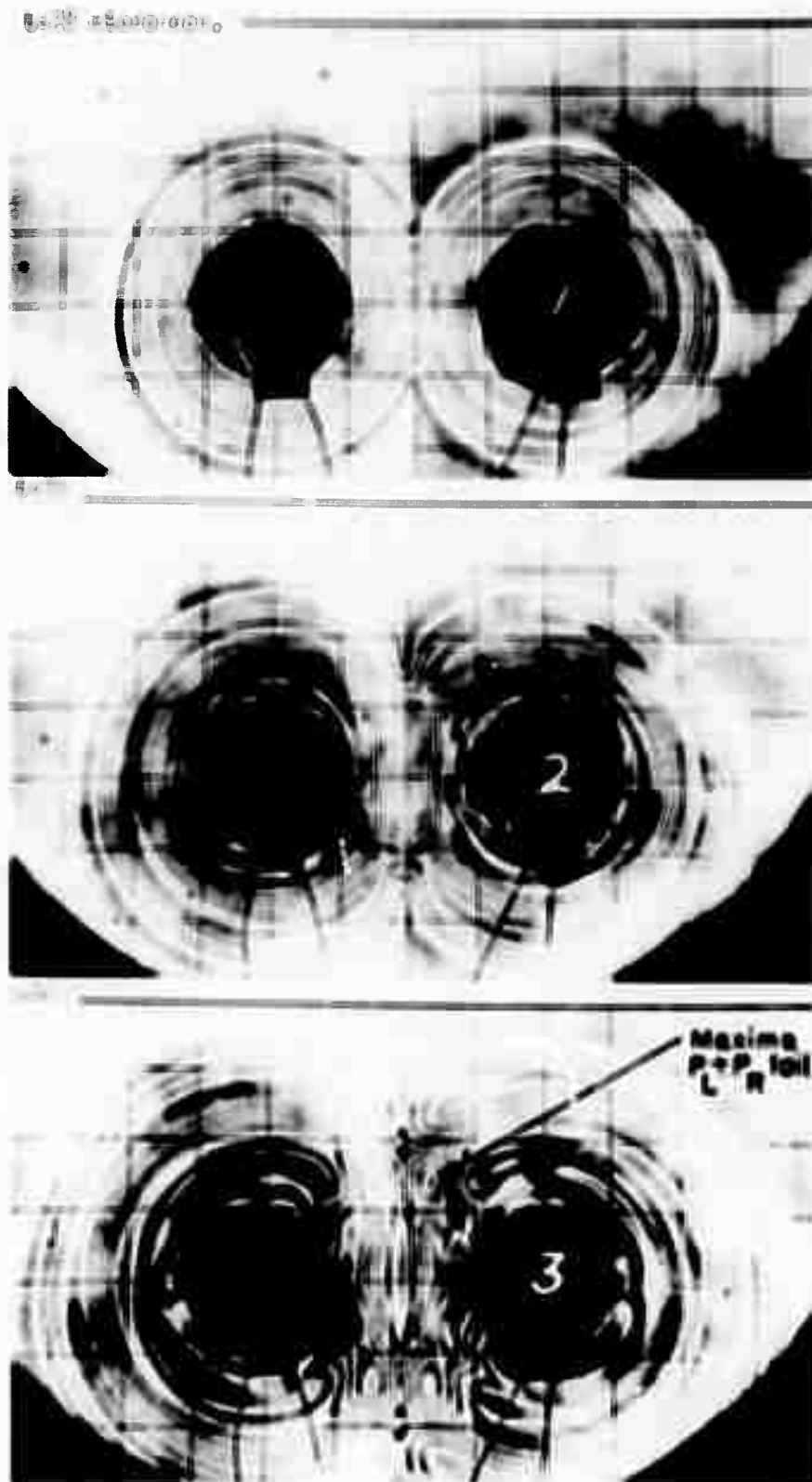
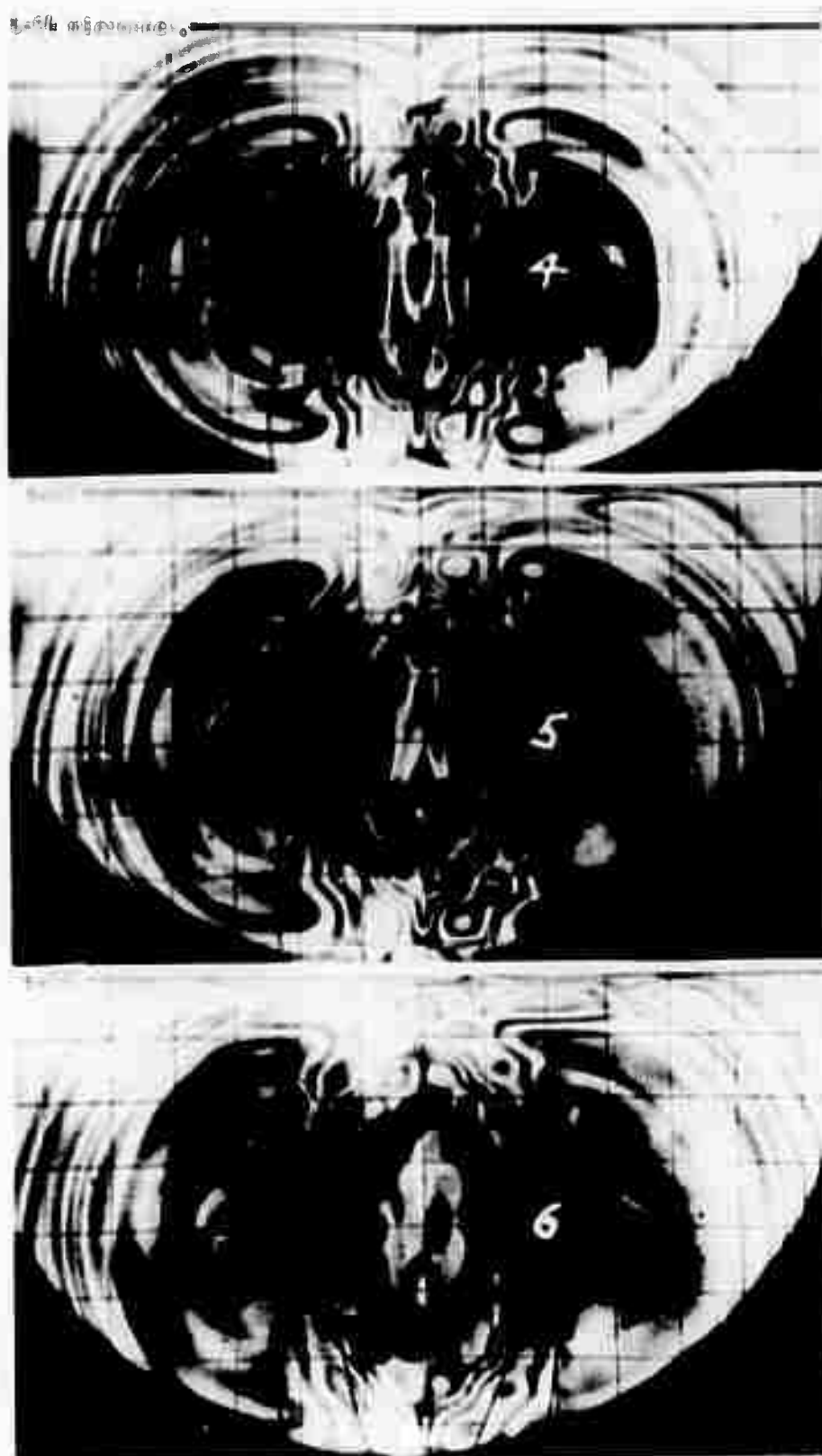


Fig. 3.3A Fringe Patterns Illustrating Interaction of P Waves (frames 1, 2 and 3)

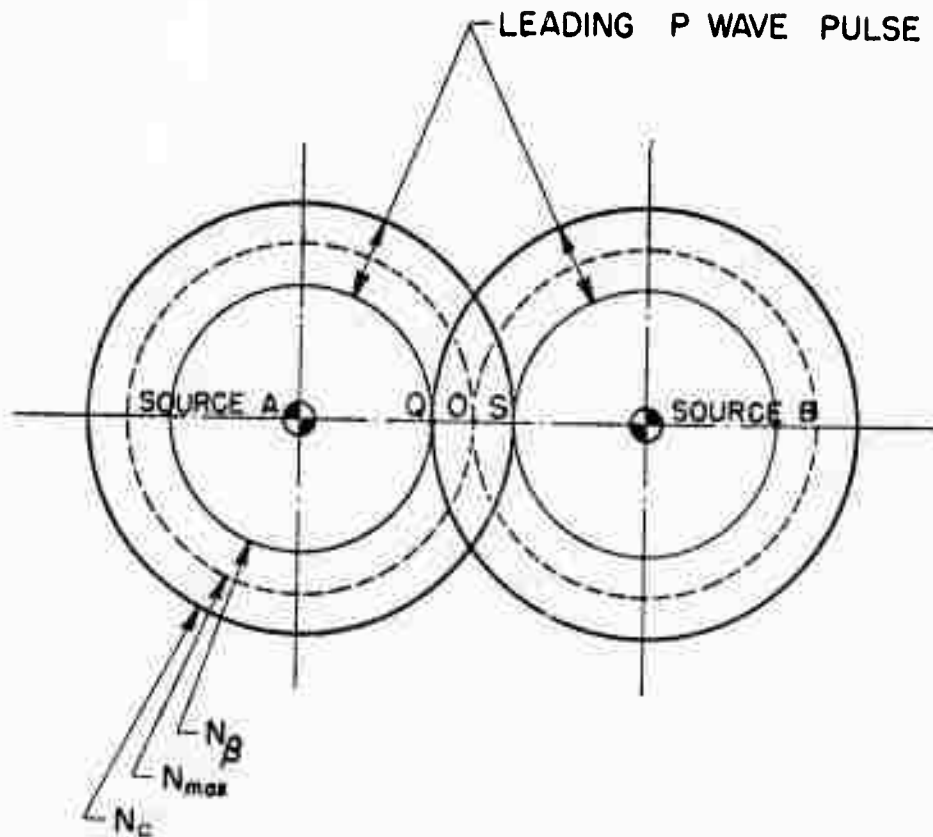


**Fig. 3.3B Fringe Patterns Illustrating Interaction of P Waves
(frames 4, 5, and 6)**

fringe maxima which can be observed in frame 2 in the central region between the sources. Later in frame 3, four fringe maxima are observed along lines making an angle of 15 degrees to the vertical centerline between charges. The top two of these four fringe peaks move toward the free boundary of the half-plane in frames 4, 5 and 6 shown in Fig. 3.3B and are the predominate feature during this interval prior to the reflection from the free boundary.

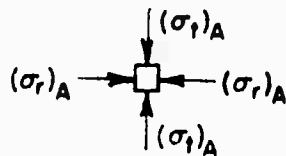
The first reinforcement along the line joining the two sources occurs when the two leading pulses of the P waves precisely overlap. The resultant stress is obtained by a direct superposition of the principal stresses along the centerline. This simple algebraic addition of the stresses is possible because the direction of the principal stresses in both the P waves coincide and remain constant for all points on the centerline. The fringe order at any point on the line connecting the two charges is obtained by direct addition following the procedure outlined in Fig. 3.4.

A fringe pattern representing the maximum reinforcement by superposition of the two P waves is shown in Fig. 3.5. A maximum fringe order of about 11 is observed at point O, the center between the sources. As indicated previously in Fig. 3.4, this peak results from an addition of the 5.5 order fringes (maxima) associated with each of the two P waves. The absolute maxima along the centerline will occur only when the maximum fringe orders associated with each of the two P waves are tangent to each other.



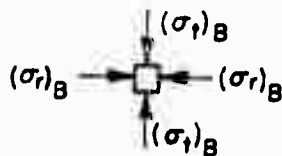
At Q

Due to P wave from source A



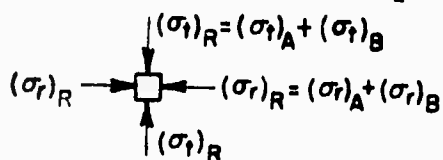
$$(\sigma_r - \sigma_t)_A = N_B \frac{f\sigma}{h}$$

Due to P wave from source B



$$(\sigma_r - \sigma_t)_B = N_A \frac{f\sigma}{h}$$

|| Resultant at Q



$$(\sigma_r - \sigma_t)_R = (N_A + N_B) \frac{f\sigma}{h} = N_R \frac{f\sigma}{h}$$

Similarly, at S $N_R = N_A + N_B$ and at O $N_R = 2N_{\max}$

Fig. 3.4 Fringe Superposition Along the Centerline

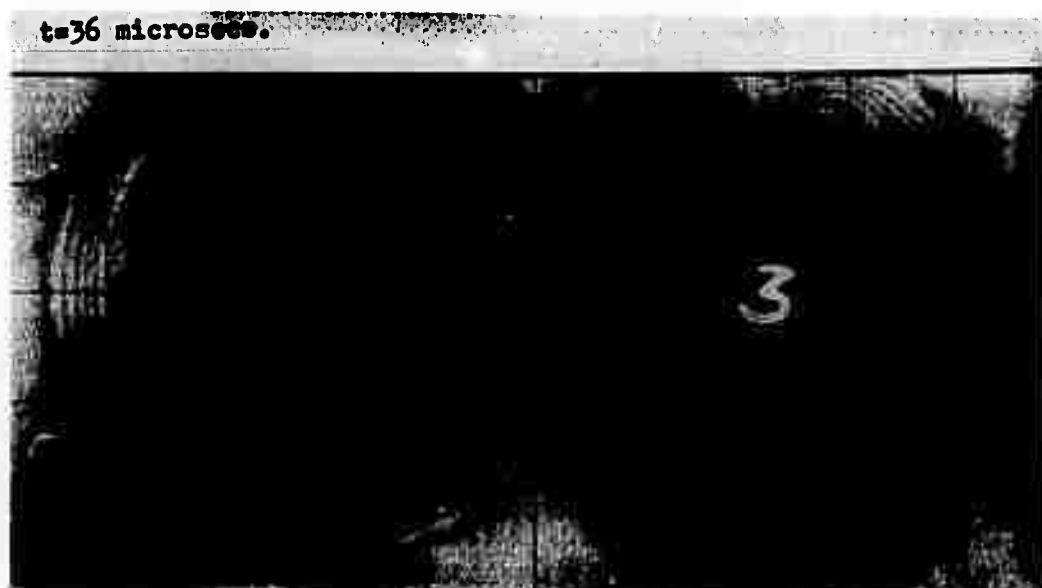
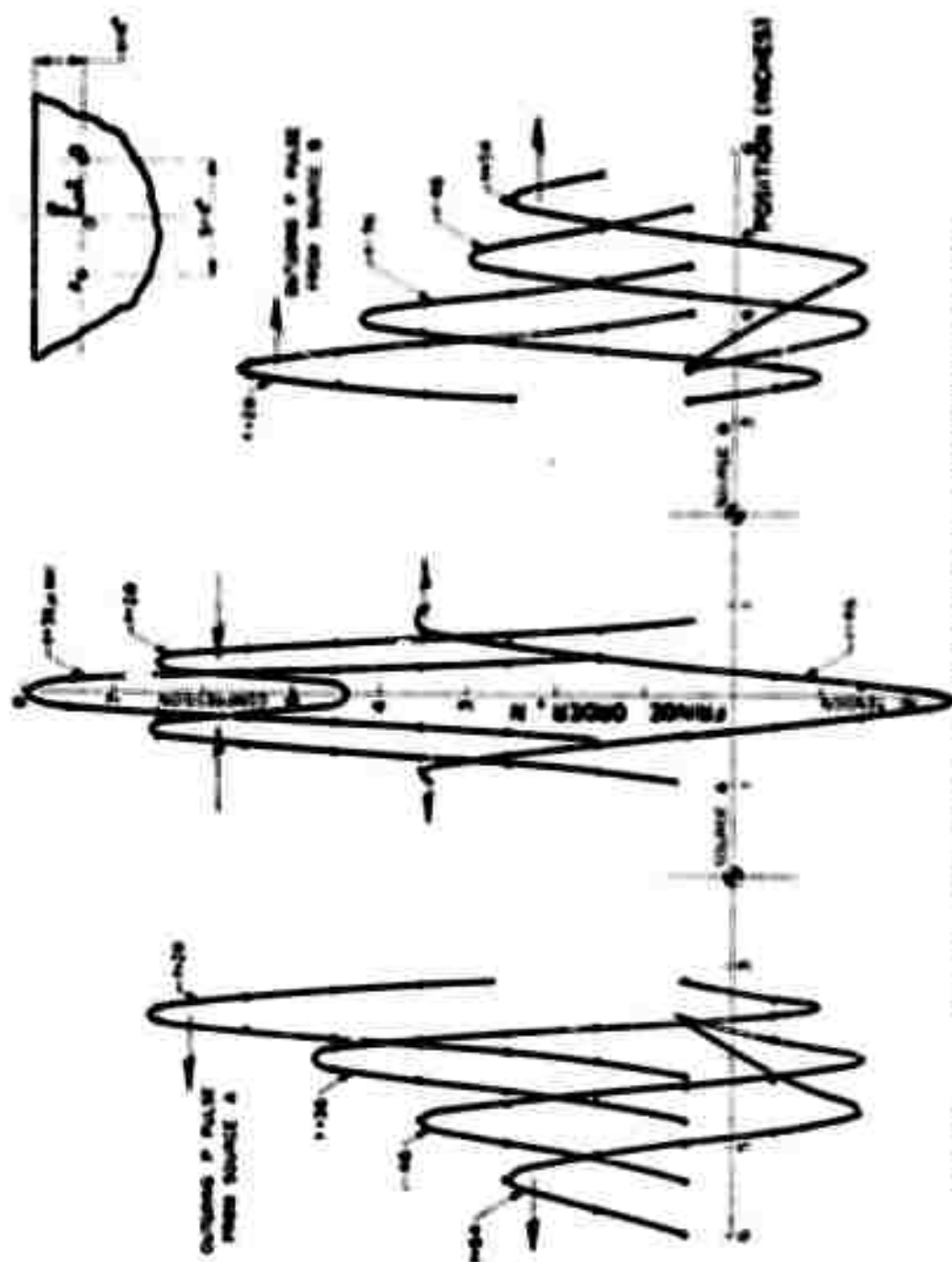


Fig. 3.5 Reinforcement of Fringe Patterns along the Centerline.
($h=2$ in. $s=4$ in.)

The high stress at point O due to P wave reinforcement decays very rapidly as the waves cross each other. This decay is illustrated very clearly in frames 2 and 3 of Fig.

3.3A. Curves of fringe order as a function of position along the centerline for the model with $h = 4$ in and $S = 4$ in. are shown in Fig. 3.6. The curves in the center of the figure in the neighborhood of point O represent the P wave reinforcement. The wave forms on the left and right show the propagation and attenuation of P waves away from the sources; however, it is the center region which is of primary interest. The dynamics of the reinforcement process are clearly presented by these curves. The two waves are approaching each other at $t = 28 \mu \text{ sec}$ with their leading edges interacting. The maximum reinforcement is observed at $t = 36 \mu \text{ sec}$ where a fringe order of eight was observed. This is somewhat lower than the absolute maximum of nine which occurred at $t = 34 \mu \text{ sec}$. As the waves propagate through each other, the maximum fringe order decays very rapidly. Between $t = 36$ and $46 \mu \text{ sec}$, the fringe maxima at point O attenuates from 8 to 2.5 fringes. Finally at $t = 64 \mu \text{ sec}$, only 0.5 order fringes remain and the region between the sources is of low stress.

The second peak which is formed at point O at $t = 46 \mu \text{ sec}$ is more important than the maximum fringe order of 2.5 would seem to indicate. This peak is produced when the trailing portion of the two P waves reinforce each other. Thus, the state of stress associated with this second peak is bi-



axial tension and as such it may be significant in producing fracture in the zone between the charges.

Similar results are presented for the model with $h = 2$ and $S = 4$ in. in Fig. 3.7. Again the very rapid build up to a high compressive peak (at $t = 36 \mu \text{ sec}$) of about 10.5 fringes is followed by a rapid decay and the formation of the second peak at $45 \mu \text{ sec}$.

Increasing the distance between the sources decreases the fringe order maxima along the centerline. This decrease occurs because the stress waves travel a larger distance before interaction occurs and the stresses associated with each P wave attenuate. A cursory study of the fringe patterns for $h = 4$ in. and $S = 4, 6, 8$ and 10 in the appendix illustrates the decrease in N_{MAX} along the connecting line as the distance between the two sources is increased.

The fringe order at point O, the center-point between sources is shown as a function of time in Fig. 3.8 for several different models. It is apparent that the state of stress changes very rapidly from a high-level compression peak to a lower level tensile peak. The magnitude of N_{MAX} in the compressive peak decreases appreciably as S is increased from 4 to 10 in. regardless of the value of h . The magnitude of N_{MAX} associated with the trailing tensile peak also diminishes; however, the relative decrease of the tensile maximum is less than that in the compressive maximum.

This discussion demonstrates that high stresses occur along the connecting line due to reinforcement of the lead-

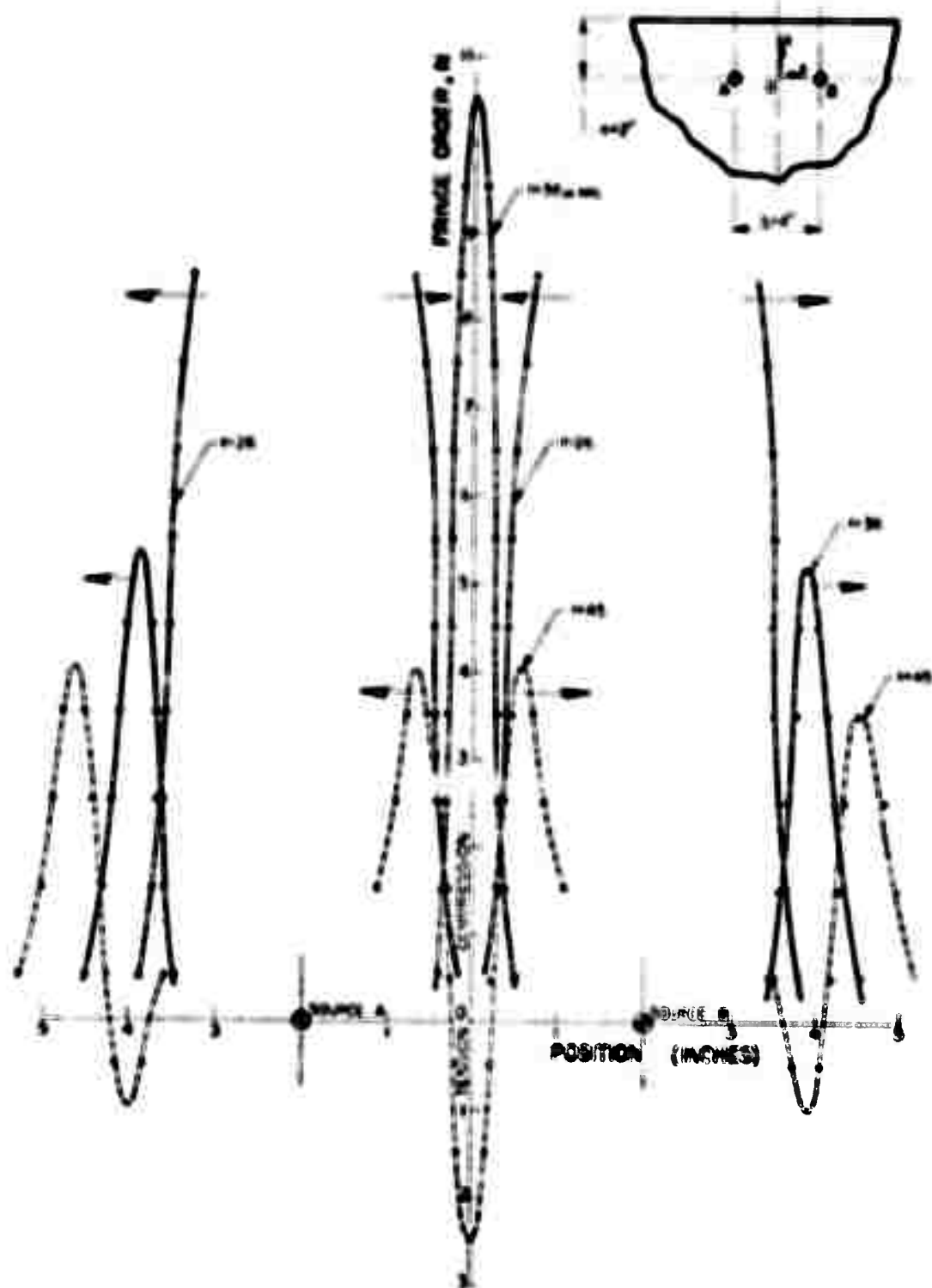


FIG. 37 PRINCE ORDER AS A FUNCTION OF POSITION ($n/\lambda=1$, $0/\lambda=2$)

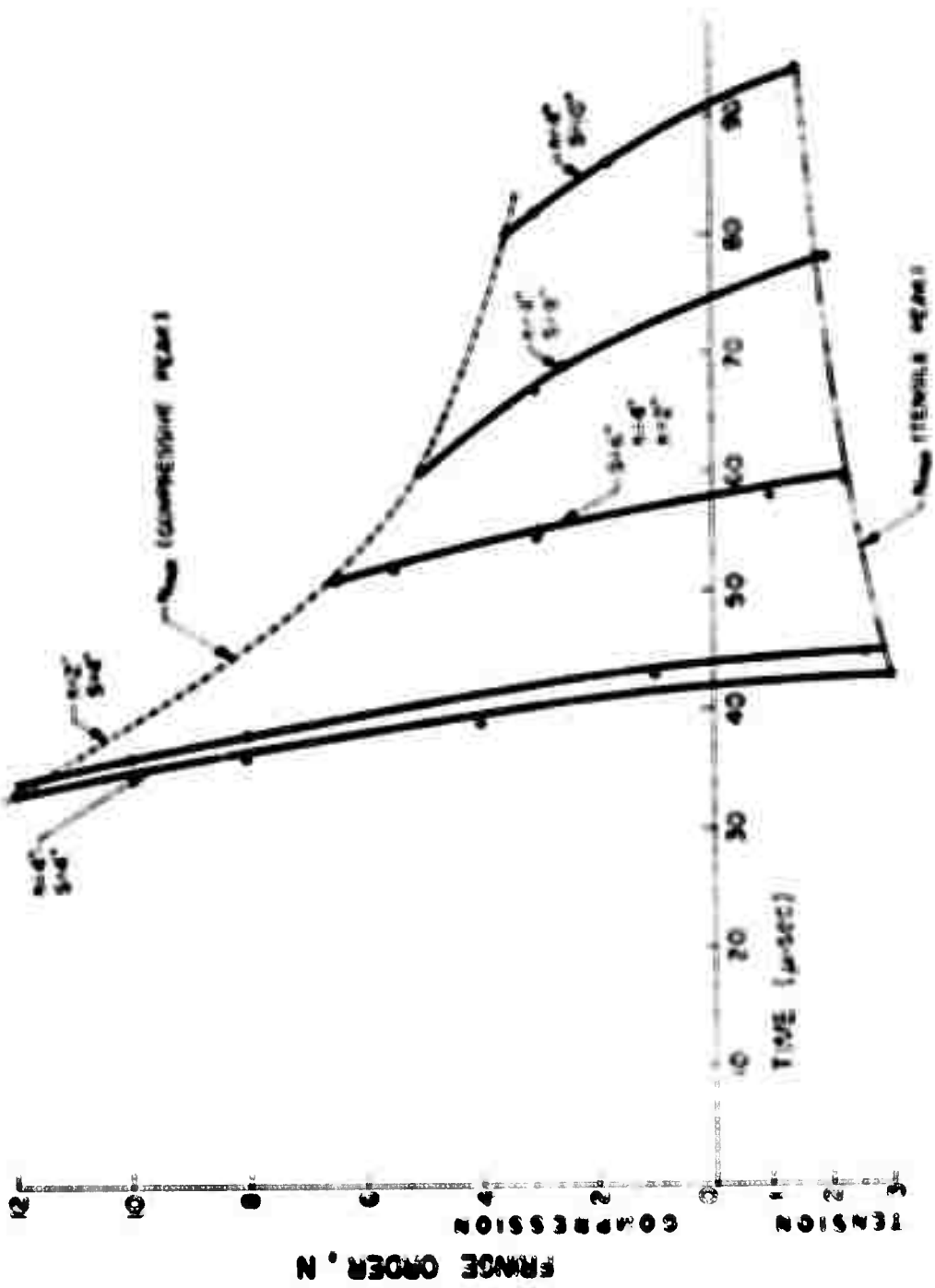


FIG. 3.6 FRINGE ORDER AT CENTER POINT BETWEEN SOURCES AS A FUNCTION OF TIME

ing pulse and the first trailing pulse in the P wave. These high stresses occur over a very short time interval because the P waves cross each other at very high velocity. It was concluded that varying the depth of charge h had no effect on the magnitude of the maximum stress at point O provided that the influence of free boundary reflection was not significant. Increasing S decreased the maximum fringe order as a result of P wave attenuation before interaction.

Next, consider the interaction of the two incident P waves which takes place in regions removed from the center-point. After the two P waves have crossed, four fringe peaks are formed along straight lines which make an angle $\phi = 10$ to 20 degrees with the vertical center-line (See Fig. 3.3A, frame 3). The formation of these maxima result from a superposition of the leading compressive pulse of one P wave with the tensile tail of the second P wave. This type of reinforcement increases the difference in the two principal stresses ($\sigma_1 - \sigma_2$) which in turn results in a higher fringe order.

Curves showing the fringe order as a function of position along a line η which passes through one of the peaks are presented in Fig. 3.9. These results show two dominant maxima for each frame. The leading peak is associated with the leading pulse of the incident P wave and the second and largest peak is due to the interaction of the two P waves. Both of these peaks decay as the waves move into the field during the progress of the dynamic event.

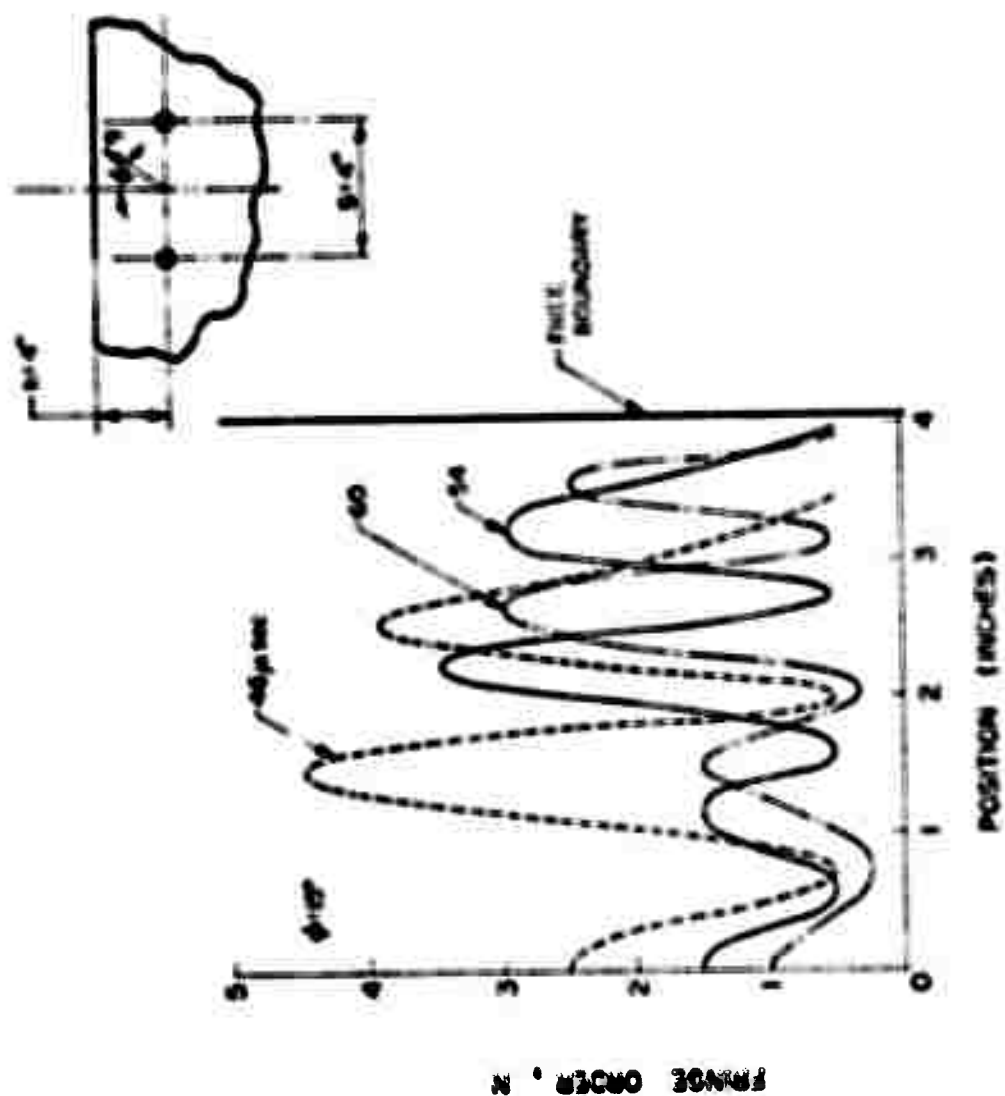


FIG. 3-9 FRINGE ORDER AS A FUNCTION OF POSITION ALONG η
 $(b/\lambda = 2, \delta/\lambda = 2)$

When S is increased, the principal stress difference along the η line decreases. Fringe orders as a function of position along η for a model with $S = 6$ in. is given in Fig. 3.10. The fringe maximum along η was first observed at $t = 63 \mu$ sec. Its maximum amplitude was only 2.5 fringes as compared to 4.5 fringes for the model with $S = 4$ in. Moreover, the peak stress occurs at larger values of η (closer to the free boundary) with increasing S because the waves travel a greater distance before the interaction begins. This increased distance between the sources changes the position of the η line from $\theta = 15$ degrees with $S = 4$ in. to $\theta = 10$ degrees with $S = 6$ in.

The reinforcement along the η line essentially involves the combination of two low-level pulses when $S \geq 8$ in. The photoelastic fringe pattern for $h = 4$, $S = 8$ in. presented in Fig. 3.11 shows peaks of about $N = 2$; however, it occurs after the reflection from the free boundary becomes the dominate portion of the dynamic process. The effect of S on N_{MAX} is presented in Fig. 3.12 where the fringe order is shown as a function of time for models with $h = 4$ in. (constant) and $S = 2, 4, 6$ and 8 in. These results clearly indicate the attenuation in N_{MAX} as S is increased.

When h is decreased to 2 in., three effects can occur depending upon the relative values of h and S . First when $S/h > 2.5$ to 3 the incident wave has attenuated so much that the pulse formed by reinforcement is still small in magnitude. Second, when $S/h = 2$, fringe maxima do occur but

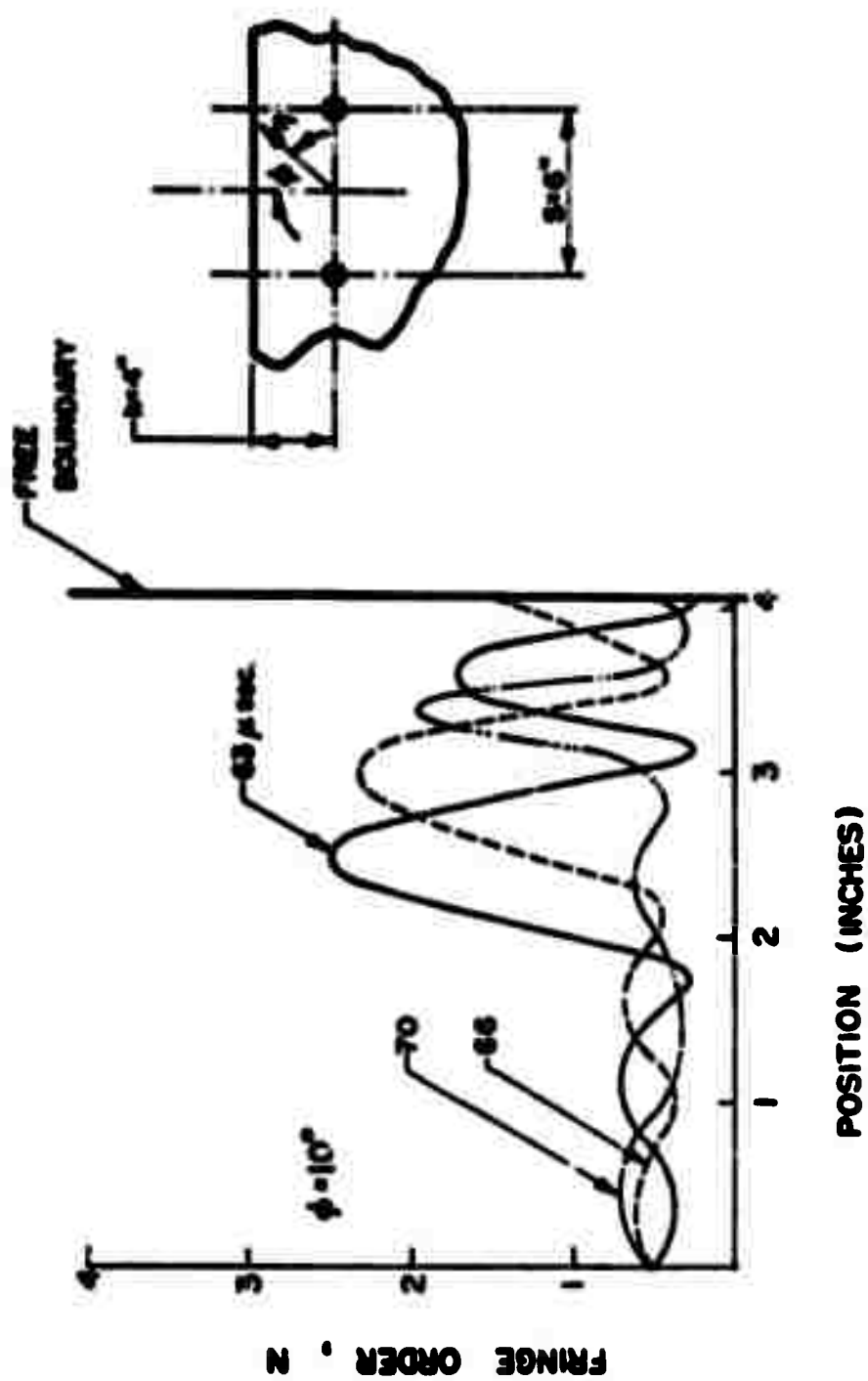


FIG. 3-10 FRINGE ORDER AS A FUNCTION OF POSITION ALONG y

$$(h/\lambda = 2, \quad s/\lambda = 3)$$



Fig. 3.11 Fringe Patterns Illustrating Low-Level Reinforcement when $S/\lambda \geq 4$

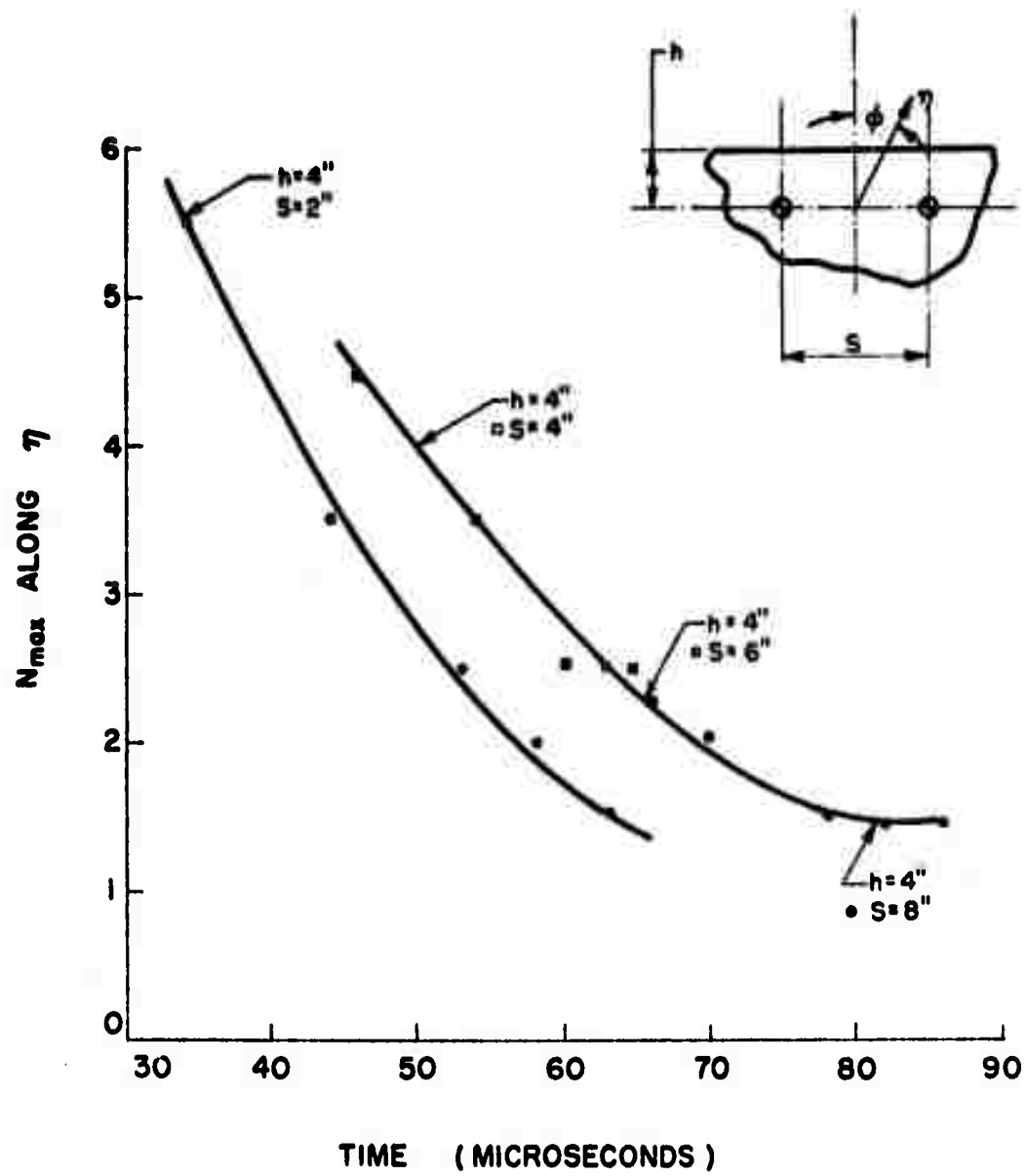


FIG. 3-12 FRINGE ORDER N_{max} ALONG η AS A FUNCTION OF TIME

these peaks are strongly influenced by the reflected PP wave. This type of reinforcement is illustrated in Fig. 3.13 (frame 4) and the effect of the reflected PS wave is apparent in frame 5. Finally, when $S = h = \lambda$, the reinforcement along η becomes insignificant compared to the high stresses produced along the connecting line.

3.3. Conclusions (Pre-reflection period).

The experimental data presented here clearly shows that the reinforcement due to the interaction of the incident P waves from the sources is significant. Reinforcement occurs at the centerpoint of the line connecting the two sources and also along the η line which makes an angle $\phi = 10$ to 15 degrees to the vertical center-line.

The magnitude of the stresses in these regions of reinforcement depends on the relative values of h , S and λ^* . Along the connecting line, decreasing S/λ increases the maximum principal stress difference while varying h/λ has no effect providing $h \geq \lambda$. The magnitude of the angle ϕ which defines the η line decreases with increasing S/λ approaching zero as $S/\lambda > 5$. Decreasing S/λ increases the principal stress difference along η . Decreasing h/λ also increases the principal stress difference along η since the reflected PP and PS waves enter into the interaction and enhance the reinforcement near the boundary.

* λ is the predominate wave length in the incident P wave (taken as 2 inches).

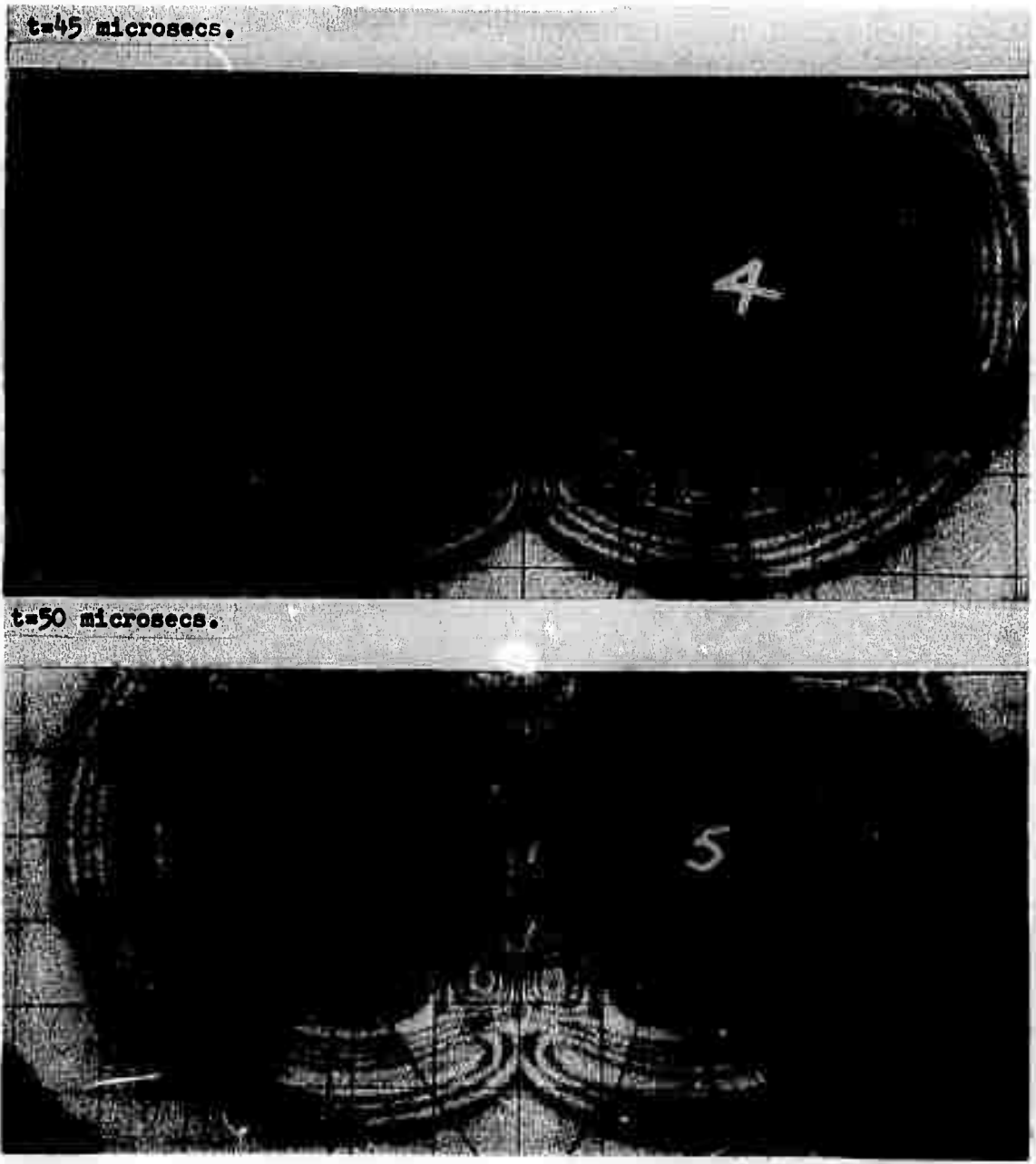


Fig. 3.13 Fringe Patterns Indicating Influence of Free Boundary Reflections on Fringe Peaks along the η Line.

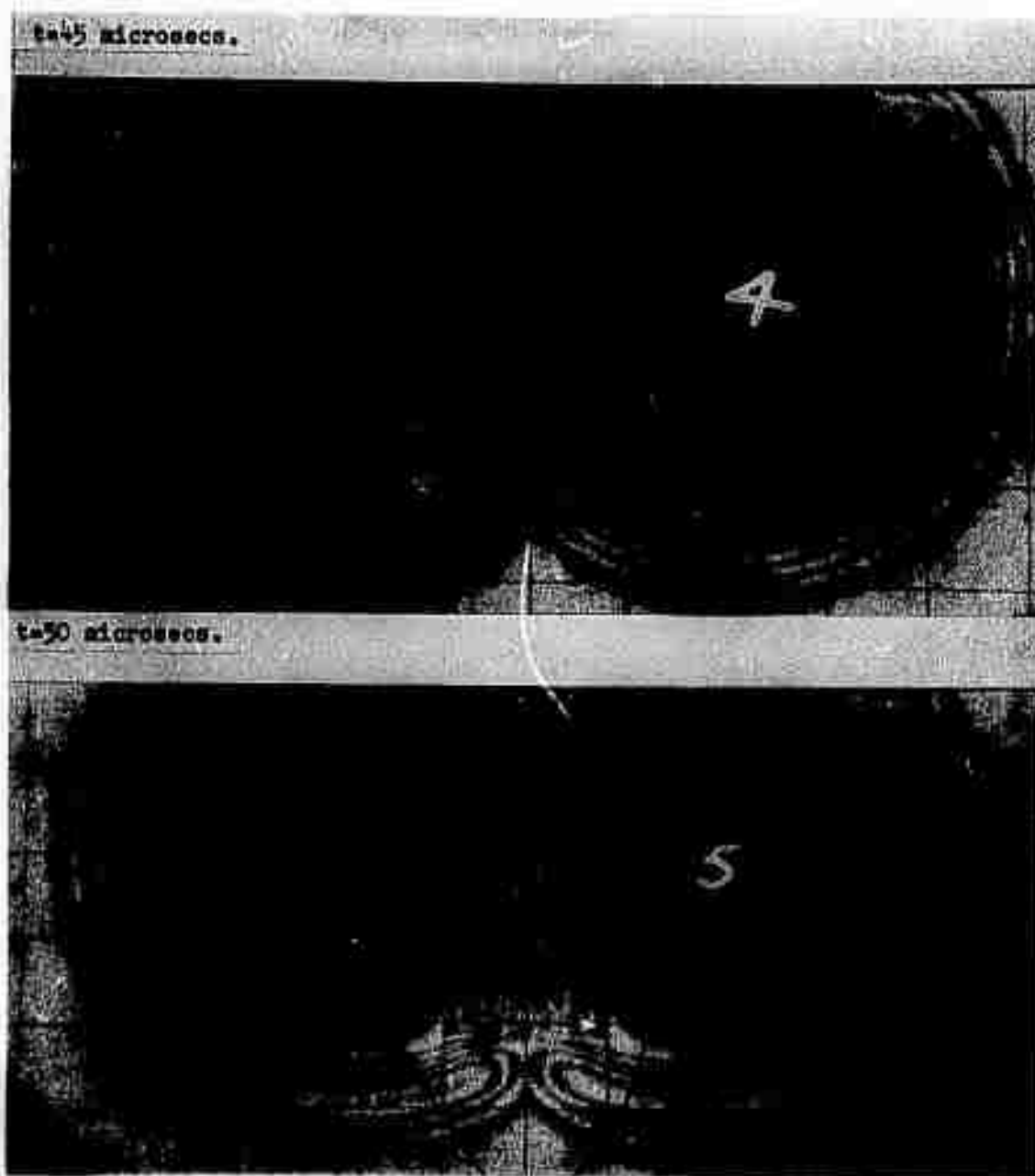


Fig. 3.13 Fringe Patterns Indicating Influence of Free Boundary Reflections on Fringe Peaks along the η Line.

IV. PHOTOELASTIC RESULTS: POST-REFLECTION PERIOD

This section covers a detailed analysis of the post reflection behavior of the interaction of dilatational waves with the free surface of a half-plane. The analysis first treats the reflection from a single dilatational source and then the more complex reflection phenomenon from multiple sources is examined. Attention is focused on the geometric parameters h/λ and S/λ to establish their effect on the stresses produced near the boundary. Interactions between the incident dilatational P waves, the reflected dilatational PP waves and reflected shear PS waves are closely examined to show reinforcement conditions which increase the stresses near the boundary. The results shown enhance the understanding of the stress wave reflection process which significantly affects the rock removal and fragmentation so important in the operating economies of open-pit mining.

4.1. Stress Wave Reflection Due to a Single Dilatational Source in a Half-Plane ($h/\lambda = 1$ and 2)

An outgoing P wave with a cylindrical front interacts with a straight boundary to produce reflected dilatational wave PP and a shear wave PS. This analysis is intended to show the interaction between the incident P and the reflected PP waves and the characteristics of the PS wave. The data established in the study of the reflection patterns produced from a single source, will serve as a basis for extending the investigation to the more complex topic of post-

reflection behavior of stress waves produced by multiple sources in the half-plane.

The first aspect of the reflection process involving the incident P wave is the development of the reflected PP wave. Typical photoelastic patterns which represent the early portion of the reflection process are shown in Fig. 4.1 for a model with $h/\lambda = 2$. These patterns show a very rapid change in the stress distribution near the boundary. The leading pulse in the PP wave and the first trailing pulse in the incident P wave both are both tensile; thus, they reinforce each other to produce a region of high tensile stress.

The beginning of the reflection process is shown in frame 3 of Fig. 4.1 where the fringes are nearly tangent to the free boundary. Here a maximum fringe order of 2.5 representing the biaxial compressive stress in the leading pulse of the P wave can be observed approximately 0.4 in. from the boundary. Shortly after (13 μ sec) the fringe peak ($N = 3$) illustrated in frame 5 occurs at about the same distance from the boundary. However, due to the reflection process the sign of the stresses are reversed and this fringe peak represents a state of biaxial tension.

The fringe order as a function of position along the center line of the model is given in Fig. 4.2 over the time interval from $40 \leq t \leq 88$. The wave forms are shown coming into the boundary for $t < 58 \mu$ sec and outgoing from the boundary for $t > 58 \mu$ sec. The conversion from a compressive

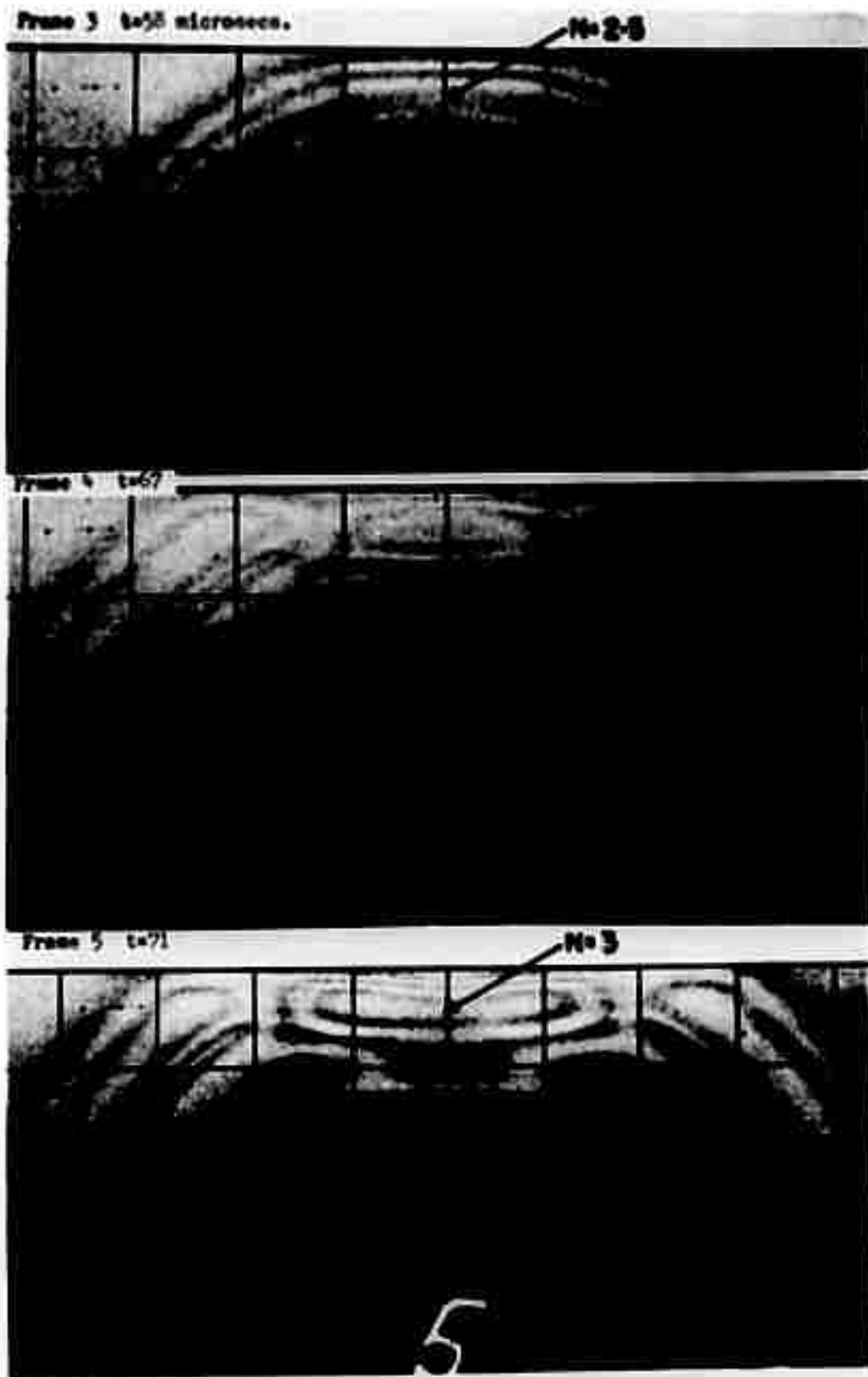


Fig. 4.1 Early Interval in the Reflection of an Incident P Wave

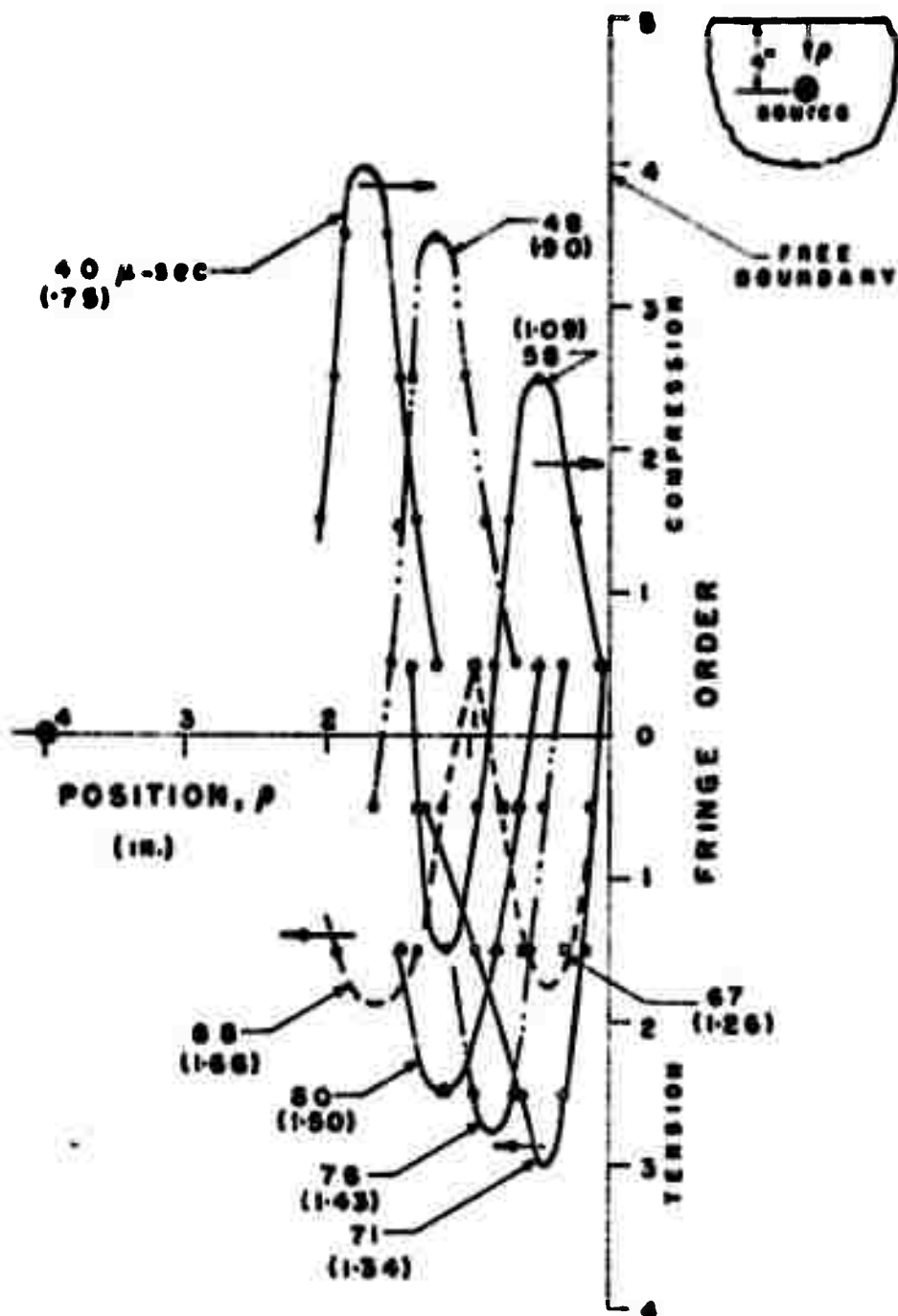


FIG. 4-2 FRINGE ORDER AS A FUNCTION OF POSITION
ALONG VERTICAL THROUGH SOURCE ($n/\lambda=2$, $s/\lambda=0$)

to a tensile state of stress is indicated, as well as the rapid establishment of the post reflection tensile peak near the boundary. It is noted that the numbers in parentheses are normalized by dividing the actual time by the time required for the incident P wave to reach the boundary (53 μ sec).

Reinforcement of the P and PP waves occurs for only a short interval since the two waves cross each other at a high speed and their pulse length is short. Hence, the tensile stress region not only moves away from the boundary but also attenuates rapidly. Both of these effects are illustrated in frames 7 and 9 of Fig. 4.3. It is clear that scabbing failure of a brittle material should initiate in the time of the build-up to a tensile peak between $67 \leq t \leq 71 \mu$ sec, at a location of approximately $\lambda/4$ from the boundary. The region of high tensile stress is relatively local as it is confined to the central area about one inch to either side of the center-line.

When h/λ is decreased from 2 to 1, the reinforcement of the P and PP waves is effected in three ways. First, the fringe peaks due to the reinforcement are much higher since the incident P wave has not attenuated to the degree noted with $h/\lambda = 2$. Second, the attenuation of these fringe maxima is negligible for a relatively long time interval (45 to 55 μ sec). Finally, fringe maxima of significant magnitude $N = 4.5$ occur over a region well below the boundary extending as deep as $\lambda/2$.

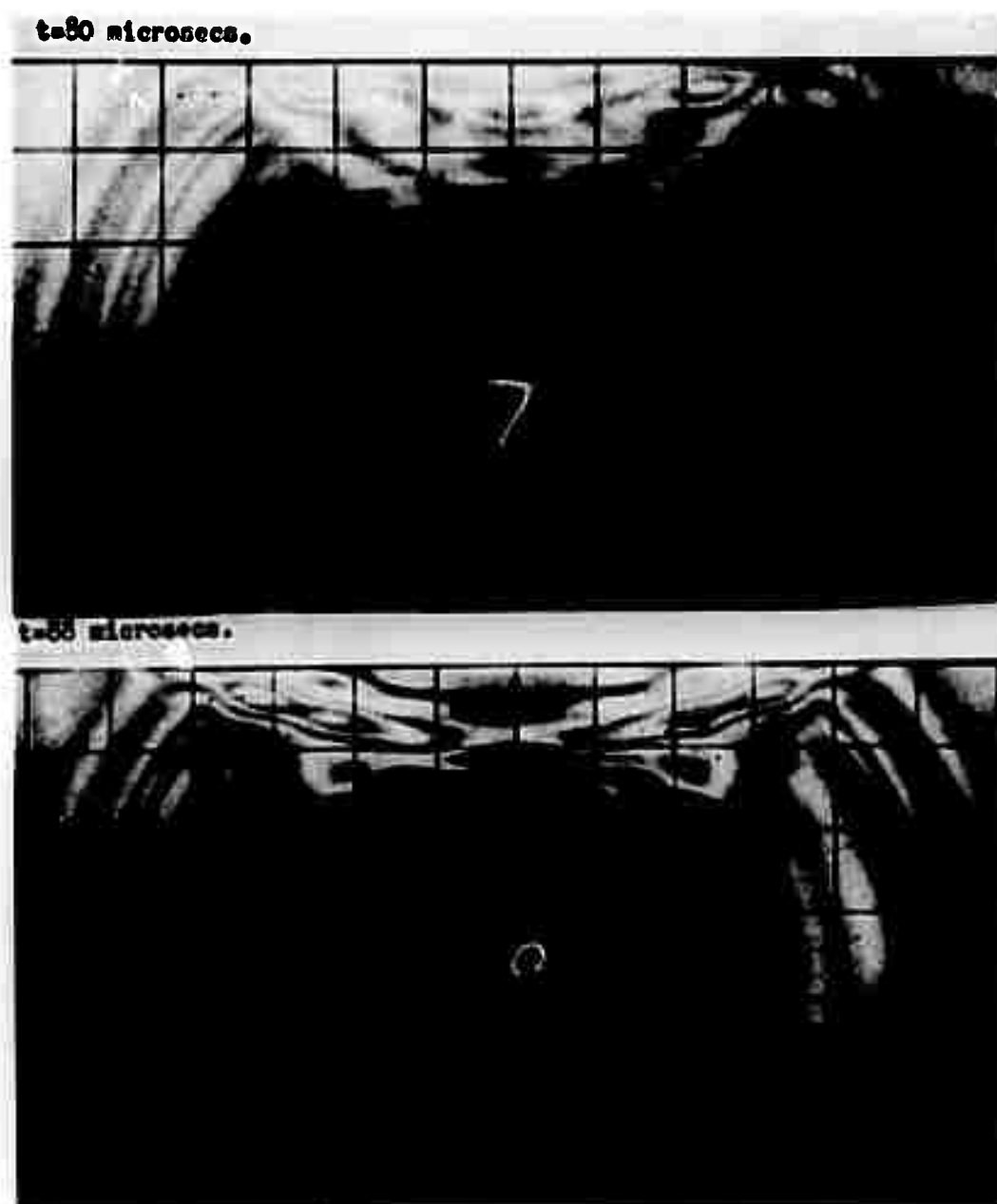


Fig. 4.3 Mid-interval in the Reflection of an Incident P Wave

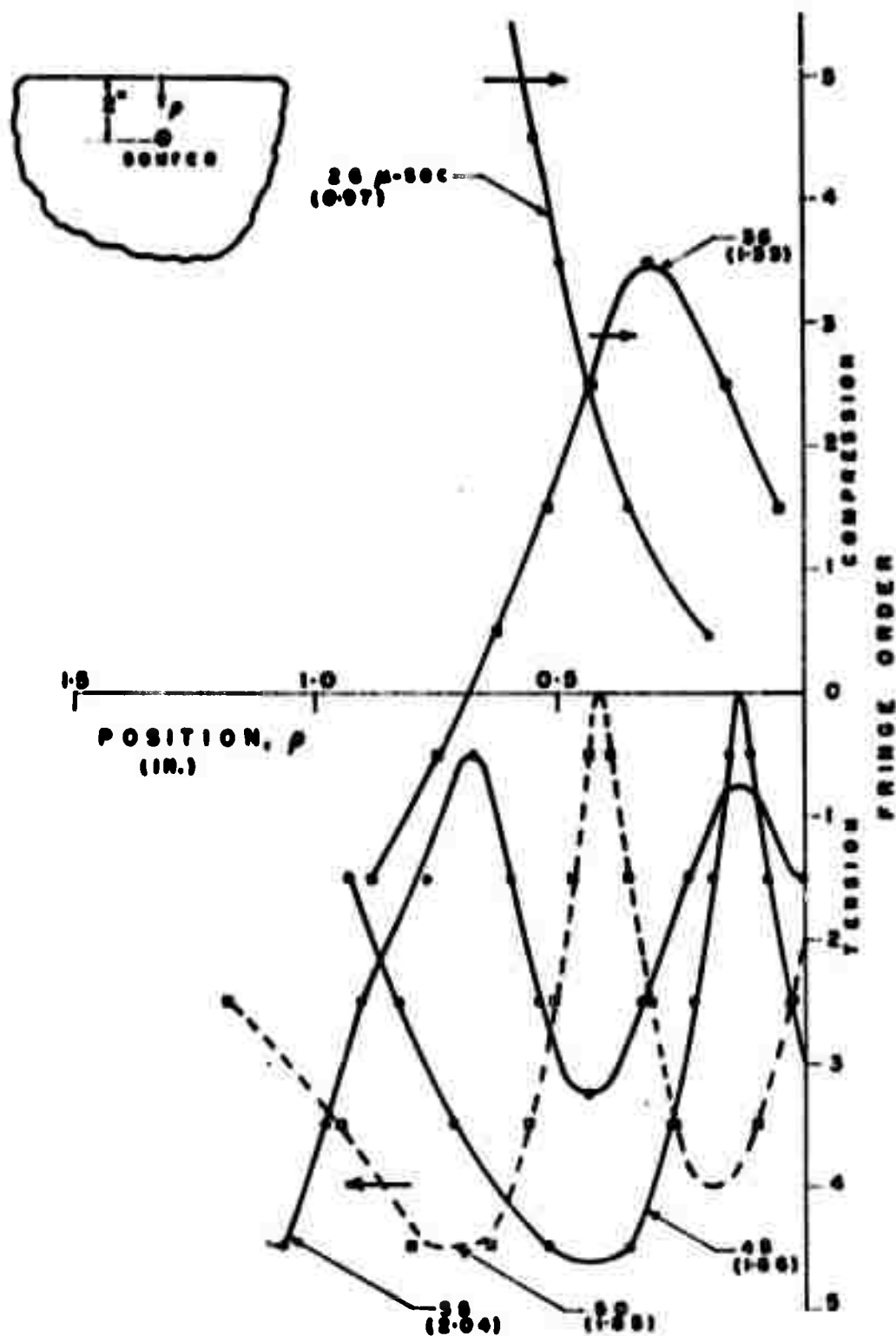


FIG. 4.4 FRINGE ORDER AS A FUNCTION OF POSITION ALONG VERTICAL THROUGH SOURCE ($h/\lambda=1$, $s/\lambda=0$)

As the P wave interacts with the boundary it generates a shear wave PS at all angles of incidence except the normal. Along the normal direction no reflected shear wave is produced and the P wave in effect reflects, reversing its sign. Consequently, the vertical line above the source can only be influenced by P and PP interactions.

An example of the fringe patterns associated with the PS wave observed in a dynamic photoelastic experiment is illustrated in Fig. 4.5. The separation of individual values of the principal stresses associated with this reflected shear wave can be accomplished directly from these isochromatic fringe patterns. Since the shear wave is equivoluminal, the first stress invariant must vanish and a state of pure shear exists and as indicated previously in Section 3.1

$$\sigma_1 = -\sigma_2 = \frac{N(f_o)d}{2h} \quad (2 \text{ bis})$$

The biaxial state of stress where the principal stresses are equal and opposite in sign is then in direct proportion to the fringe order. Although, regions containing the PS wave also contain tails of the P and PP waves the effect of these tails is small and Eq. 2 can be used to closely approximate the stresses.

The sequence of fringe patterns presented in Fig. 4.5 indicate the importance of the reflected shear wave in this dynamic event. High fringe orders and, hence, high tensile stresses exist along the wave. These stresses attenuate much

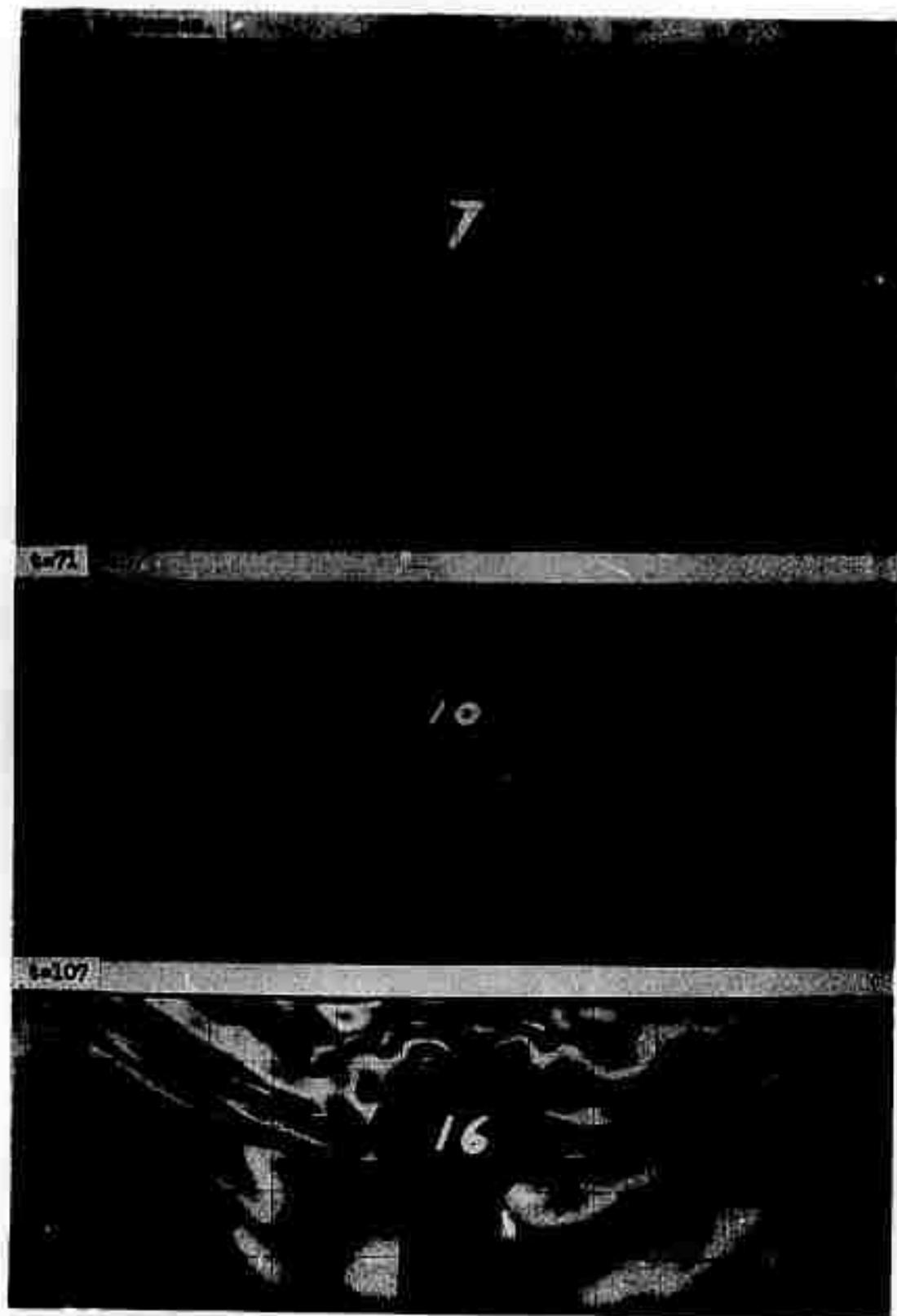


Fig. 4.5 Fringe Patterns Representing the Reflected Shear(PS) Wave.

more slowly with respect to both time and position than those corresponding to the P and PP wave interaction. The region effected by these stresses is much larger than the comparable region effected by the P and PP wave reinforcement.

Results from the model with $h/\lambda = 1$ showing the fringe order as a function of position x along a line drawn parallel to the free boundary are given in Figs. 4.6 and 4.7. The data in Fig. 4.6 is for a depth d of 0.3 in. and the data in Fig. 4.7 is for a depth d of 1 in. Comparison of these results show that the stresses in the reflected PS wave are higher at the $d = 0.3$ in depth than at the $d = 1$ in. depth. In both cases, the maxima decreases as the PS waves propagate into the field with the rate of decay being more abrupt for $d = 0.3$.

Similar results for the model with $h/\lambda = 2$ and $d = 0.3$ in. are presented in Fig. 4.8. The increased distance of the charge from the boundary has resulted in a pronounced decrease in the magnitude of the maxima fringe orders. However, the rate of decay of the fringe peaks with respect to the position parameter x is less with $h = 2$ inches.

Another form of presentation of the data associated with the PS wave is given in Fig. 4.9 where the fringe order N is shown as a function of the position parameter κ . Here κ is measured along a straight line drawn through the fringe maxima for the PS wave. As the PS wave is nearly planar in the region near the boundary, the κ axis is approximately parallel to the wave front. The results of Fig. 4.9 more

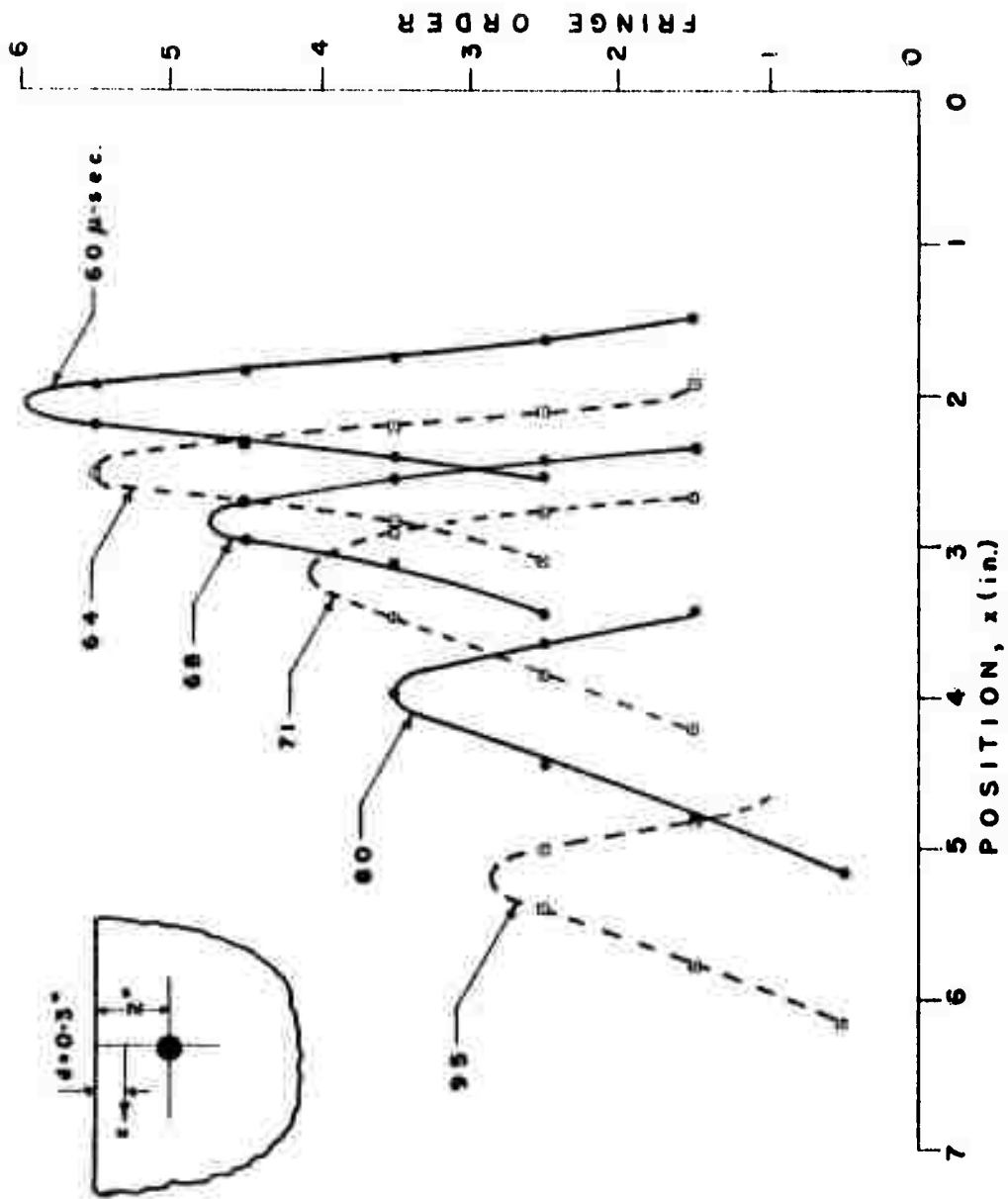


FIG. 4.6 FRINGE ORDER AS A FUNCTION OF POSITION x FOR THE
PS WAVE ($h/\lambda=1$, $s/\lambda=0$, $d=0.3''$)

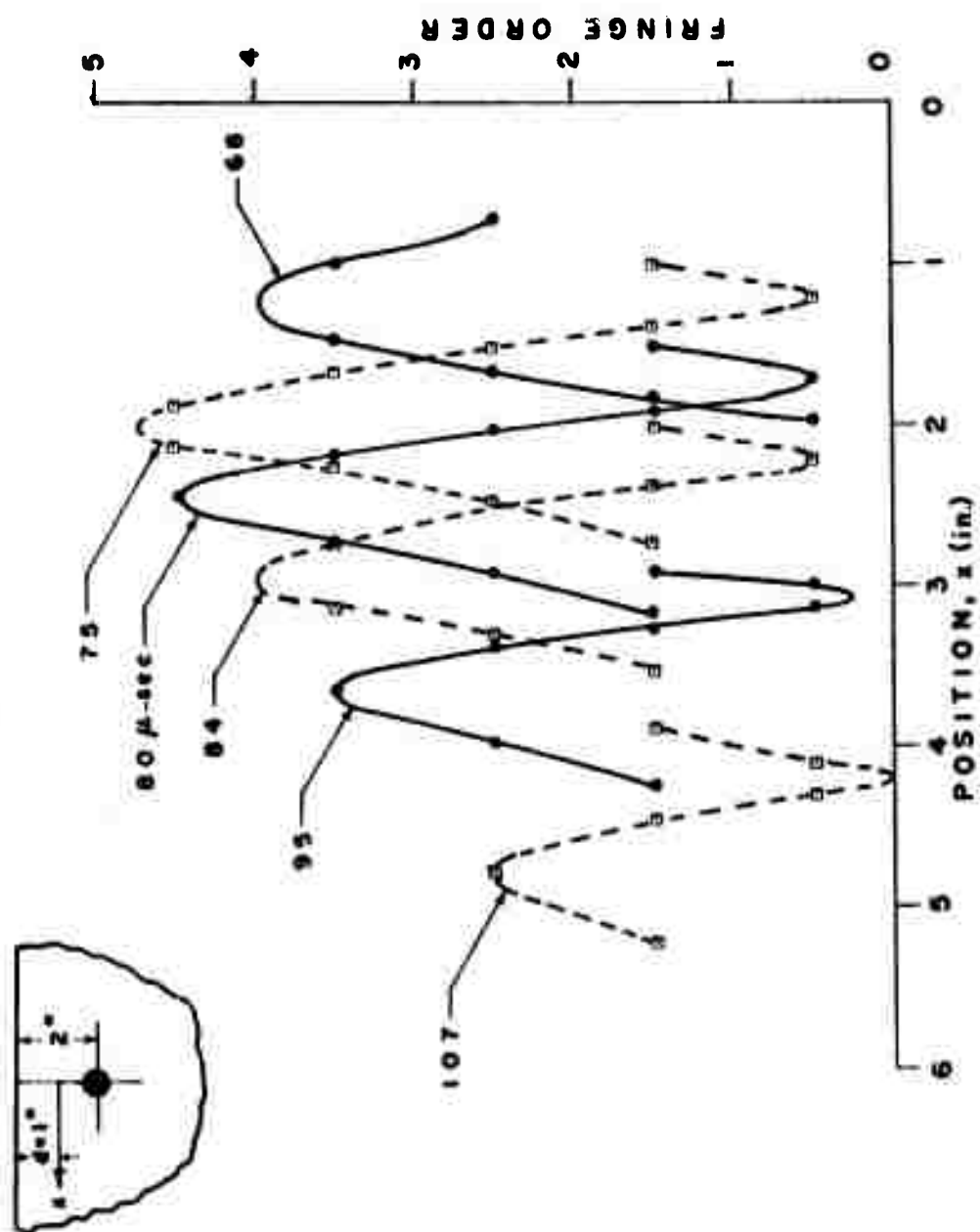


FIG. 4.7 FRINGE ORDER AS A FUNCTION OF POSITION x FOR THE
PS WAVE ($h/\lambda=1$, $s/\lambda=0$, $d=1.0''$)

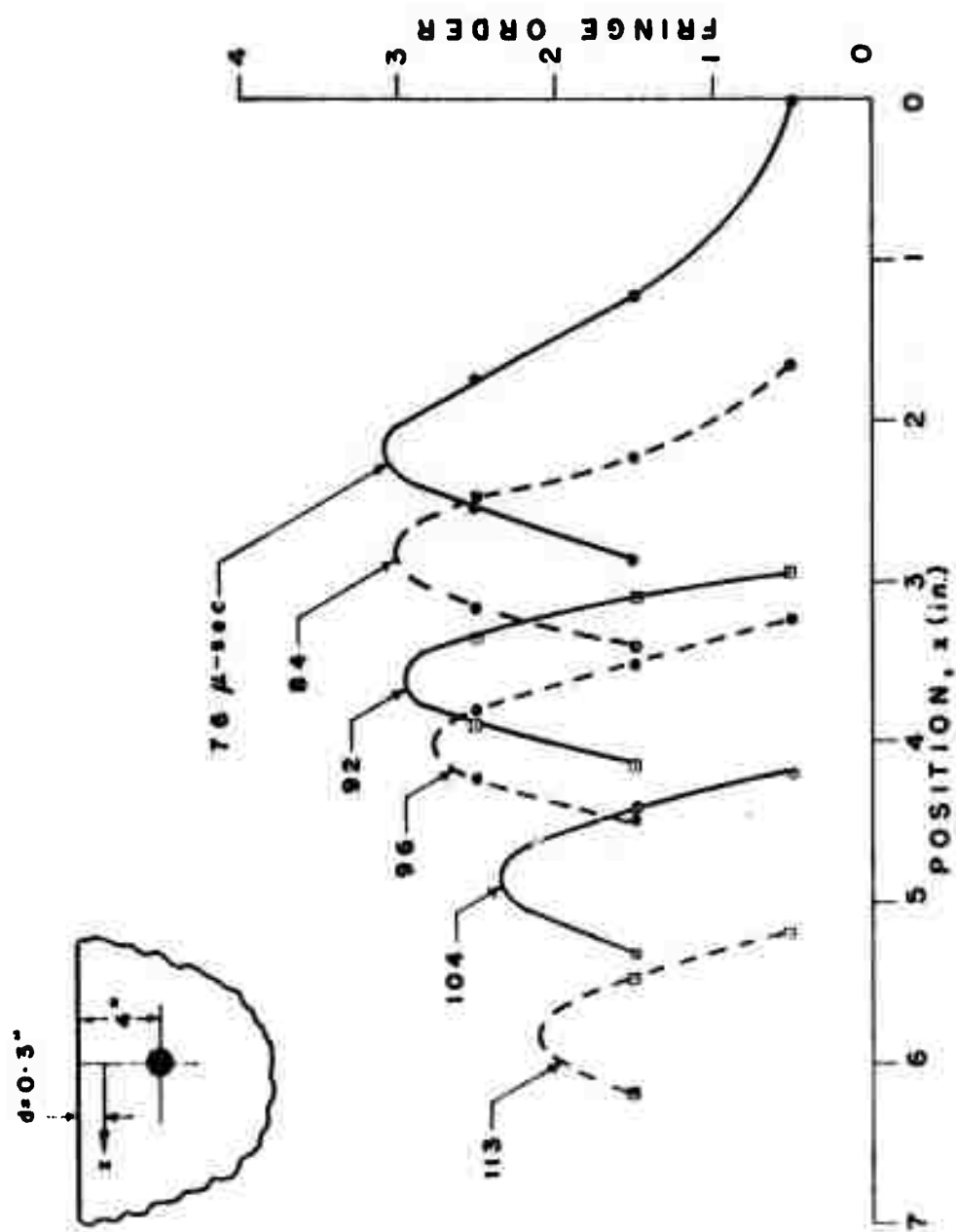


FIG 4-8 FRINGE ORDER AS A FUNCTION OF POSITION x FOR THE
PS WAVE ($h/\lambda=2$, $s/\lambda=0$, $d=0.3''$)

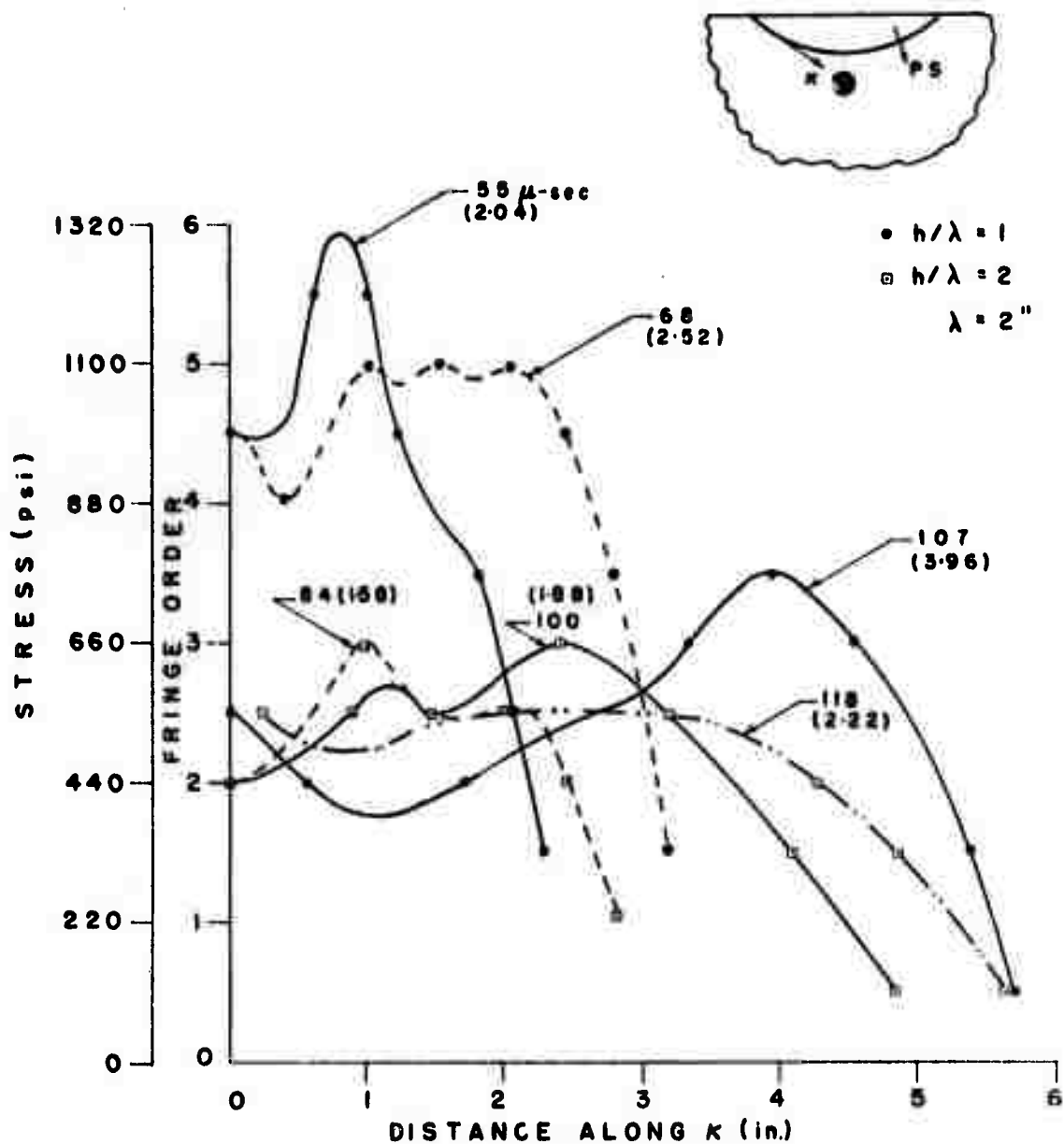


FIG. 4-9 FRINGE ORDER AS A FUNCTION OF POSITION κ FOR THE PS WAVE.

clearly demonstrate the influence of the depth of the charge h in decreasing the fringe order. Also it should be noted that fringe order decreases with κ at smaller values of κ for $h/\lambda = 1$ than for $h/\lambda = 2$.

4.2. Stress Wave Reflection Due to a Pair of Dilatational Sources in a Half-Plane ($h/\lambda = 2$)

When two sources generate dilatational waves in a half-plane, important interactions occur between the reflected and incident waves. For models with $h/\lambda = 1$, the predominate interaction is between the two reflected PS waves, whereas with $h/\lambda = 2$ the PP and P interactions are the most significant provided $s/\lambda < 2$. For instance with $s/\lambda > 2$ both the PS - PS interactions and the PP - PP interactions are equally important.

First, consider the experiments where h/λ was maintained constant at 2 and s/λ was varied from 1 to 5. The behavior of the interacting stress waves depended strongly on the s/λ parameter. For $s/\lambda = 1$ the two sources are close together and the two incident P waves interact before reaching the boundary. This pre-reflection interaction is demonstrated with a select group of fringe patterns shown in Fig. 4.10A (frames 3 and 4). Upon reflection a high tensile stress develops along the vertical centerline near the boundary. This subsurface tensile peak is shown in frame 7 of Fig. 4.10B and it is also illustrated in Fig. 4.11 where the fringe order distribution is given as a function of position along the centerline. The reinforced P wave exhibits a



Fig. 4.10A Pre-Reflection Reinforcement of the Incident P Wave.

$t=63$ microsecs.



$t=67$

$N=6.5$



Fig. 4.10B Post-Reflection Reinforcement.

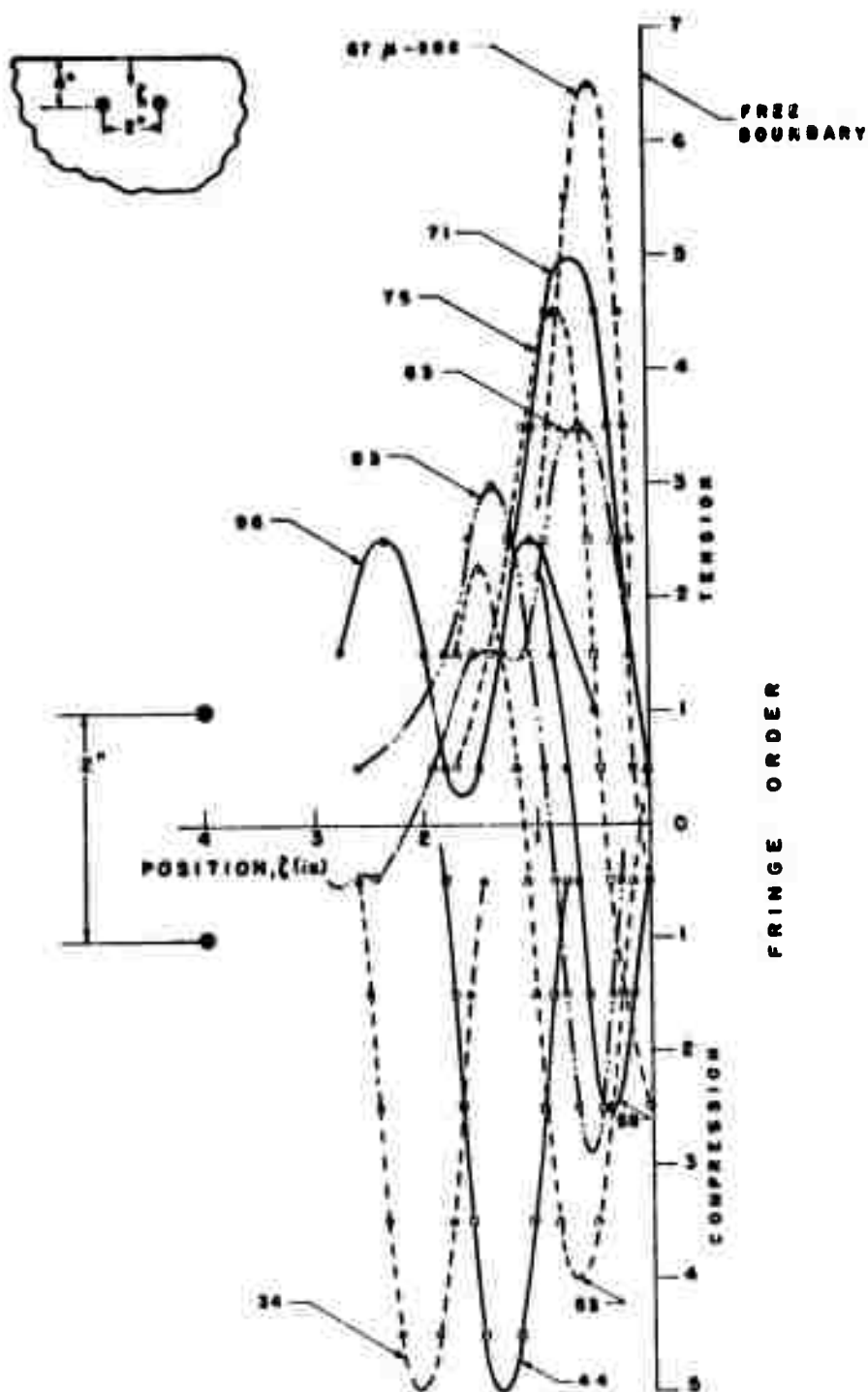


FIG 4-11 FRINGE ORDER AS A FUNCTION OF POSITION ALONG VERTICAL CENTERLINE, BEFORE AND AFTER REFLECTION ($h/\lambda = 2$, $s/\lambda = 1$)

peak fringe order of 4 just prior to reflection and after reflection this is magnified to 6.5 at a depth $\lambda/4$ below the boundary. A relatively high stress occurs at this location below the boundary over a lateral distance of about $2S$. As is evident in frame 7 of Fig. 4.10, $N > 3.5$ for a distance of 4 inches along a line parallel to the boundary at a depth $d = 0.5$ in. below the boundary.

As the event progresses the dynamic behavior is represented by the fringe patterns in Fig. 4.12. As shown in frames 8 and 9 the fringe maxima is beginning to attenuate and to move down the vertical centerline. Later (frame 11), the stresses due to the reflection of the reinforced P wave become less significant and the shear wave becomes predominate. The attenuation of the reflected pulse is illustrated in Fig. 4.11 where the decay of the fringe maxima is obvious as the wave propagates back into the model.

As the two sources are moved apart and $S/\lambda \geq 2$ the reflection behavior is markedly different and the reflected PP wave is considerably less significant. Fringe patterns (frame 4) of Fig. 4.13A show that the two P waves are reinforcing each other at the same time as the reflection process is under way. Examination of frame 7 shows the formation of two fringe order maxima above the sources about 0.4 in. from the boundary. These peaks correspond to tensile stresses which are produced by a PP wave and a P tail reinforcement as previously discussed.

Four μ sec. later, in frame 8, it is clear that the large

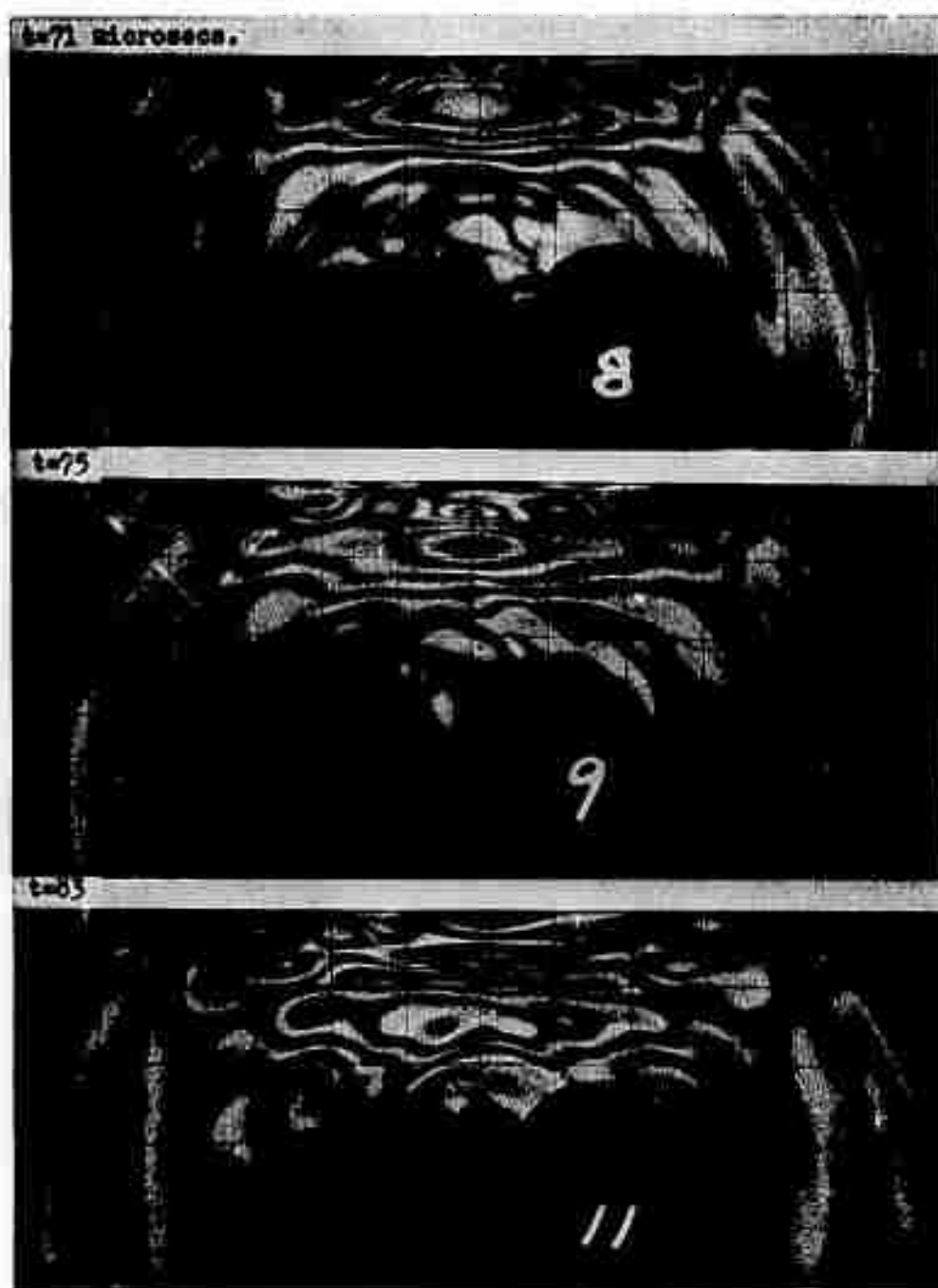


Fig. 4.12 Final Stages of the Reflection of the Reinforced P Waves with $S/\lambda = 1$.

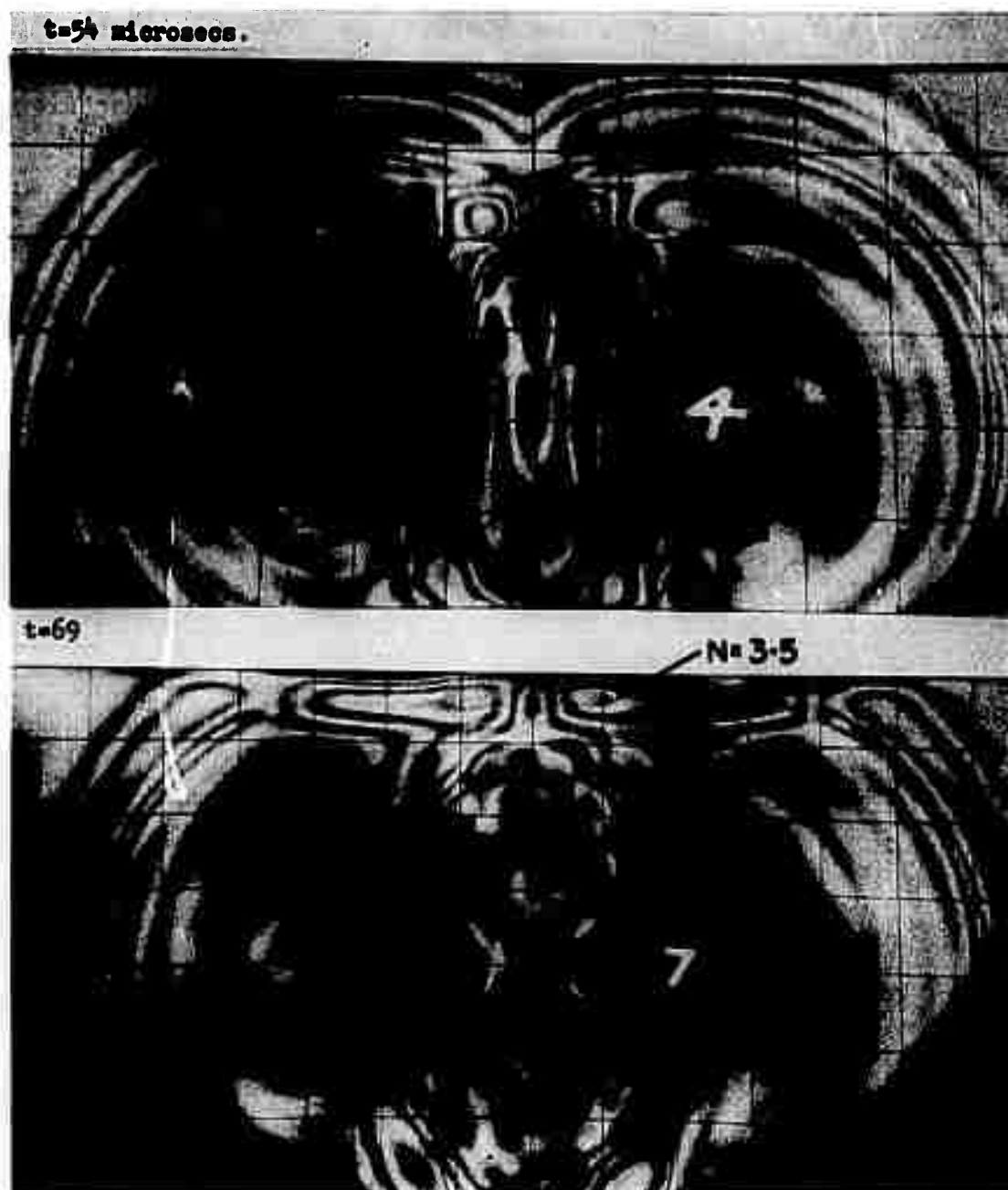


Fig. 4.13A Reflection Behavior for the Model with $h/\lambda = 2$ and $s/\lambda = 2$.

fringe peaks have divided in two peaks associated with each of two sources. One peak moves towards the centerline between the two sources and the other moves away. Actually these peaks are primarily due to the shear wave PS which is being generated during the reflection process. The peaks near the vertical centerline are larger in magnitude because the PS wave from the right hand source is being reinforced by the incident P wave from the left hand source. Maximum reinforcement appears to occur in frame 9 of Fig. 4.13B when the two PS waves, two PP waves and the tails of the two P waves simultaneously occupy the region on the centerline a distance $d = 0.4$ in. below the boundary.

This reinforcement is extremely short in duration as the six waves move out of coincidence. The rapid attenuation of the fringe maxima occurring along the centerline is evident in the fringe patterns of Fig. 4.14 where frames 10, 11 and 12 are shown. The reflected shear waves cross each other in frame 12 and continue to produce high stresses in the region below the free boundary off of the center-line.

To obtain a better understanding of the stress variation in this region, curves of fringe order as a function of position x along a line parallel to the boundary at a depth $d = 0.3$ in. are presented in Fig. 4.15. In the early time interval of the post-reflection period for $69 \leq t \leq 77 \mu \text{ sec}$, higher fringe peaks are clearly evident between the sources as compared to the regions removed from the sources. Later the shear waves cross and the same order fringe peaks are

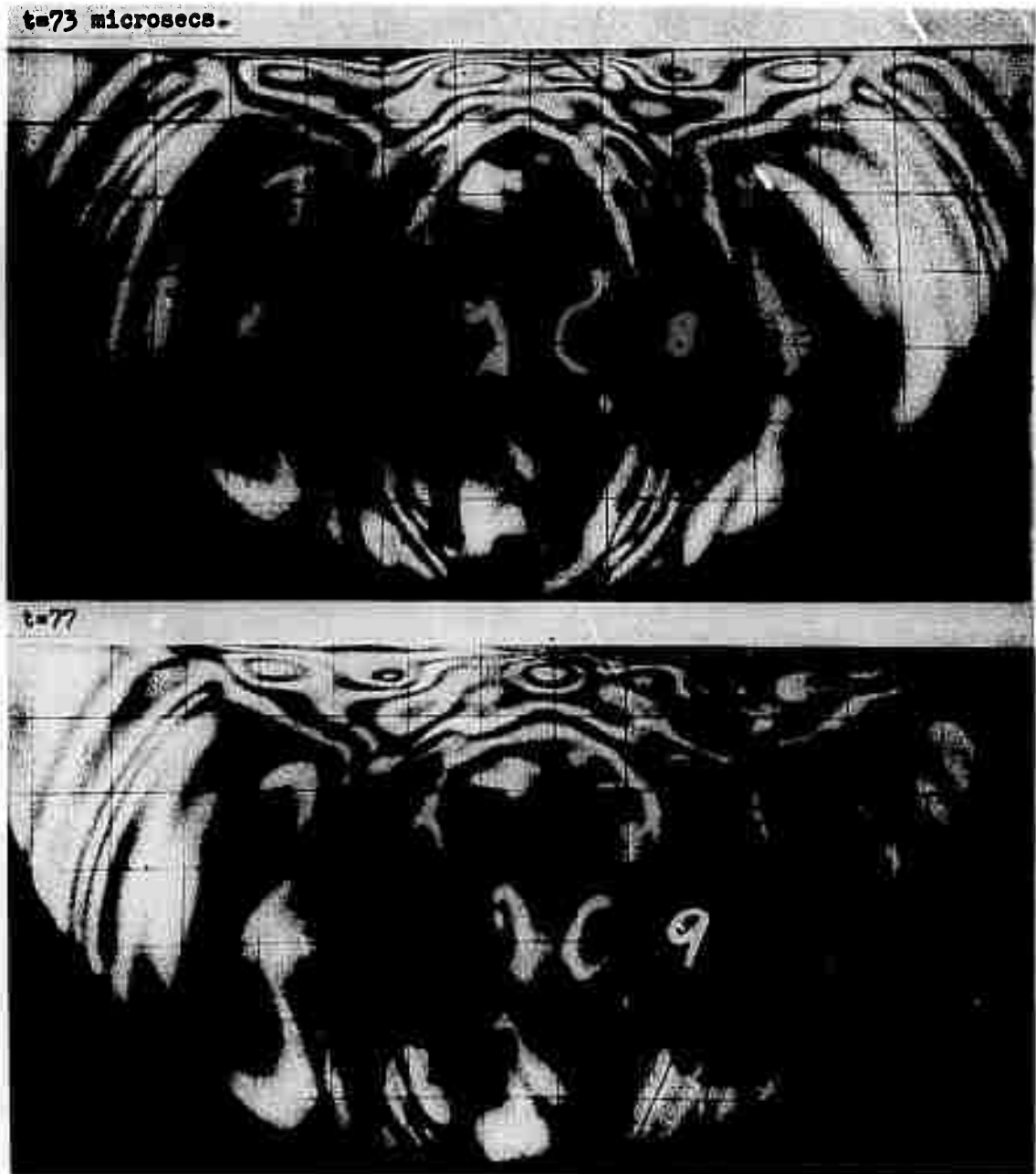


Fig. 4.13B Reflection Behavior for the Model with $h/\lambda = 2$ and $s/\lambda = 2$.

$t=80$ microsecs.



$t=84$

$PS_L + P_R$



$t=88$



Fig. 4.14 Rapid Attenuation of the Fringe Maxima along the Centerline.

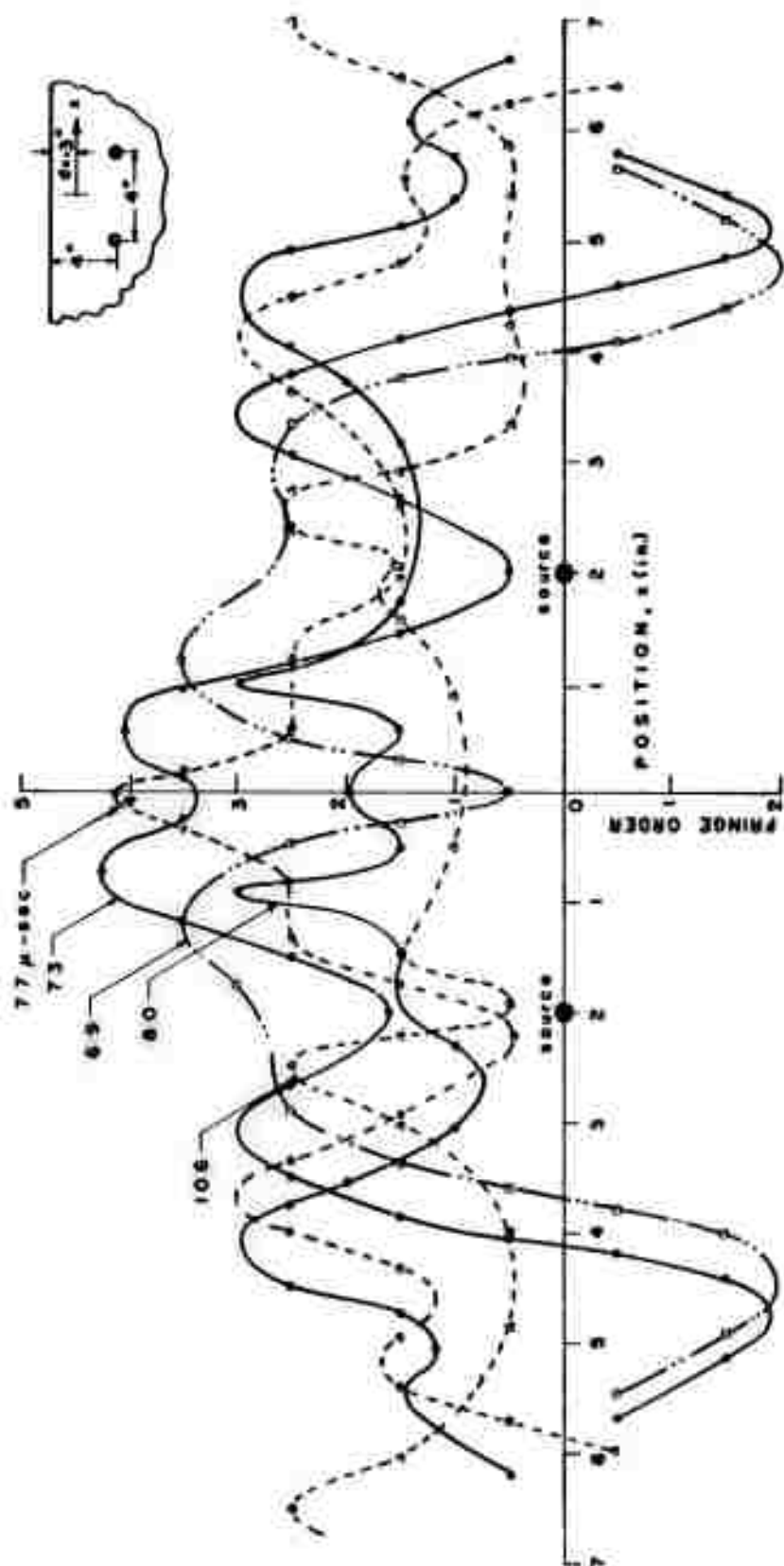


FIG. 4.15 FRINGE ORDER AS A FUNCTION OF POSITION.

($h/\lambda = 2$, $s/\lambda = 2$)

observed on both sides of each source. Finally the curve for $t = 106 \mu \text{ sec.}$ is comparable in magnitude to the curve for $80 \mu \text{ sec.}$ showing clearly that attenuation of the PS wave in this region is quite small.

Examination of Fig. 4.14 also shows another pair of fringe peaks 1 to 2 inches below the boundary just outside the two vertical lines passing through the sources. The formation of the peak on the right is due to the reinforcement provided by the combination of the incident P_L wave (subscripts L & R refer to the left and right hand sources) with the reflected PS_R wave. Similarly the formation of the peak on the left is due to the interaction of the P_R and PS_L waves.

The dynamic event proceeds in a similar fashion when S/λ is increased from 2 to 3, 4 and 5. The stresses near the boundary are primarily due to the PS wave and as such attenuation is relatively small as S/λ is increased. The value of N_{MAX} regardless of time of its occurrence in the scabbing zone near the boundary is shown as a function of position x for values of $S/\lambda = 1$ to 5 in Fig. 4.16. Here it is evident that spacing parameter $S/\lambda = 1$ produces the maximum response due to the reinforcement of the incident P wave before the initiation of the reflection process. The increase of S/λ to values higher than one results in a modest decrease in N_{MAX} with the most significant drop occurring as S/λ increases from one to two. The decrease in N_{MAX} is quite small as S/λ goes from two to five. This attenuation is illustrated by the curve in Fig. 4.16 labelled N_{MAX}

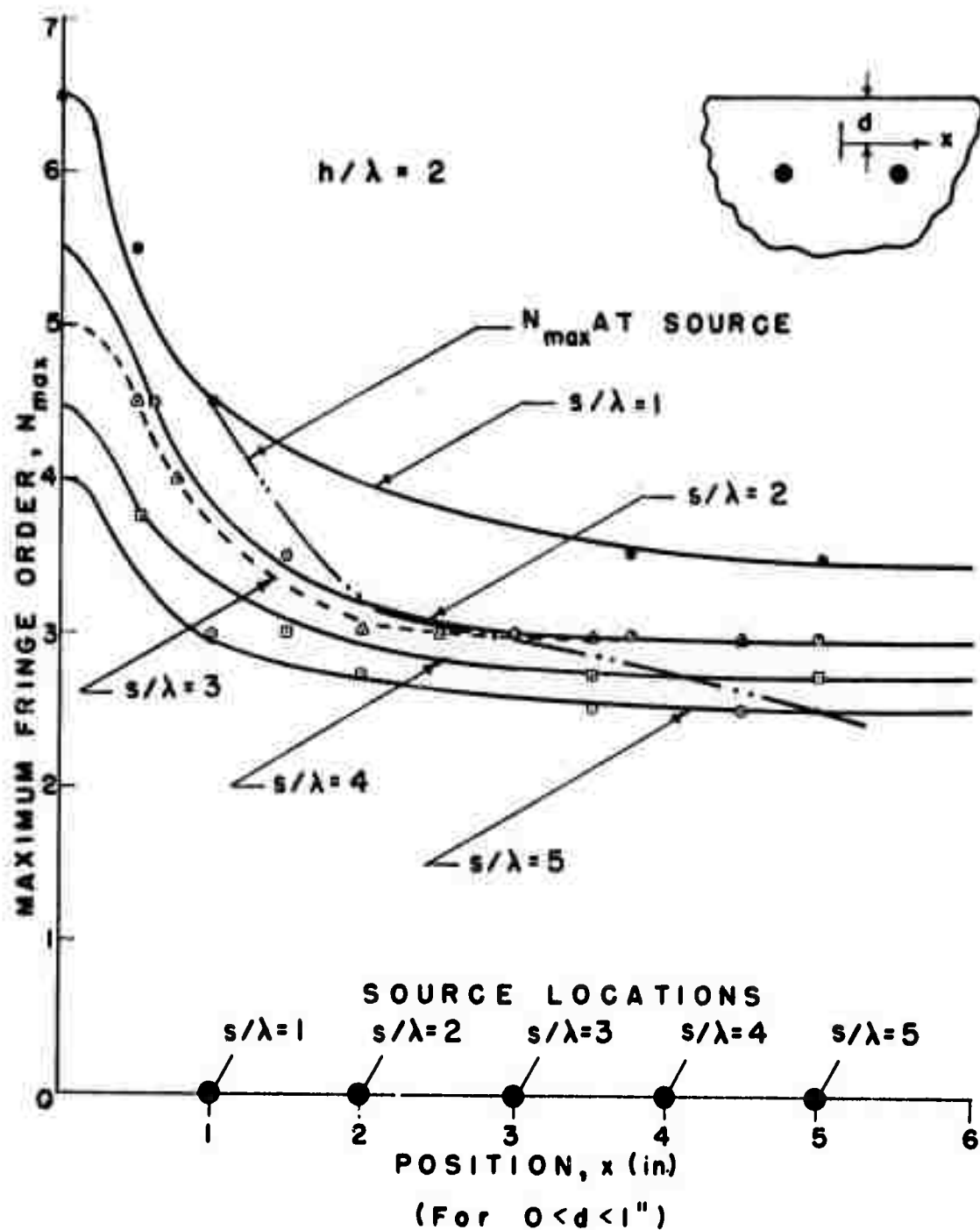


FIG 4-16 N_{\max} AS A FUNCTION OF POSITION IN THE REGION NEAR THE BOUNDARY.

at the source location.

4.3. Stress Wave Reflection Due to Three Dilatational Sources in a Half-Plane ($h/\lambda = 2$).

The observations made previously for the two source model were verified by conducting one experiment with a three source model. In this instance, the model was fabricated with $S/\lambda = 1$. With three sources the end effects are eliminated and the region between the left and right hand sources is representative of any region along a line of many sources with the same S/λ spacing.

Examples of the fringe patterns are shown in Fig. 4.17 and 4.18. In frame 3, the reinforcement of the incident P waves of all three sources is clearly evident. Indeed the front of the P wave is nearly planar and parallel to the boundary for a distance of about six inches. In frame 8, early in the reflection process, two subsurface maxima with $N = 6.5$ are formed. These peaks are due to the reflection of the combined P waves and represent superposition of PP_L , PP_C , PP_R waves with the tails of P_L , P_C and P_R waves. These two peaks move together to form a ridge with $N = 5$ in frame 9. The ridge lengthens and attenuates in magnitude as it propagates back into the model in frame 10. It is clear that the ridge depicted in frame 10 more than spans the distance $2S$ covered by the three charges. Thus, the scabbing type fracture in brittle materials should be complete and at a reasonably uniform depth below the surface.

Graphs showing the fringe order at a depth d below

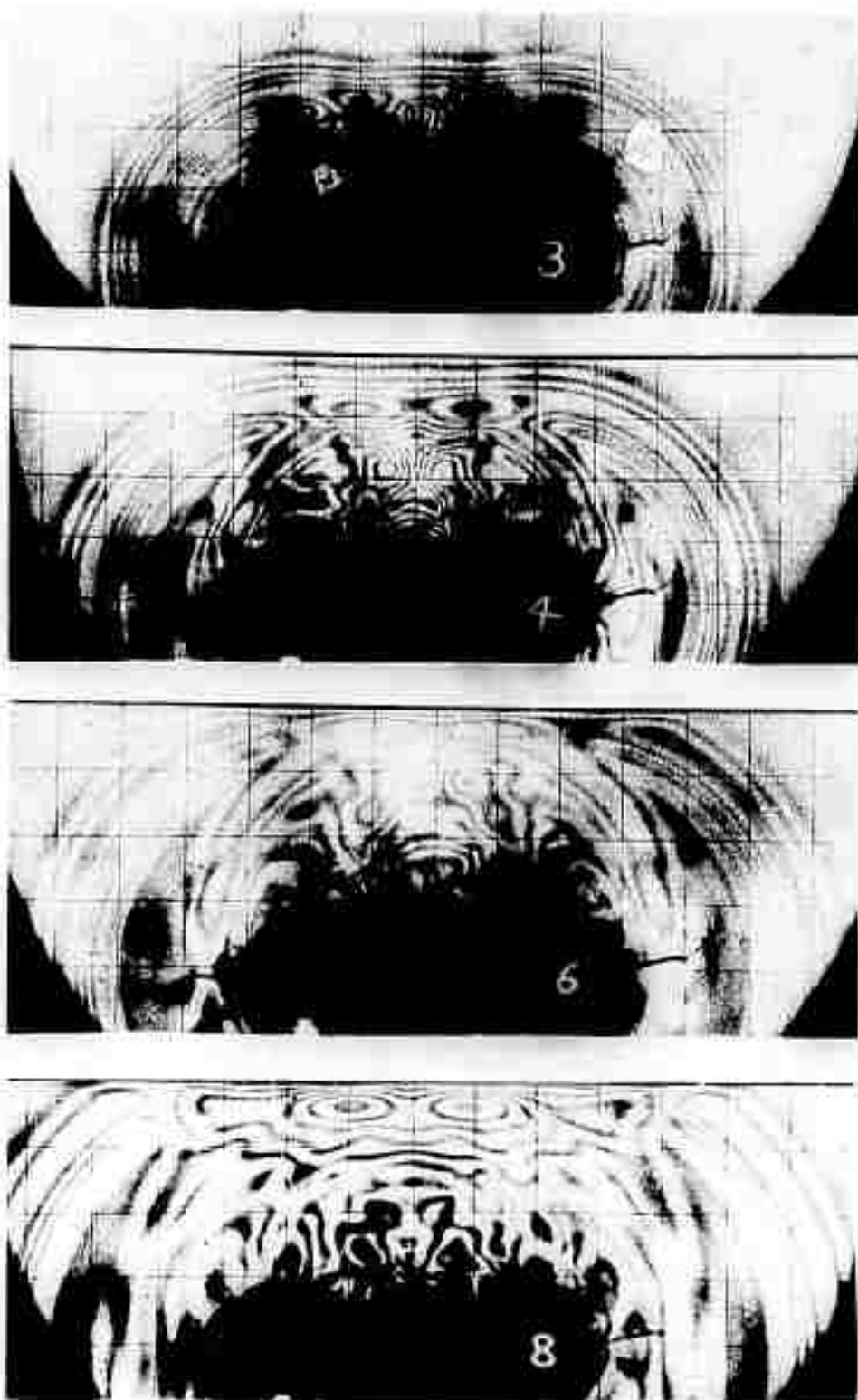


Fig. 4.17 Representation of the Early Phase Response of the Model with Three Sources.

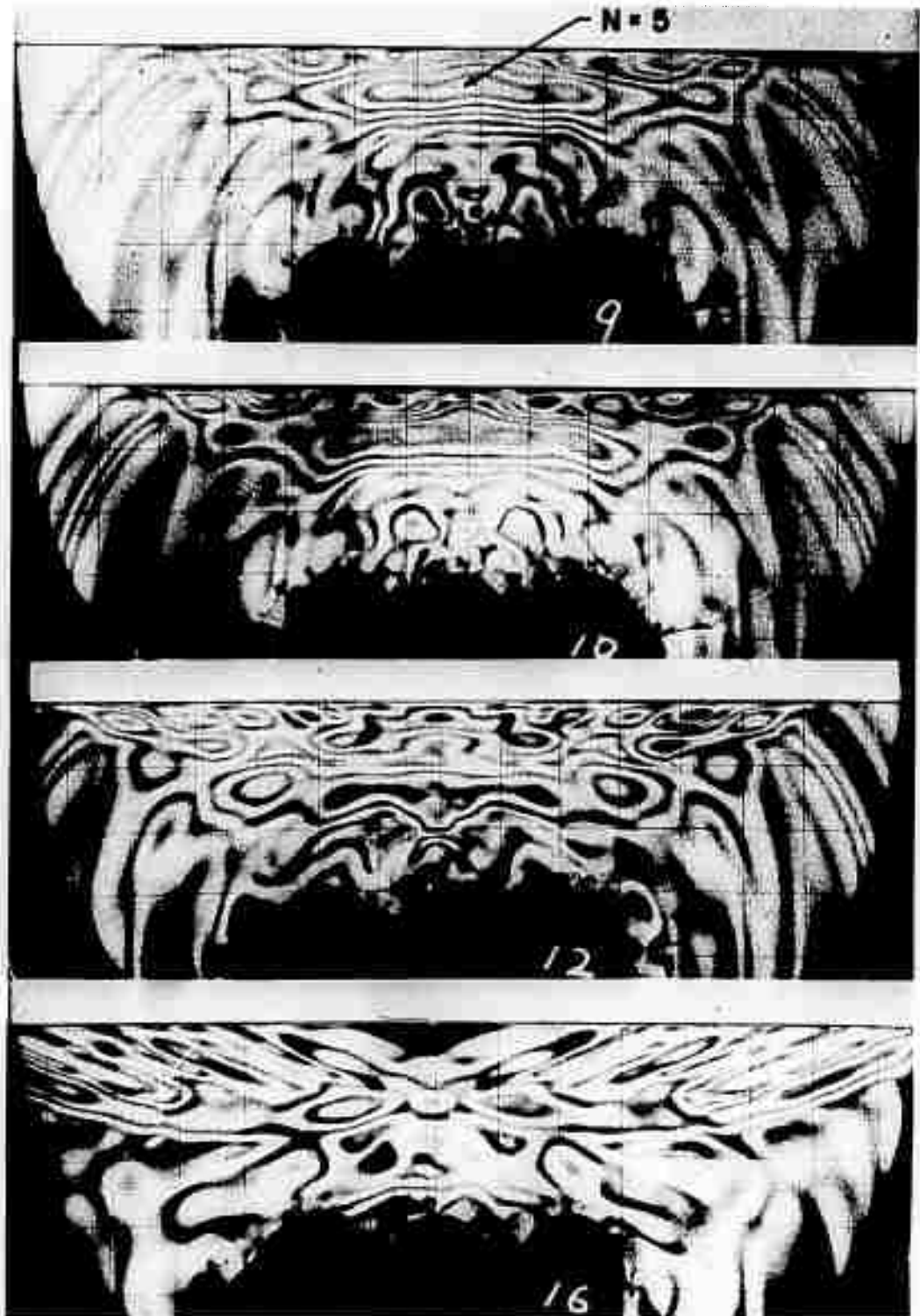


Fig. 4.18 Representation of the Late Phase Response of the Model with Three Sources

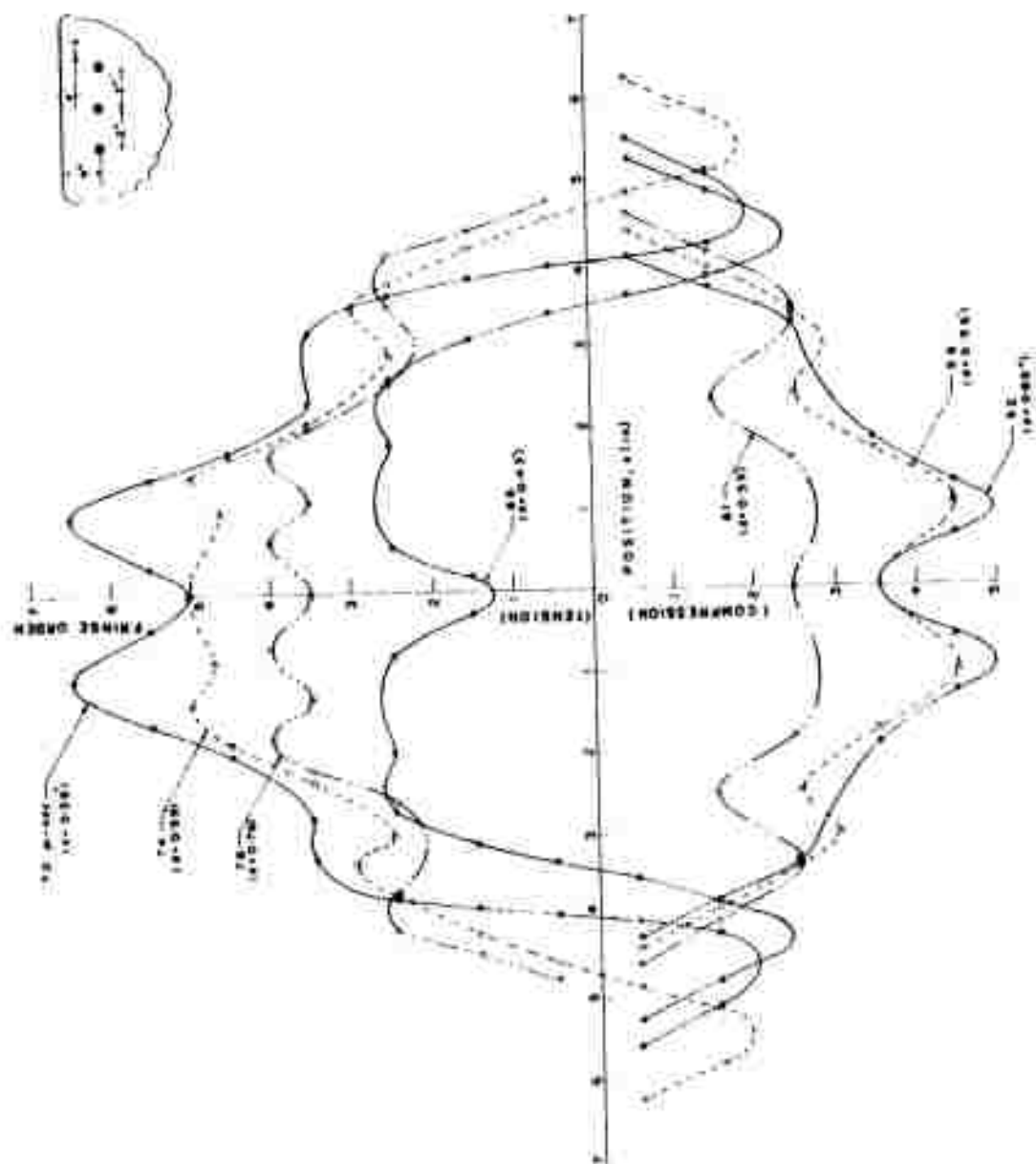
the free surface are presented in Fig. 4.19. The depth d was selected so that the position axis x would pass through the maximum fringe order. All of the features described above are indicated on this figure. The very high tensile stresses produced by the predominately P, PP wave interactions should be quite effective in inducing scabbing.

The effect of the PS wave in this model is much less significant. In the early event the P, PP wave interaction is so dominant that the PS wave is difficult to observe although it does enter in the reinforcement process described earlier. Later in the event (frames 12 and 16) after the passage of the PP wave from the critical area near the boundary, the PS wave can be observed. In the center region of the model, no significant reinforcements of the PS waves are noted. At the end of the event the three PS waves have all separated and are propagating out of the field of view without interaction.

4.4. Stress Wave Reflection Due to a Pair of Dilatational Sources in a Half-Plane ($h/\lambda = 1$)

The post reflection behavior of stress waves becomes extremely involved when the sources are brought closer to the free boundary. Quantitative interpretations are especially difficult when the distance S between the sources is small. Also, when the distances h and S are both small, the stresses are quite high producing large fringe gradients and a loss of resolution in the dynamic recording.

An example of the early portion of the reflection process



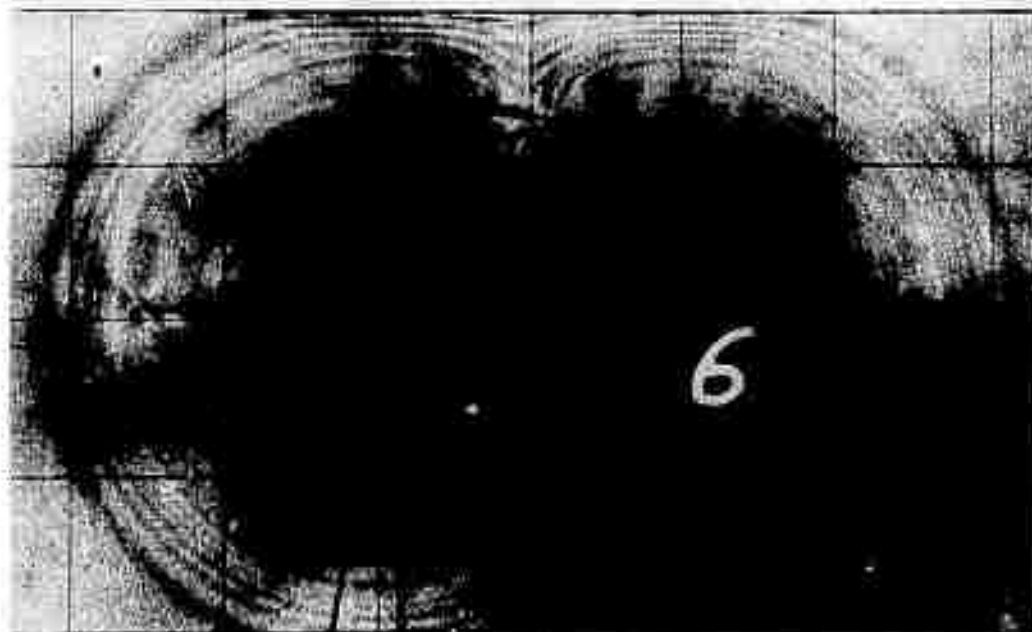
is illustrated in Fig. 4.20A and B where frames 6, 9, 10 and 11 are shown. Fringe maxima with $N = 7$ can be observed above each source in frame 9. The peak above the right hand source results from the superposition of the P_L incident pulse, the PP_R reflected pulse, the tail of the P_R wave and probably the PS_R wave. A similar reinforcement occurs over the left hand source.

The extremely rapid changes in the stress patterns occur during the period $40 < t < 46$ between the exposure of frame 9 and frame 11. In frame 10, a very high fringe ridge ($N = 7$) lies over the region between the two sources. This development is a continuation of the reflection process just described where the P waves are predominate and where the shear waves play a more minor role.

Three μ sec. later in frame 11, the reflected shear waves and reflected dilatation waves are both important. The two fringe peaks $N = 7$ over the sources are due primarily to PP wave reinforcement of the P_L and P_R waves. Other fringe maxima at the extremes are due to the shear waves PS ($N = 6$) reinforcing the tails of the incident P waves. The interaction of the PS_L and PS_R waves in the center yields a fringe maximum of $N = 7$ on the centerline at $d = 0.3$ in.

The later portion of the reflection process is shown in Fig. 4.21 where frames 12, 14 and 16 are presented. The fringe maxima $N = 7.5$ over the sources are still evident in frame 12 and remains very strong relative to other regions in the model. The fringe peak on the centerline due to the

t=28 microsecs.



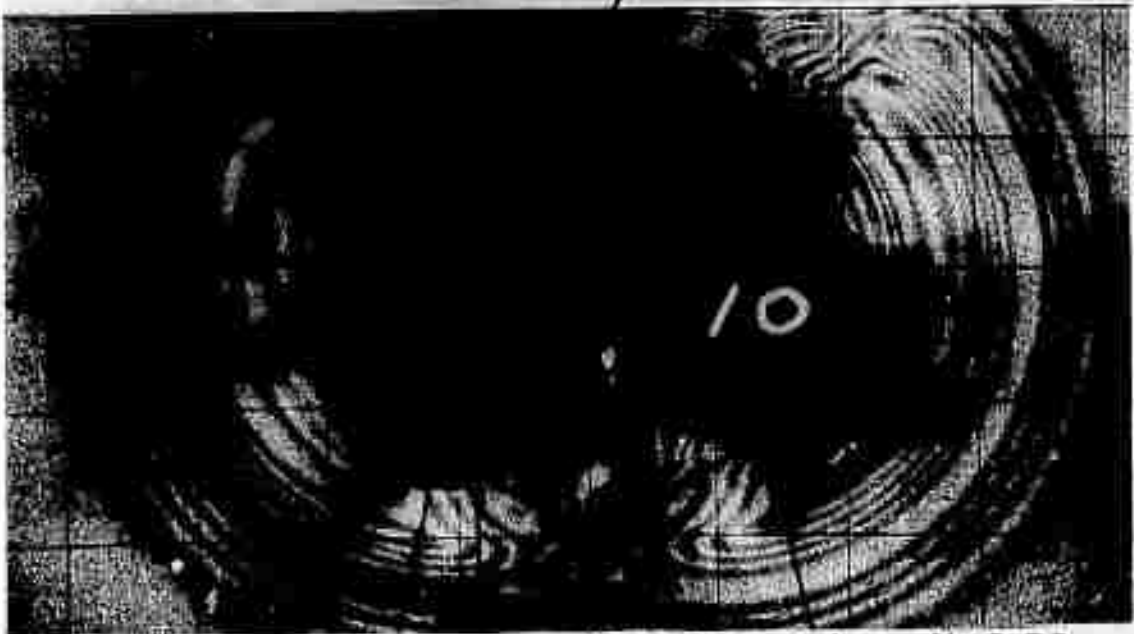
t=37



Fig. 4.20A Early Portion of the Reflection Process with $h/\lambda = s/\lambda = 1$ (frames 6 and 9)

$t=40$ microsecs.

$N=7$ RIDGE



$t=13$

$N=7$

$N=7(PS_L + PS_R)$

$N=6 PS_R$



Fig. 4.20B Early Portion of the Reflection Process with $h/\lambda = s/\lambda = 1$ (frames 10 and 11)

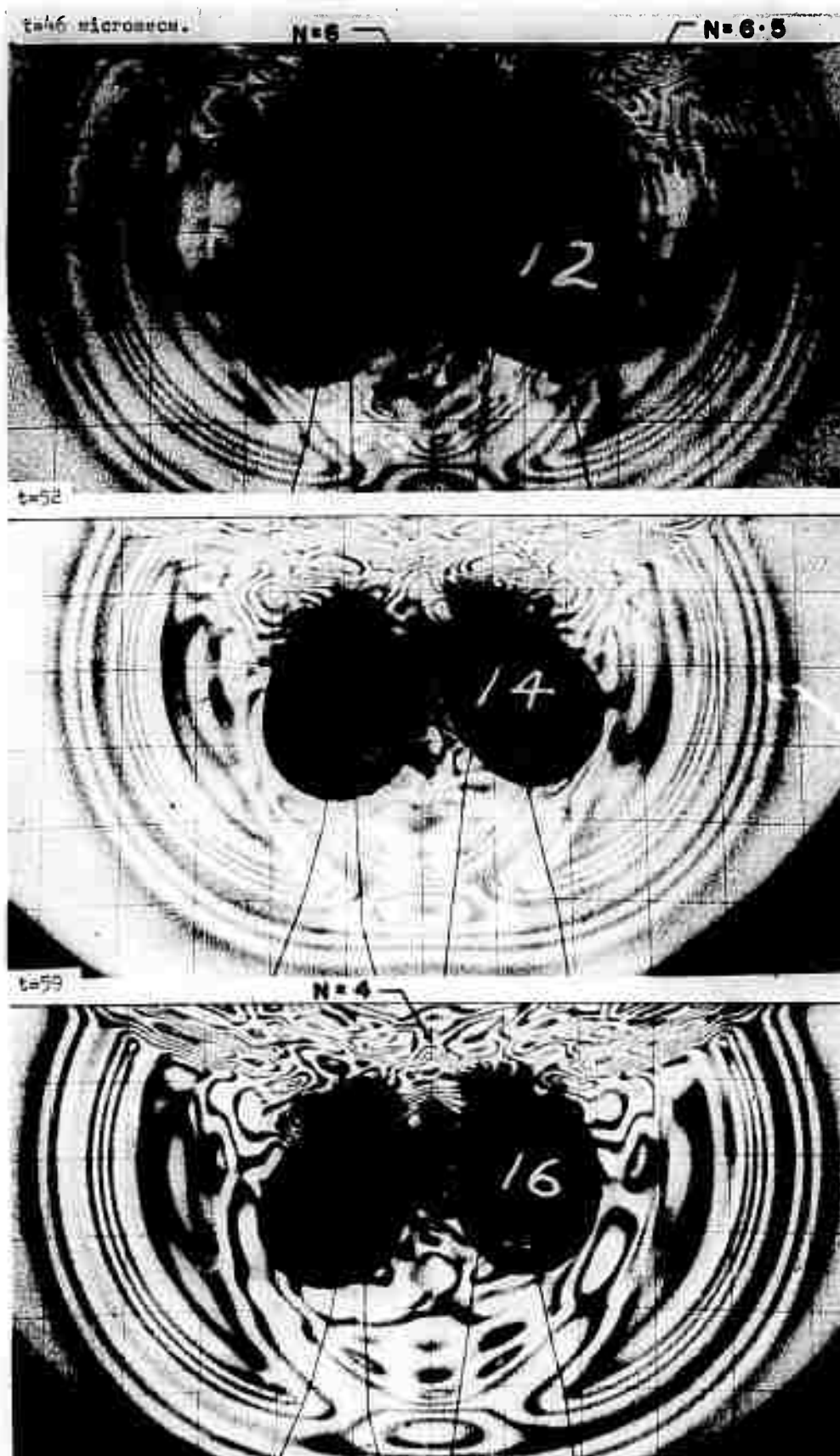


Fig. 4.21 Late Portion of the Reflection Process with $h/\lambda = s/\lambda = 1$

combination of the PS_L and PS_R has moved down and attenuated to some degree with $N = 6$. At the extremes, the PS wave and the tail of the P wave combine to give another pair of fringe maxima with $N = 6.5$. Later in event, frame 16, the reinforcement of PS_L and PS_R continues with modest attenuation and a fringe peak of $N = 4$ occurs on the centerline at $d = 0.5$ in. The peaks which were previously over the sources have moved laterally and down in the field and have attenuated so much that they are no longer a primary concern. At the extremes the PS and P wave interaction still provides a high concentration of stress along ridge lines which extend approximately one inch below the boundary.

Curves showing the fringe order as a function of position x along a line parallel to the free boundary are presented in Fig. 4.22. The x axis was positioned at variable depths d so that the axis would intersect the fringe maxima. Two observations from Fig. 4.22 are apparent. First, fringe peaks between 6.5 and 7.5 fringes occur between $40 \leq t \leq 49$ μ sec at depths which range from 0.3 to 0.7 in. Second, the fringe peaks decay rapidly at the larger values of x for time $t > 49$ μ sec. It should be noted that stresses at the centerline were higher than shown here early in the event at $t = 43$ μ sec when the PP wave was dominant. This fact will be indicated in a subsequent discussion. It is apparent that stresses of significant magnitude exist between the sources for at least 10 μ sec and should facilitate the scabbing process for depths ranging from $d \approx 0.3$ to 0.9 inches.

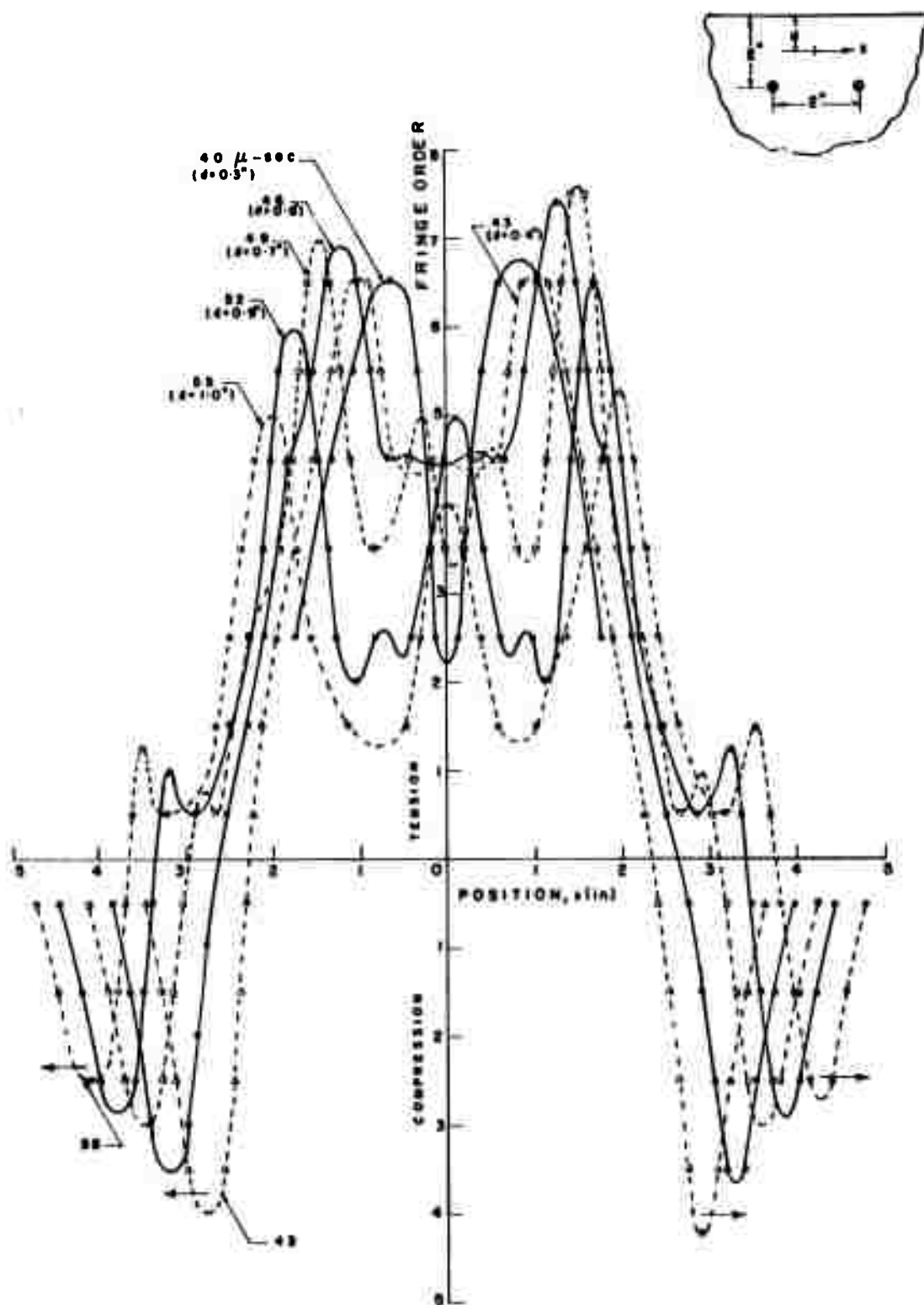


FIG. 4-22 FRINGE ORDER AS A FUNCTION OF POSITION ALONG A LINE BELOW THE BOUNDARY ($h/\lambda=1$, $s/\lambda=1$)

It is also important to note the strategic positioning of the fringe peak produced by the PS_R wave interacting with the tail of the P_L wave. Reference to frame 12 of Fig. 4.21 shows that this fringe peak and the ridge of the PS_R wave join along a straight line between the boundary and the left hand source. This long line of high stress provides a path along which cracks initiated at the source can propagate to the boundary.

The stress variation along the shear wave of one source (say the PS_L) is complicated by the interaction of the PS_R and P_R waves. As a consequence, the trends are difficult to observe; however, it is possible to show the nature of the PS wave by showing the fringe order as a function of position along its ridge line. The same geometry was examined ($h/\lambda = S/\lambda = 1$) but in a different test that utilized slower framing rates to scan a larger range of the dynamic event.

The fringe order as a function of position along the straight line ζ is shown in Fig. 4.23. The line ζ is inclined at an angle approximately 20 degrees to the boundary so that it passes through the fringe peaks in the PS_L wave. The largest fringe peak $N = 8$ at $t = 45 \mu \text{ sec}$ is due to the reinforcement provided by the P_R wave. As this reinforcement occurs for only a short interval of time, the predominate peak vanishes and subsequent fringe maxima are due primarily to PS_L wave alone.

The interaction of the PS_L and PS_R waves above the sources

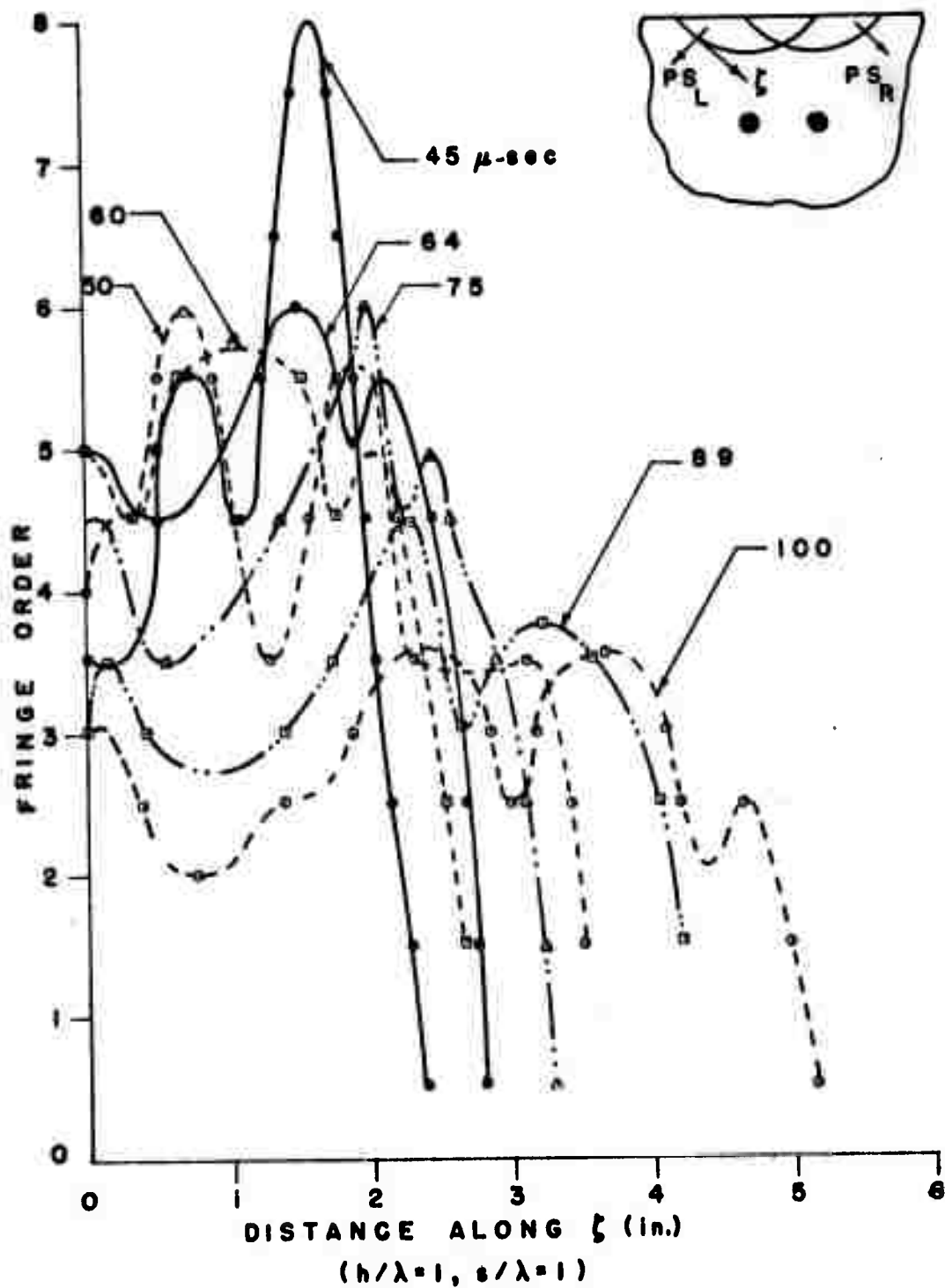


FIG. 4.23 DISTRIBUTION OF THE FRINGE ORDER ALONG THE RIDGE LINE OF A PS WAVE.

was extremely complex. Fringe maxima occurred on the vertical centerline where these two waves cross. The general features of this interaction is depicted in Figs. 4.20 and 4.21; however, the dynamic resolution of the fringe pattern is not sufficient to permit the accurate determination of the fringe order distributions along the centerlines. It is evident that very large stress exist in the region close to the boundary early in the event. These stresses on a relative scale should be sufficiently large to fracture the rock in the central region near the vertical centerline.

For other models with $h/\lambda = 1$ but with $S/\lambda > 1$, the reflected shear waves are of increasing importance. As illustrated in Fig. 4.24, the PS_L and PS_R waves interact at the vertical centerline to produce a fringe maxima on the boundary $N = 5.5$ and another maxima below the boundary $N = 5.5$ at $d = 0.5$ in. Later in the event (see frame 16) the PS_L wave interacts with the cracks propagating from the R source and vice versa. Obviously, these late event interactions of the relatively low velocity shear wave with the cracks extending from the sources are of extreme importance in improving the efficiency of the detonation process for rock removal.

Very high stress gradients are developed as the shear waves PS_L and PS_R intersect along the vertical centerline. However, the magnitude of the maximum fringe order along the centerline is not amplified by the interaction. A comparison of maximum fringe orders at the centerline with the maxi-



Fig. 4.24 Interacting Shear Waves with $h/\lambda = 1$ and $s/\lambda = 2$

imum fringe orders in the individual PS_L and PS_R waves shown in Table III indicates that all three peaks are about the same.

Table III. Comparison of Maximum Fringe Orders in the PS_L , PS_R , and the Combined $PS_L + PS_R$ Waves (for $h/\lambda = 1$, $S/\lambda = 2$)

Time (t) μsec	Depth (d) in.	N_{MAX}		
		PS_L	PS_R	$PS_L + PS_R$
55	0.28	5.5	5.5	5.5
60	0.44	5.5	5.5	5.5
64	0.64	5.3	5.3	5.0
68	0.85	4.5	4.5	4.3
72	0.95	4.5	4.5	4.5
75	1.10	4.5	4.5	4.3

The minor variations in N_{MAX} are not important as they result from random fluctuations produced by the stresses in the tails of the P and PP waves.

The maximum stresses are not produced by the interaction of the PS_L and the PS_R at the vertical centerline. Instead, the P_L , P_R , PP_R , PP_L and PS_R all combine to produce a fringe maxima ($N = 10$) just to the right of the vertical centerline a distance $d = 0.25$ in. below the free boundary. This fringe maxima and a similar one just to the left of the vertical centerline is shown in frame 5 of Fig. 4.25. These fringe peaks attenuate quickly because the five waves which combine to produce them do not stay combined. Note that from frame 5 to 6 the fringe maxima decreased from 10 to 7.5 in the 5 μsec . interval. After another 9 μsec .

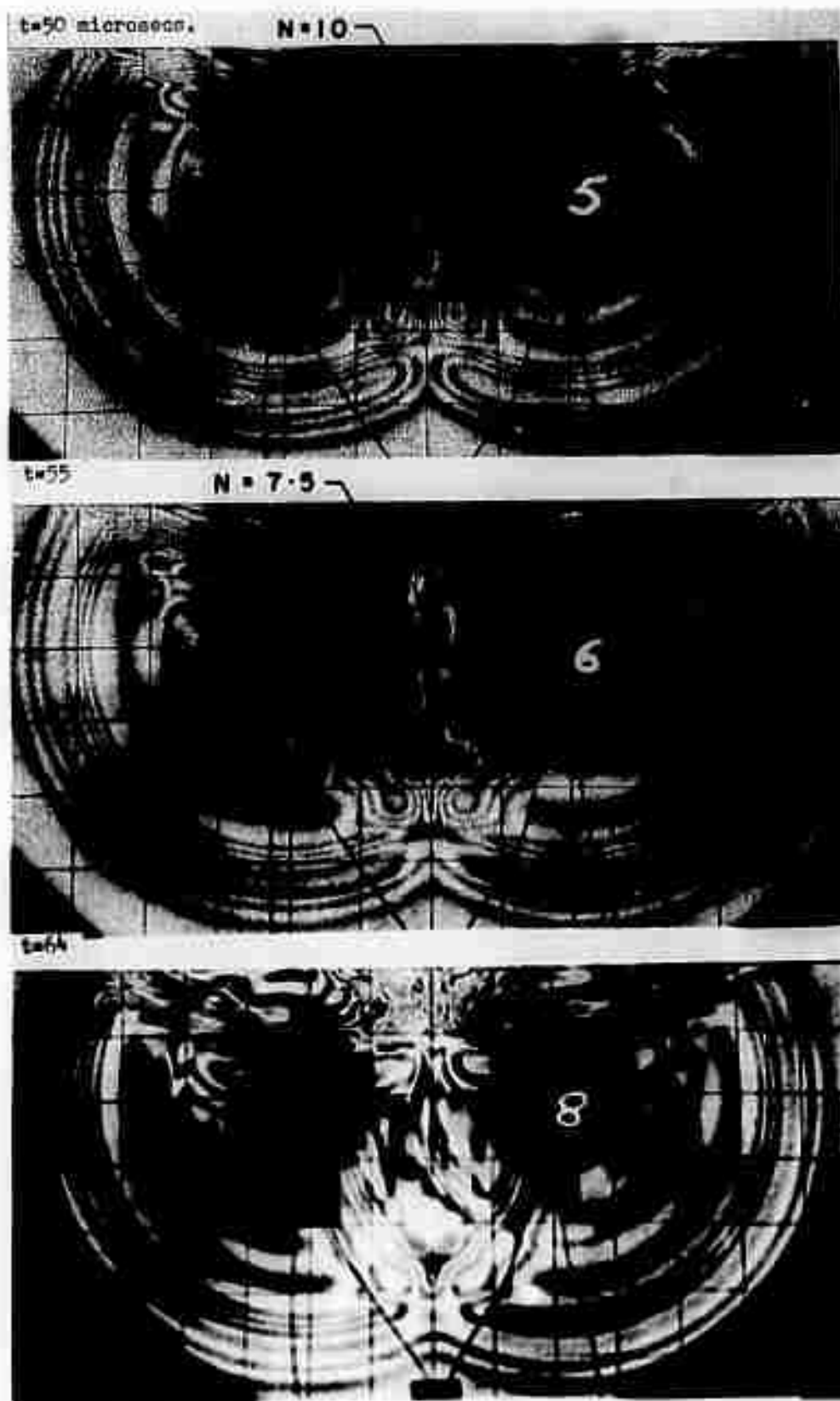


Fig. 4.25 Reinforcement of the P, PP and PS Waves

(frame 8), the P and PP waves have moved out of the region of interest and the central region contains five peaks and four valleys indicating the final phase of the interaction.

As the reflected shear waves move down in the field, the PS_L wave approaches the R source and vice versa. The interference of the reflected shear waves with the fracture zone about the charges is illustrated in Fig. 4.26. The shear stresses are relatively high to the left and right sides of both sources, but even higher in the center zone between the sources (see frame 15). If the material between the charges has not been completely fractured, these PS waves containing a tensile component of stress should aid significantly in extending the crack fronts and in completing the fracture of the face along the line of charges.

For models with larger values of S/λ (greater than 2), the distribution of the stresses is quite similar except that the PS_L and PS_R waves intersect each other after a longer period of time. As shown in Fig. 4.27 (frame 11) the P, PP and PS interaction is still quite strong with $N = 6.5$ at a distance $d = 0.8$ in. below the boundary. Later in the event the coincidence of the P, PP and PS waves is lost and the familiar multipeak and valley pattern is formed in the central region as illustrated in Fig. 4.28.

The fringe order distribution along the vertical centerline for the model with $S/\lambda = 3$ is shown in Fig. 4.29. The maximum on the free boundary at $t = 59 \mu$ sec results from the P, PP and PS wave interaction and reinforcement. The subse-

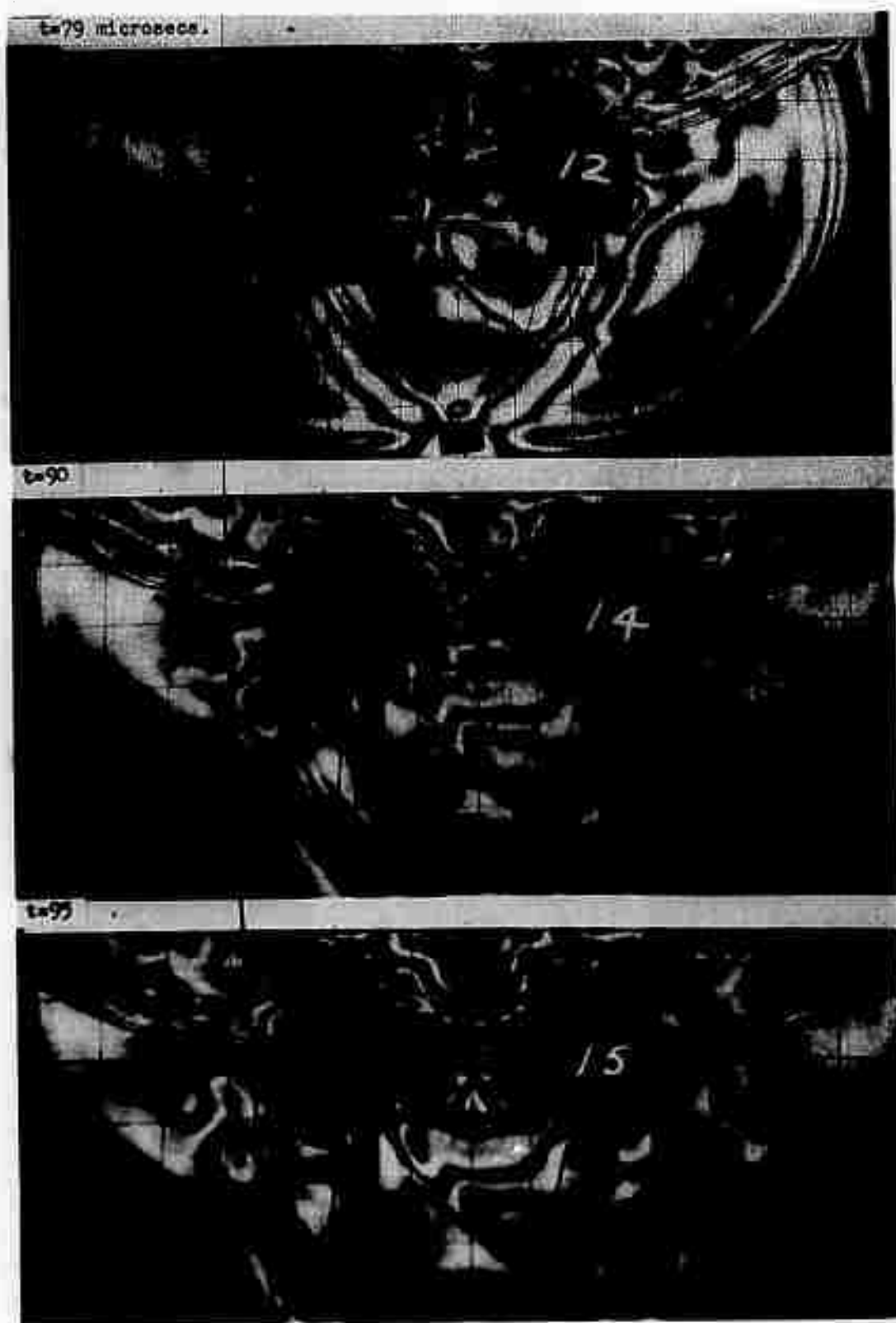


Fig. 4.26 PS Wave Interaction with the Sources

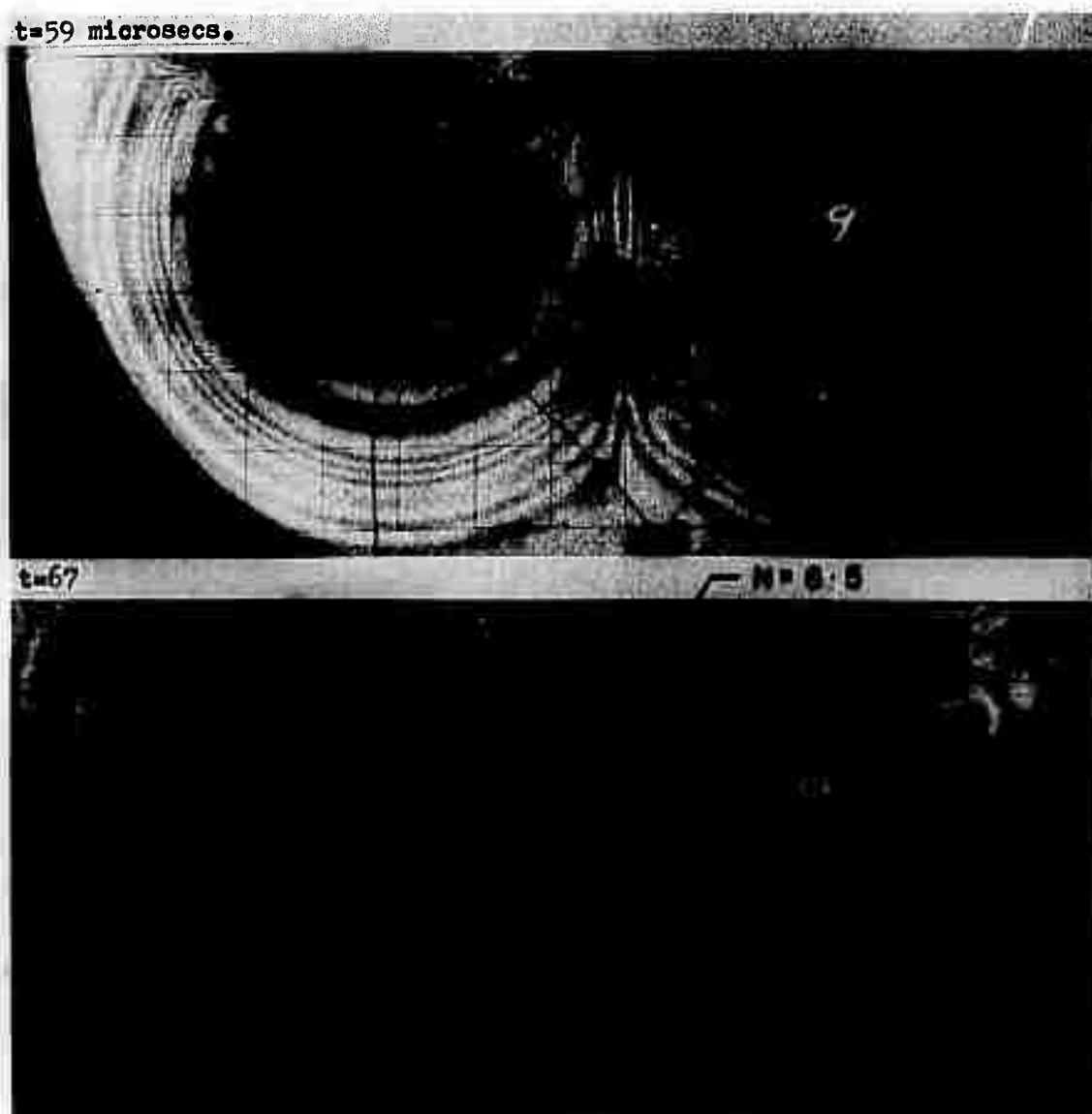


Fig. 4.27 Reinforcement of P, PP and PS Waves with $\epsilon/\lambda \approx 3$

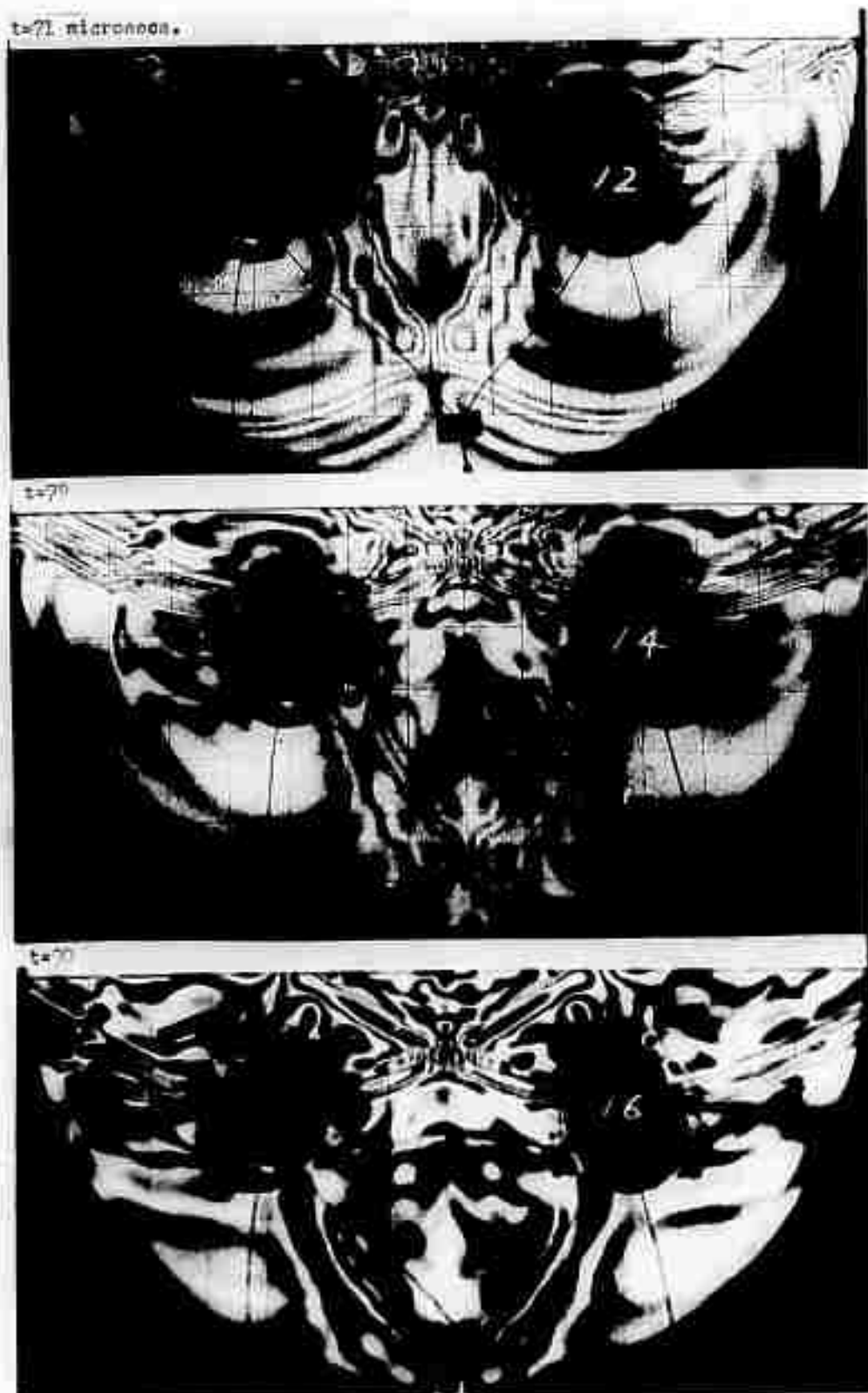


Fig. 4.28 Interaction of PS_L and PS_R Waves

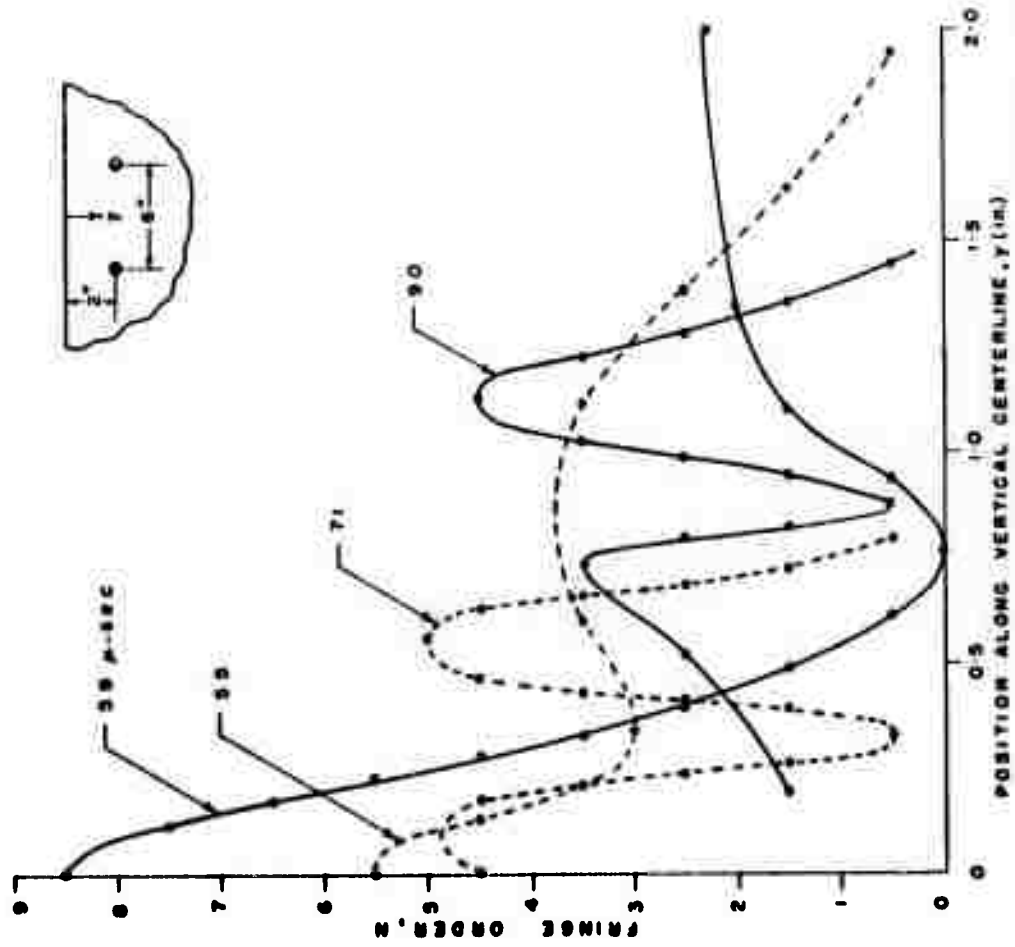


FIG. 4-29 FRINGE ORDER AS A FUNCTION OF POSITION ALONG THE VERTICAL CENTERLINE ($h/\lambda=1$, $s/\lambda=3$)

quent peaks at $t = 71$ and $90 \mu \text{ sec}$ are due to the intersection of the PS_L and PS_R waves.

To compare the stresses produced as a result of the (PS_L and PS_R) and the (P, PP, PS) interactions with the stresses which occur in a non-interacting PS wave, fringe orders were determined along the ζ and η axes defined in Fig. 4.30. The ζ axis coincides with the ridge line through the PS wave and the η axis coincides with the ridge line through the interacting PS waves. A casual inspection of these fringe distributions shows an enhancement of the stresses due to the interaction. The interacting stress waves exhibit fringe orders which are up to 60 per cent higher. Also, the increase in the fringe order extends along the wave front for a distance of three inches.

Along the η axis, the peak at the boundary occurring at $t = 59 \mu \text{ sec}$ is due to P, PP and PS interaction. The pre-dominate peak at $t = 67 \mu \text{ sec}$ is a result of the PS_L and P_R reinforcement and the secondary peak ($N = 4.5$ at $\eta = 0.75 \text{ in}$) occurs due to the PS_L and PS_R interaction. As the event proceeds, the peak due to the P and PS interaction attenuates and the PS_L and PS_R reinforcement predominates at $t = 79 \mu \text{ sec}$.

Unlike the sharp variations in fringe order distribution along η , the distribution along ζ is much more constant with respect to time and position. The maximum fringe order varied only by $1/2$ over the time interval from 59 to $71 \mu \text{ sec}$.

Three models with $h/\lambda = 1$ were evaluated with $S/\lambda = 1$,

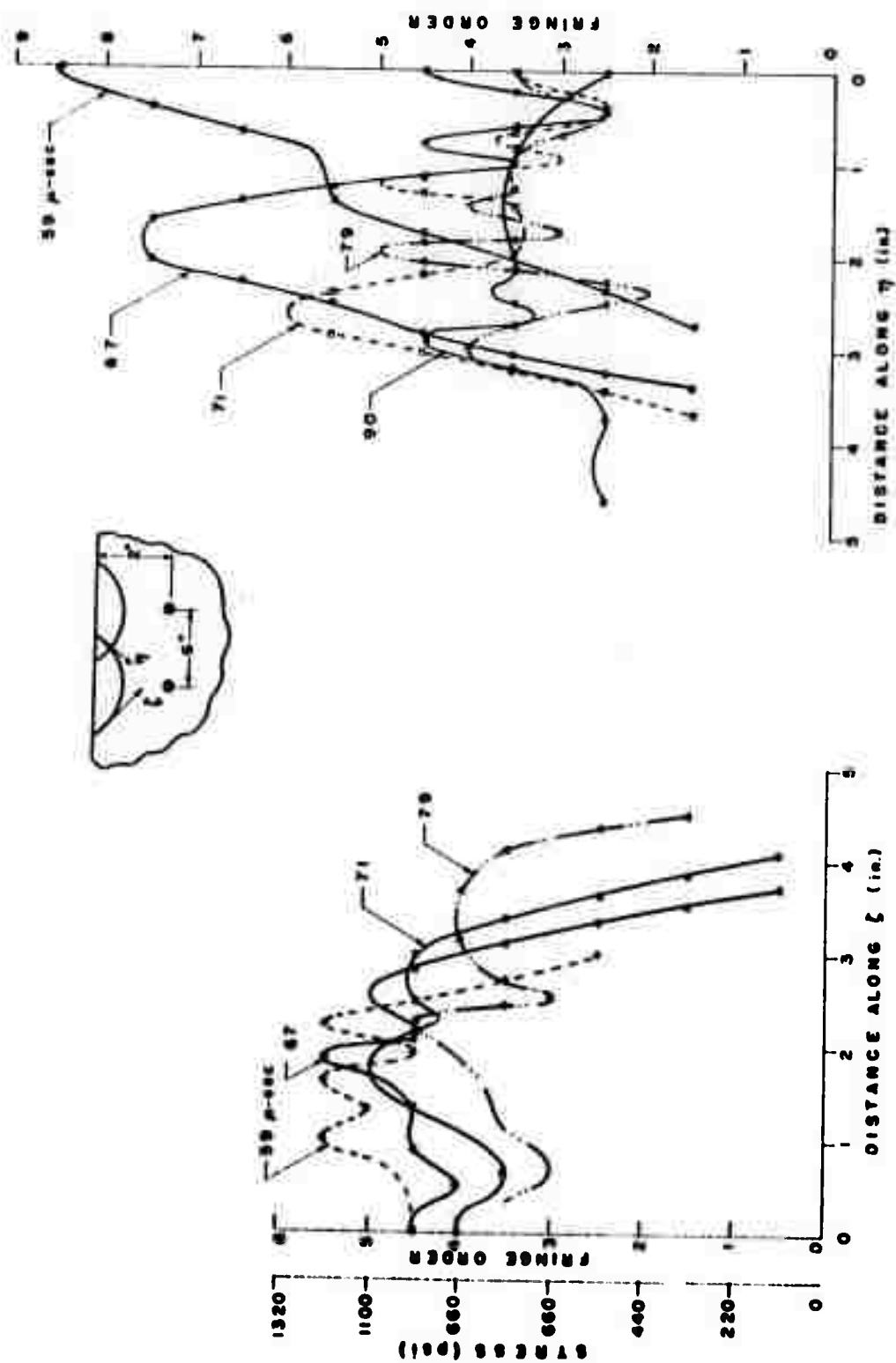


FIG. 4-30 COMPARISON OF STRESSES ALONG THE P-S WAVES.

2 and 3. The maximum fringe order as a function of position x between the two sources is shown in Fig. 4.31. These distributions for the three models were established using different times and different locations d for each point. It is evident that N_{MAX} drops sharply as x increases for all three cases. The stresses at the centerline ($x = 0$) are the highest with $S/\lambda = 1$; however, the reduction due to increasing S/λ to 2 is quite modest. The dashed curve for N_{MAX} over the source indicates the lower bound for the three cases and indicates the maximum reduction in fringe order that occurs due to increasing S/λ .

4.5. Stresses Along the Free Boundary

The stresses which occur at the free boundary are tangent to that boundary and will produce a fracture which will aid in fragmenting the scab which is removed from the face of the bench. Of critical importance in the analysis of the boundary is the sign of the stresses. The tensile strength of rock is much lower than its compressive strength and thus the tensile stresses on the boundary determine the degree of fragmentation.

Consider first a single dilatational source in a half plane with $h/\lambda = 1$. The fringe patterns for the model were shown previously in Fig. 3.1 and in the Appendix. The boundary stresses obtained from this data are shown in Fig. 4.32. It is evident that the leading pulse which moves out along the boundary is compressive with a maximum amplitude which decreases from 4.5 to 2.5 fringes. The leading pulse is

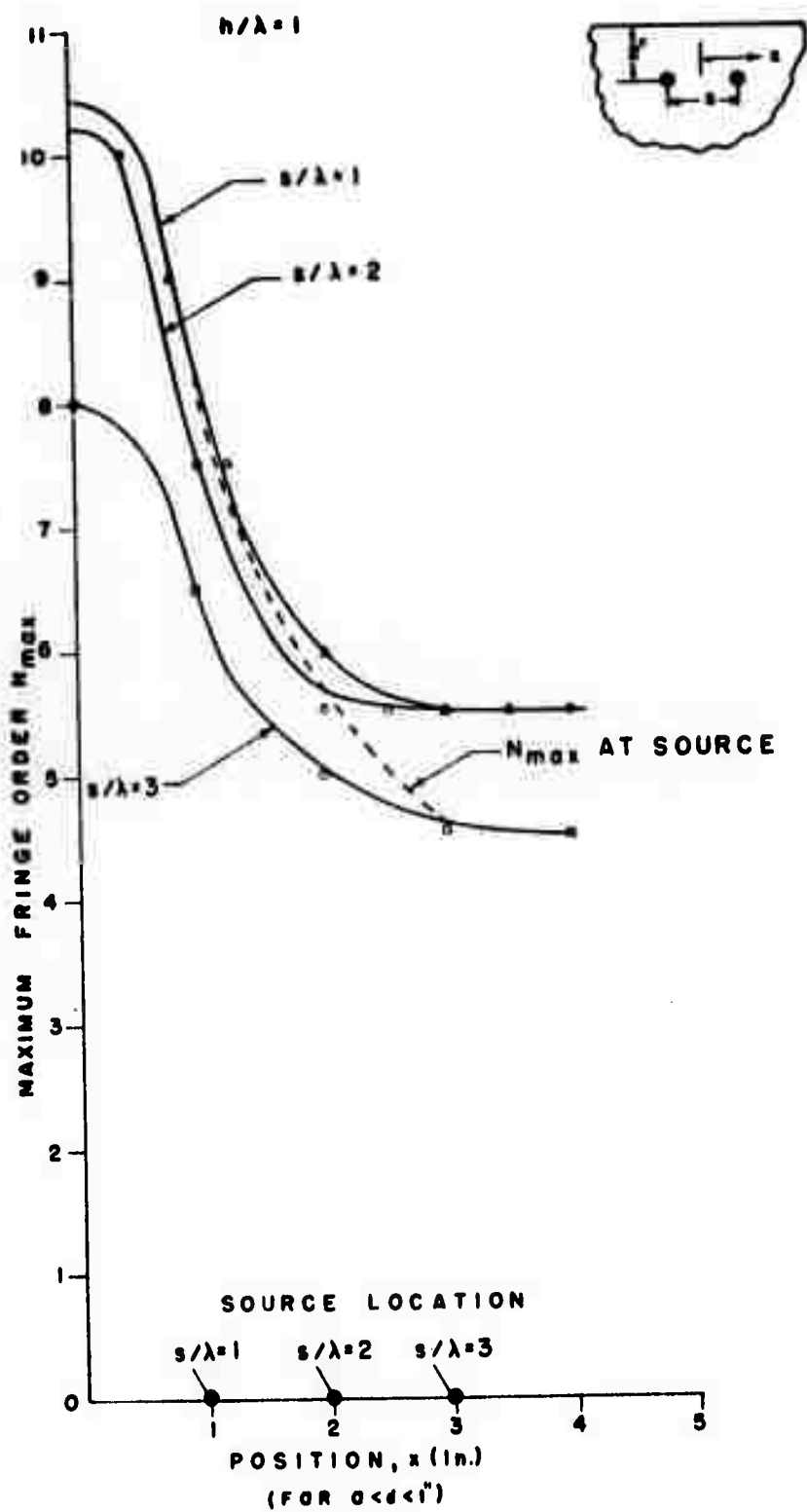


FIG. 4-31 MAXIMUM FRINGE ORDER AS A FUNCTION OF POSITION ($h/\lambda = 1$, $s/\lambda = 1, 2$ and 3)

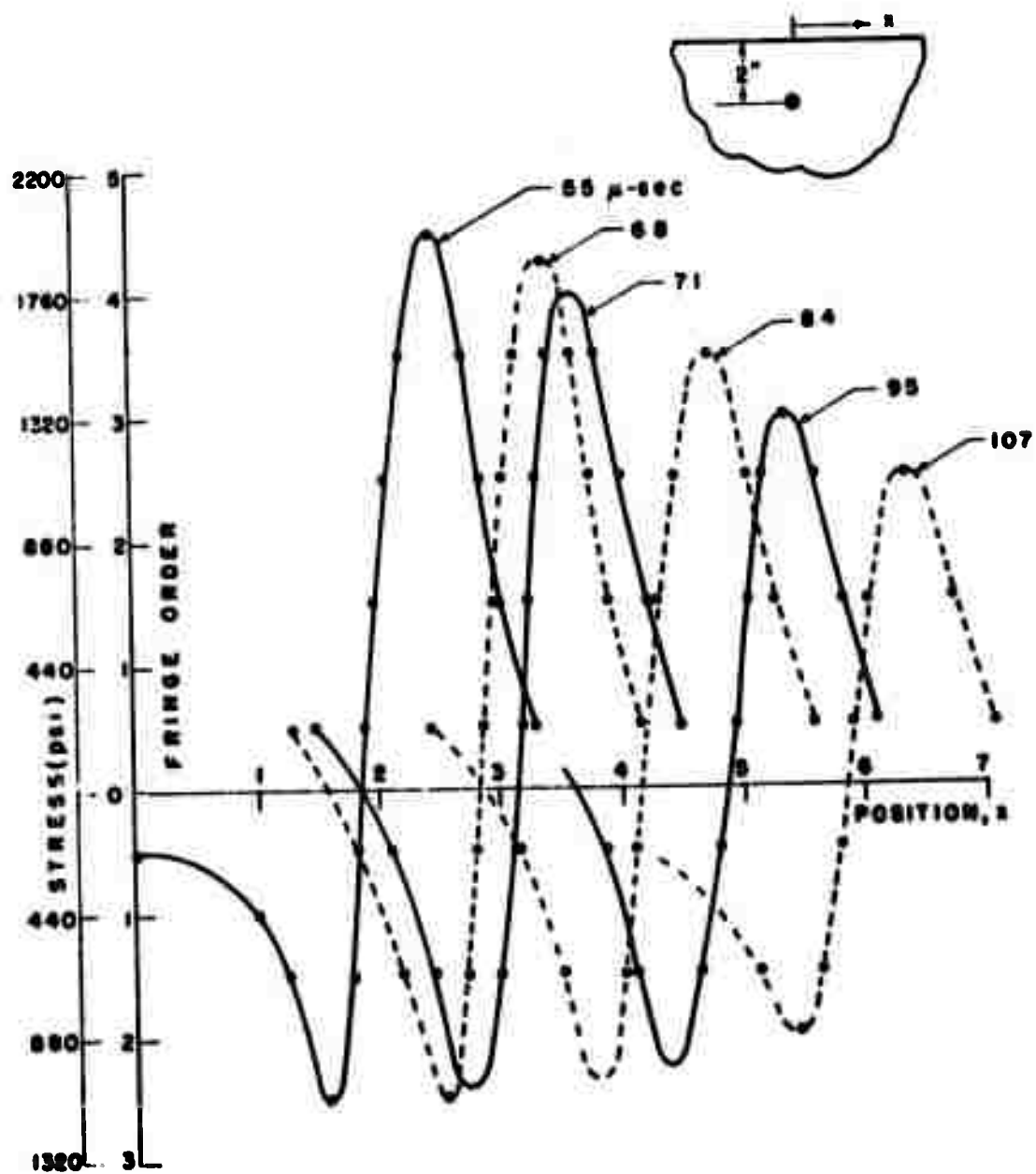


FIG. 4-32 FRINGE ORDER AS A FUNCTION OF POSITION ALONG THE BOUNDARY FOR $h/\lambda=1$, $s/\lambda=0$.

followed by a tensile tail which varies from 2.5 to 2.0 fringes. The significance of this tensile tail which should fracture the rock is increased by the fact that it is reasonably high and that it attenuates slowly with distance. For instance, the maximum tensile stress at $t = 55 \mu \text{ sec.}$ was 1100 psi compared to a compressive stress of 1980 psi in the leading tensile pulse. Later, at $t = 107 \mu \text{ sec.}$ the compressive stress has decayed to 1100 psi while the tensile stress attenuated more modestly to a level of 800 psi. It should be emphasized here that the attenuation of the stress waves is not too significant in actual mining applications. Once the rock has fragmented, some of the energy in the stress wave is dissipated and other energy is trapped in the fragment so that the actual attenuation rate will be much higher than indicated here.

When h/λ is increased, the magnitude of the boundary stresses decreases appreciably. Results for the stresses along the boundary of the model with $h/\lambda = 2$ are shown in Fig. 4.33. The maximum tensile stress for the model with $h/\lambda = 2$ is only 550 psi compared to 1100 psi for $h/\lambda = 1$. Thus, it is clear that the boundary stresses are strongly influenced by h/λ and increased fragmentation should occur as the explosive charges are moved closer to the bench face.

With double charges, two regions of tensile stress occur on each side of the vertical centerline at any instant after the PS_L and PS_R interaction has occurred. The stress distribution along the free boundary resulting from two sources with $h/\lambda = 1$ and $S/\lambda = 1$ is shown in Fig. 4.34. In this

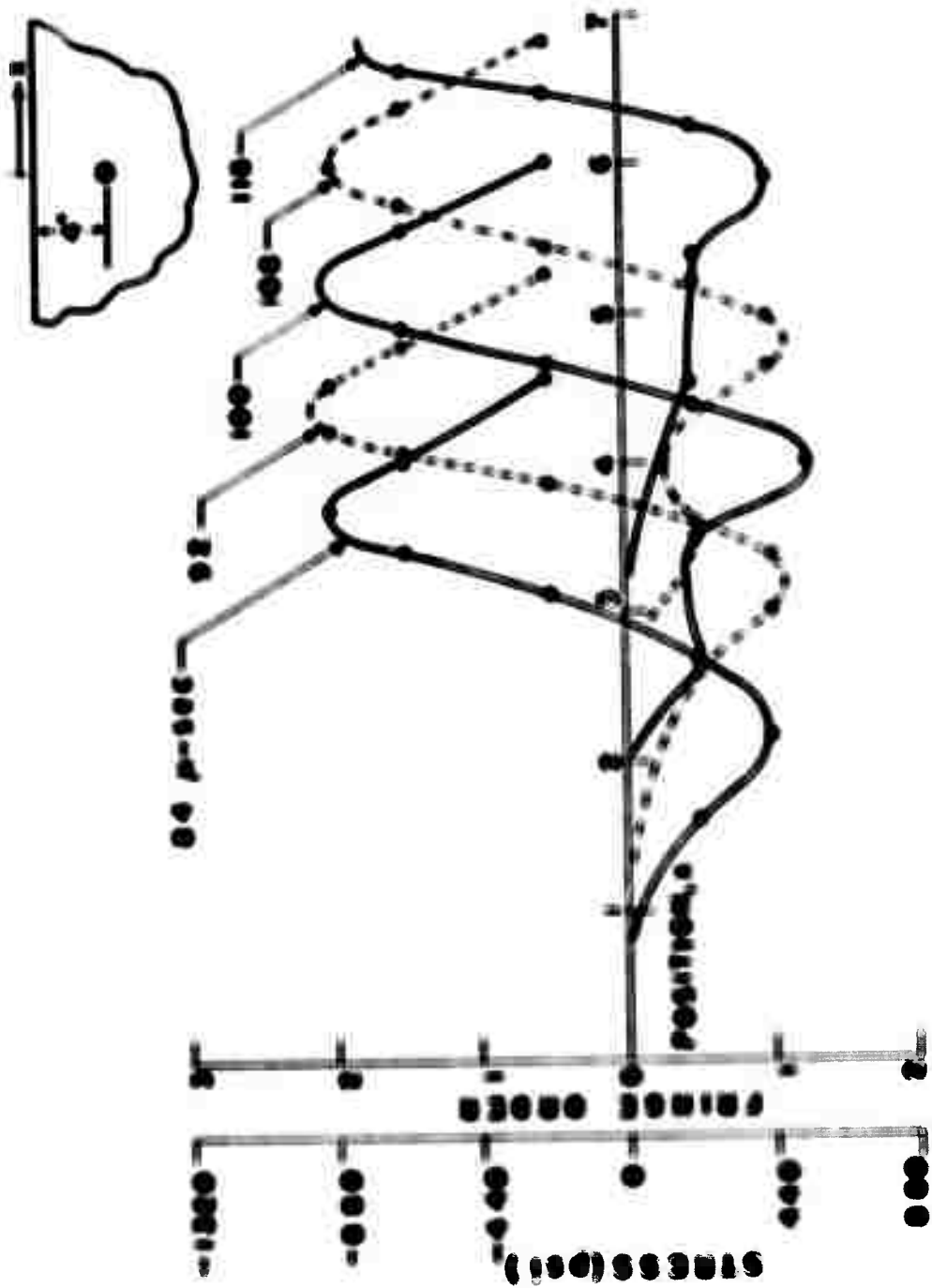
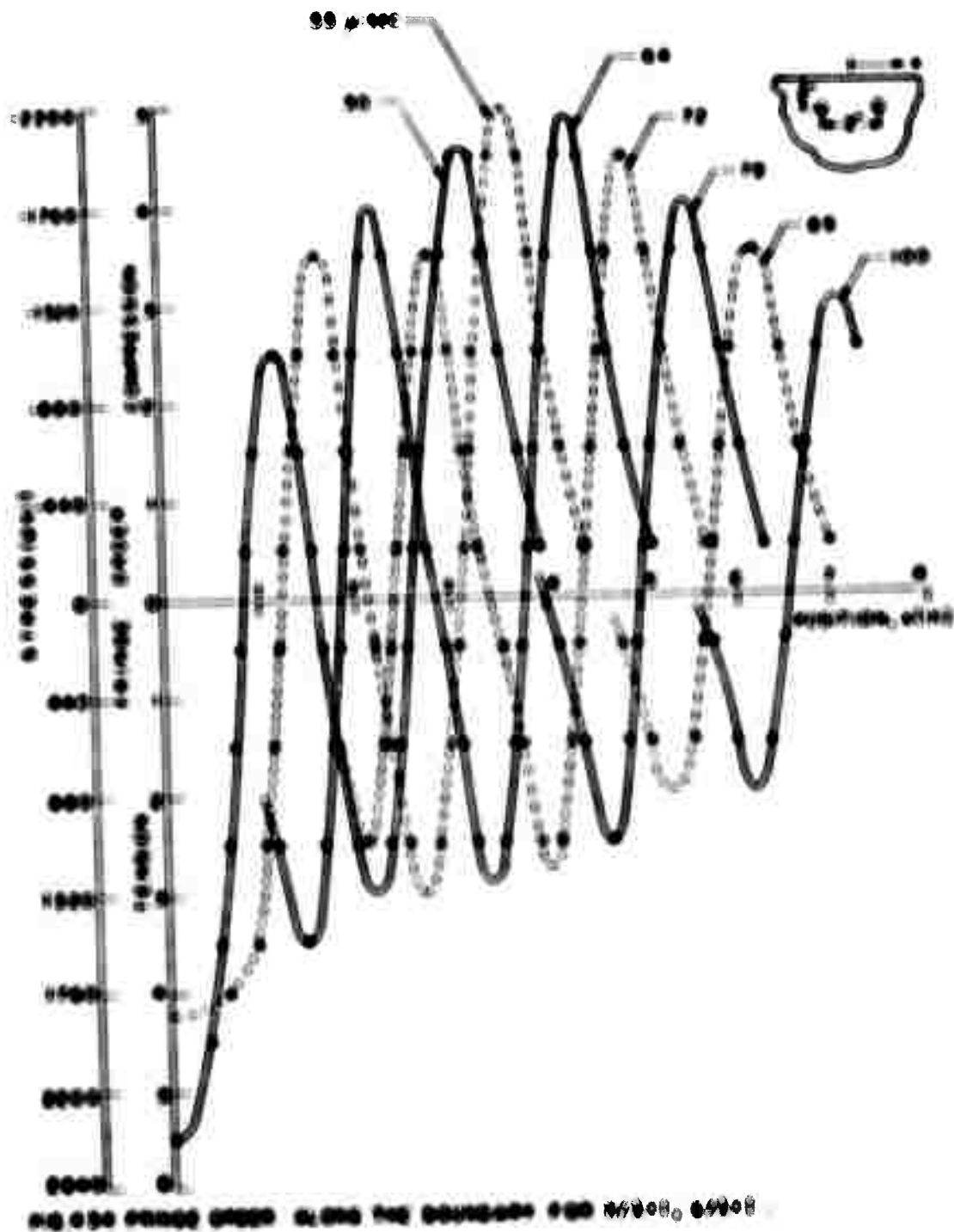


FIG. 4.33 FRINGE ORDER AS A FUNCTION OF POSITION ALONG THE BOUNDARY FOR $h/\lambda = 2$, $s/\lambda = 0$.

(190)993015



case the stress wave moving along the boundary exhibits 4 peaks. A leading compressive peak followed in order by tensile, compressive and tensile tails. Consider for example the distribution at $t = 64 \mu\text{sec}$ in Fig. 4.34. The first region of tensile stress occurs between $2.8 \leq x \leq 3.8$ and the second in the vicinity of the source. The last tensile pulse has the highest amplitude since it involves the interaction and reinforcement due to a number of different waves. Of course, in the region between the sources the very high tensile stresses produced earlier at $t = 50 \mu\text{sec}$ would probably have fragmented the rock and altered the subsequent stress distributions.

Increasing S/V has the effect of separating the two tensile regions further apart along the boundary. Results obtained for $S/V = 2$ and $S/V = 3$ (with $b/V = 1$) are presented in Figs. 4.35 and 4.36 respectively. The space between these two tensile peaks is of little significance because the leading tensile pulse is outside the control region between the two sources. In practice, with a line of distributed sources each source will have a neighbor and the interaction between adjacent sources will determine the fracture pattern. Clearly, the material between sources will be fragmented if S/V is small ($S/V \leq 1$). However, as S/V is increased to two or three, material between the sources may not be fragmented except for a region directly above the sources.

The maximum tensile stress along the boundary and between the charges occurs when the P S waves interact. The

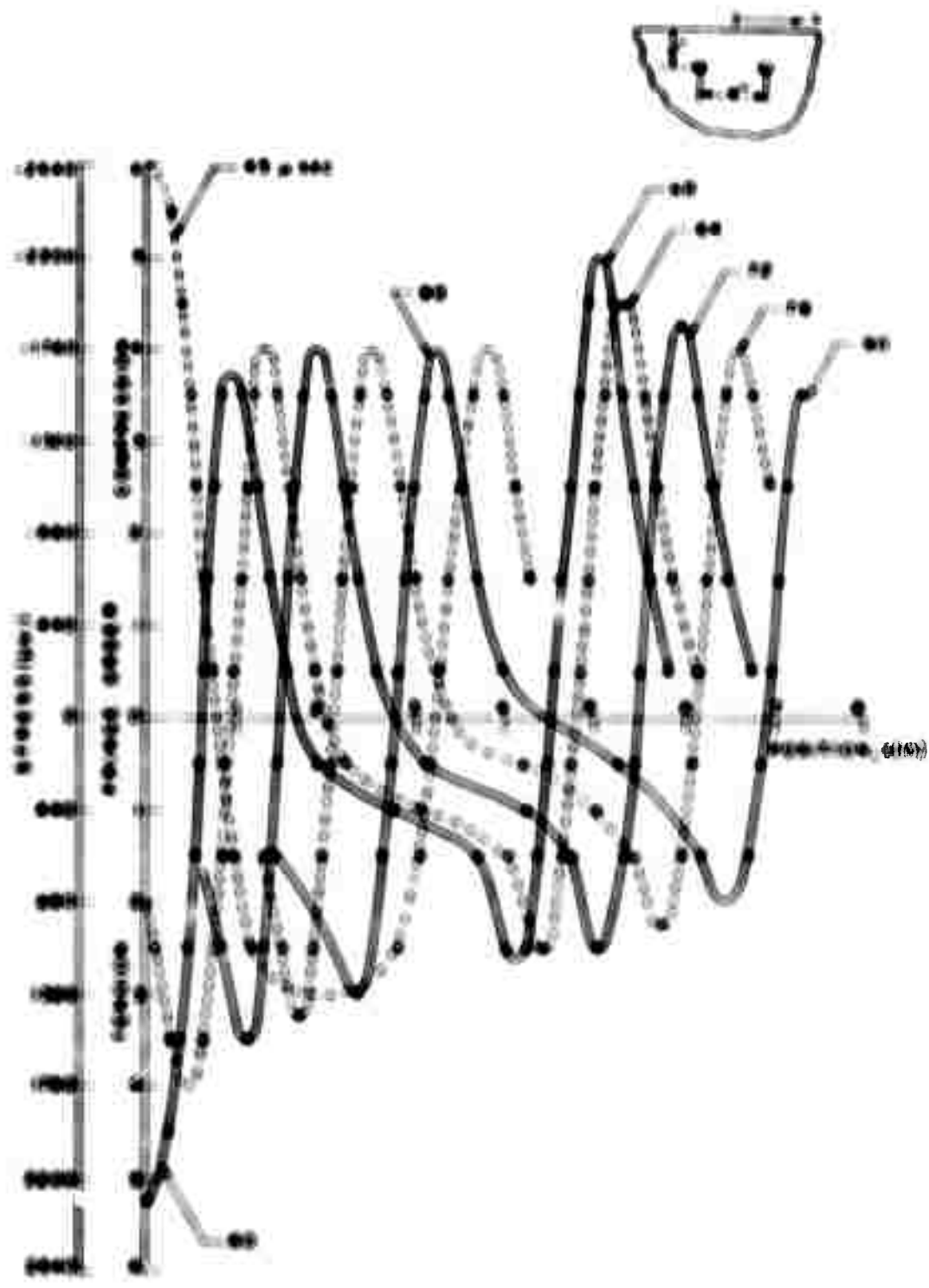


Figure 1. The variation of the amplitude of the oscillation with the frequency ω for different values of the parameter α . The curves are labeled with the values of α in the legend.

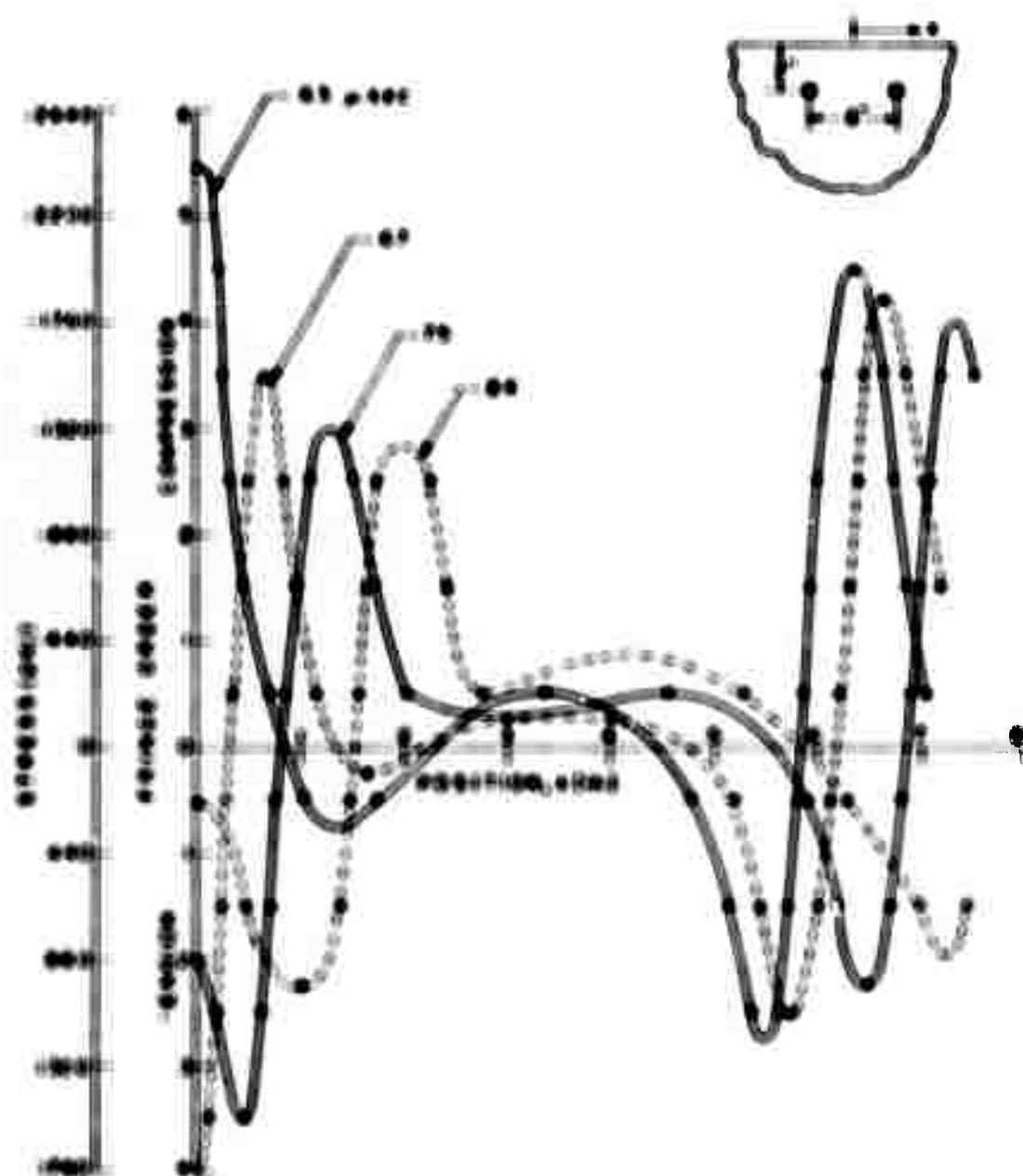


FIG. 1.30 FORCE (DYNES/CM²) AS A FUNCTION OF POSITION ALONG THE CATHETER FOR 197+0, 197+3.

influence of S/λ on this maximum stress (at the centerpoint on the boundary) is shown in Fig. 4.37. Although relatively high stresses occur for $S/\lambda = 3$ ($b/\lambda = 1$), utilization of explosive placement with $S/\lambda > 3$ is not recommended. First, fracture directly above the source will result early in the event from the P, PP interaction, and as a consequence all subsequent stresses will be relieved. Second, large values of S/λ will produce non-uniform fragmentation between the sources. While extensive fragmentation may occur above the sources and in the neighborhood near the vertical centerline, it is possible that significant zones may remain unbroken between these two locations.

For models with $b/\lambda = 2$, the variation in the maximum tensile stress on the boundary with the S/λ parameter is small. However, the boundary stresses indicated in Fig. 4.37 are much smaller for $b/\lambda = 2$ than those measured for $b/\lambda = 1$. An example of the distribution of stresses along the boundary is given in Fig. 4.38 for the model with $S/\lambda = 2$. The behavior is similar to what indicated previously; namely, two tensile pulses occur with a significant space between them. The trailing pulse is the important one since it occurs in the center zone between the charges.

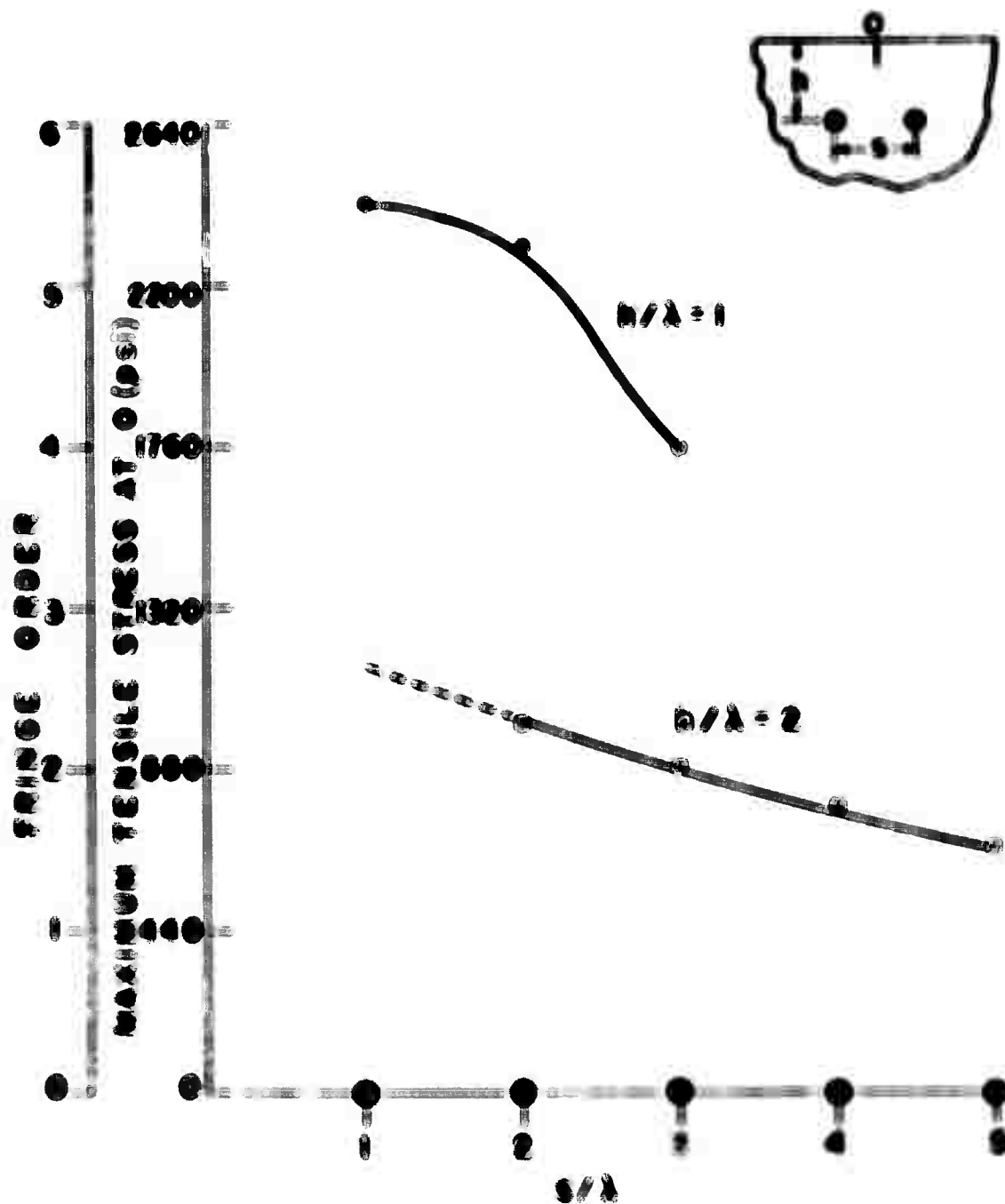
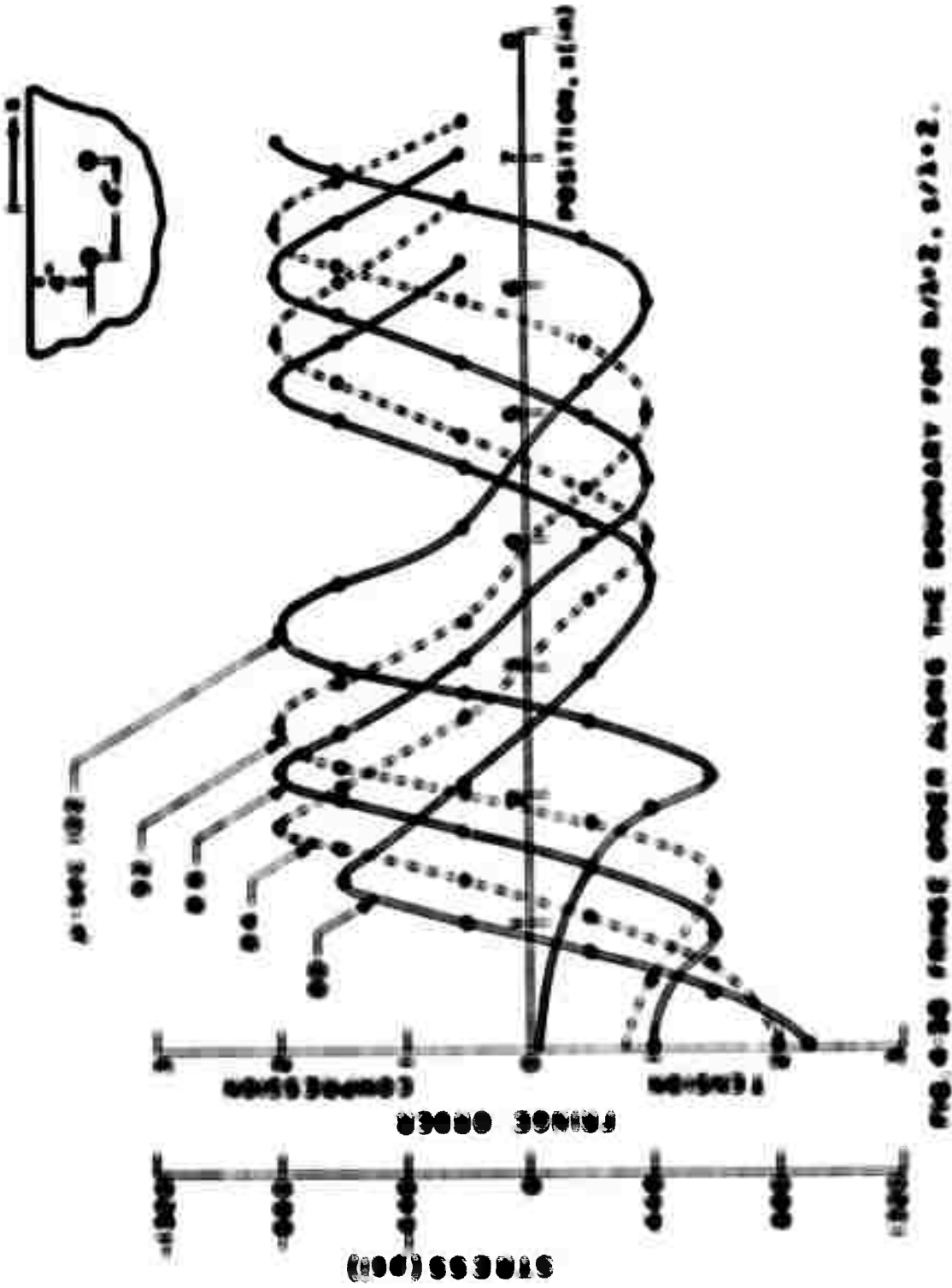


FIG. 8. Force Order vs. Maximum Tensile Stress at 0.195 for $h/\lambda = 1$ and $h/\lambda = 2$ on Maximum Stress



V. CONCLUSIONS AND RECOMMENDATIONS

Stress waves generated by multiple dilatational sources in a half-plane were examined in considerable detail by using dynamic photoelasticity. The primary contribution of the investigation was to improve the fundamental understanding of the complex stress wave interactions before, during and after the reflection process. The information obtained in the form of full-field fringe patterns permitted stress distributions to be established at discrete times during the dynamic event. These results in turn provide a foundation for further research work employing very brittle photoelastic models where the interaction between propagating cracks and stress waves can be examined.

In this investigation, several interactions between stress waves were noted which are important because they produce the tensile stress field that are essential in rock removal and rock fragmentation in surface mining operations. In the pre-reflection phase (before the stress wave reaches the free boundary), two important interactions were observed. The first occurred in the center region of the line joining the two sources when the tails (tensile) of the two incident dilatational waves P_1 and P_2 reinforce each other. These stresses are significant and in brittle materials can initiate bidirectional fracture between the sources. The second interaction occurred at four points in the field when the leading pulse P_1 (compression) combined with the tail pulse P_2 (tension) at locations where the respective orientation pro-

duced a high shear stress. These stresses should enhance the fragmentation process.

In the post reflection phase, three different stress wave interactions produced reinforcements near the boundary which were of considerable importance. These include: 1) the leading pulse in the PP wave with the trailing pulse in the P wave, 2) the P_L wave, the PP_R wave and the PS_R wave and 3) the PS_L and PS_R waves. The relative importance of these interactions depends on the spacing of the charges, indicated by the parameters h/λ and S/λ , as discussed extensively in Section 4. Two additional observations, both of which occur very late in the post-reflection period deserve mention. First, the PS wave moves into the shattered region around the sources producing sufficiently high stresses to re-initiate the radial cracks existing in this zone. Second, the wave resulting from the PS_L and PS_R combination moves down the vertical centerline into the region between the charges and should have a stress field sufficient to complete the fracture initiated previously by the reaction of the P_L and P_R tensile tails.

Two factors are of utmost importance in mining applications, namely rock removal and rock fragmentation. Both of these factors must be considered in selecting the optimum geometry of charge placement. Although this study does not permit conclusions to be drawn for placement of the charges in rock, suggestions can be made for further model studies where more brittle materials are used to fabricate the models.

Clearly, the greatest amount of rock can be removed at a minimum cost by increasing h/λ and S/λ to their maximum possible value consistent with a complete fracture along the charge line. The degree of fragmentation which occurs depends strongly upon h/λ and to a lesser degree on S/λ . The fragmentation results from scabbing failure, surface induced cracks due to tensile boundary stresses and the radial cracks emanating from the sources.

Fracture between the bore holes along the charge line is produced by three different occurrences at three different times during the dynamic event. First, the tensile tail of the incident P wave initiates radial cracks from the bore hole. Second, the reinforcement of the tensile tails in the P_R and P_L waves produce bi-directional cracking at the center region between the charges. Finally, the combined PS_L and PS_R waves move between the sources and ultimately complete the extension of the fracture between the sources. The P_L and P_R interaction is independent of h/λ but strongly dependent on S/λ . On the other hand the PS_L and PS_R interaction is strongly dependent on h/λ and only modestly influenced by S/λ . Thus it appears that further model studies directed toward establishing the most suitable parameters for rock removal should start with $h/\lambda = 2$ and $S/\lambda = 4$. Larger values of S/λ may be feasible in removing rock from the face, but uniformity in fragmentation of the product will be probably lost with $S/\lambda > 4$. Preliminary experiments with brittle materials (i.e., a

high ratio of compressive to tensile strength) may show little fragmentation, which will require reducing h/λ to say 1.5.

It is recommended that further investigation of this problem be conducted with a model material which is both brittle and birefringent. The birefringence will permit dynamic photoelasticity to be employed to investigate the stress wave propagation. The brittle model material will result in the development of fracture zones in regions of high tensile stresses. The growth of the fracture zones will be recorded simultaneously with the dynamic photoelastic patterns. As cracks develop in the model, these cracks present new boundaries to the stress waves and markedly affect the stress distributions in the later portion of the dynamic event.

Preliminary experiments conducted using plate glass indicate that it should serve quite well as a model material which is birefringent and brittle. Once optimization in terms of maximum material removal and uniform fragmentation has been accomplished on glass, model studies on various rocks should be conducted to establish the validity of these results.

It is noted that another series of experiments is currently being conducted by this research group where the stress wave is generated by a line load. The information obtained from this study will be combined with the results of the investigation recommended above to obtain practical

recommendations for optimizing rock removal and fragmentation by means of explosives.

APPENDIX A

FRINGE PATTERNS



FIG. 1. 2. 3. 4. 5. 6.

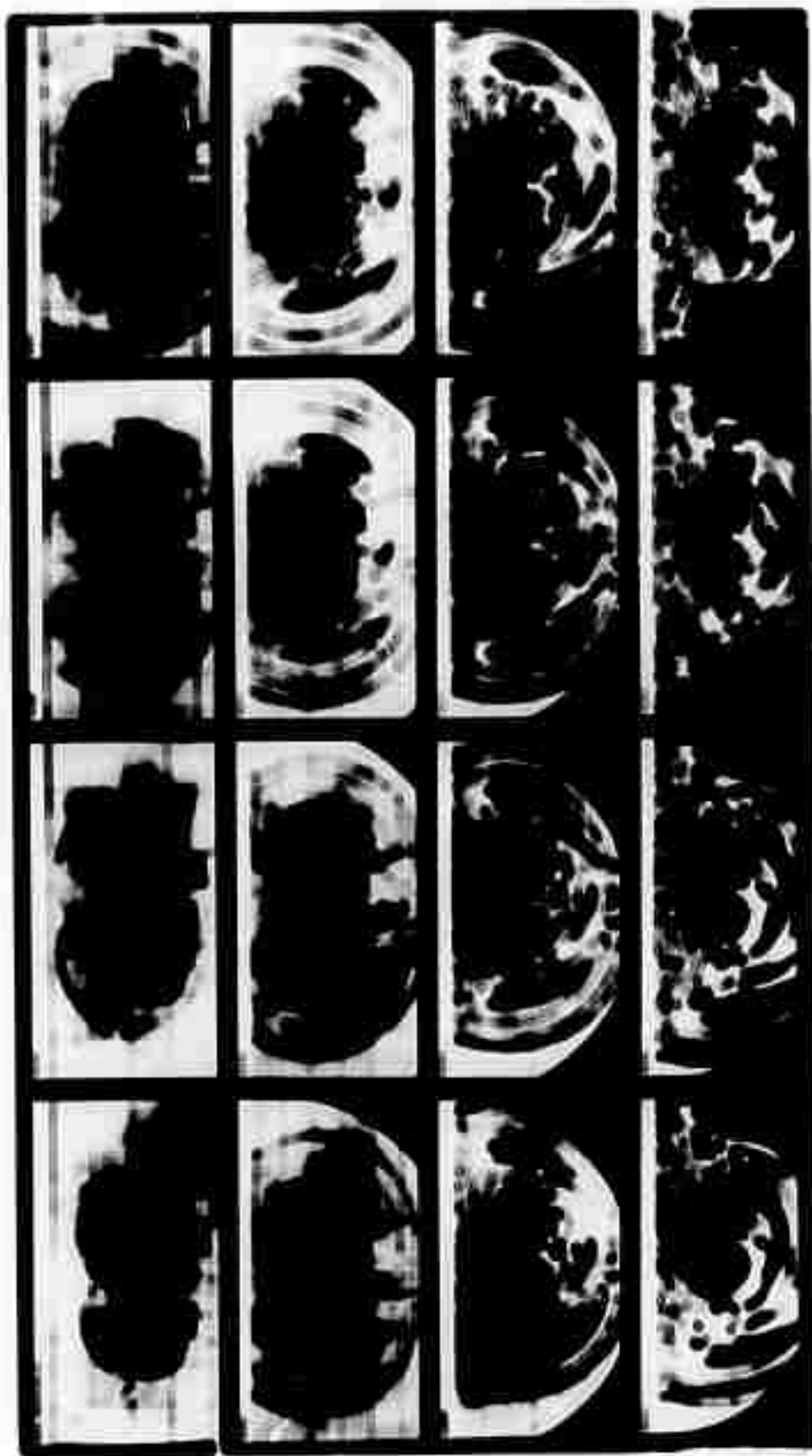


FIG. A-20 10-27-88

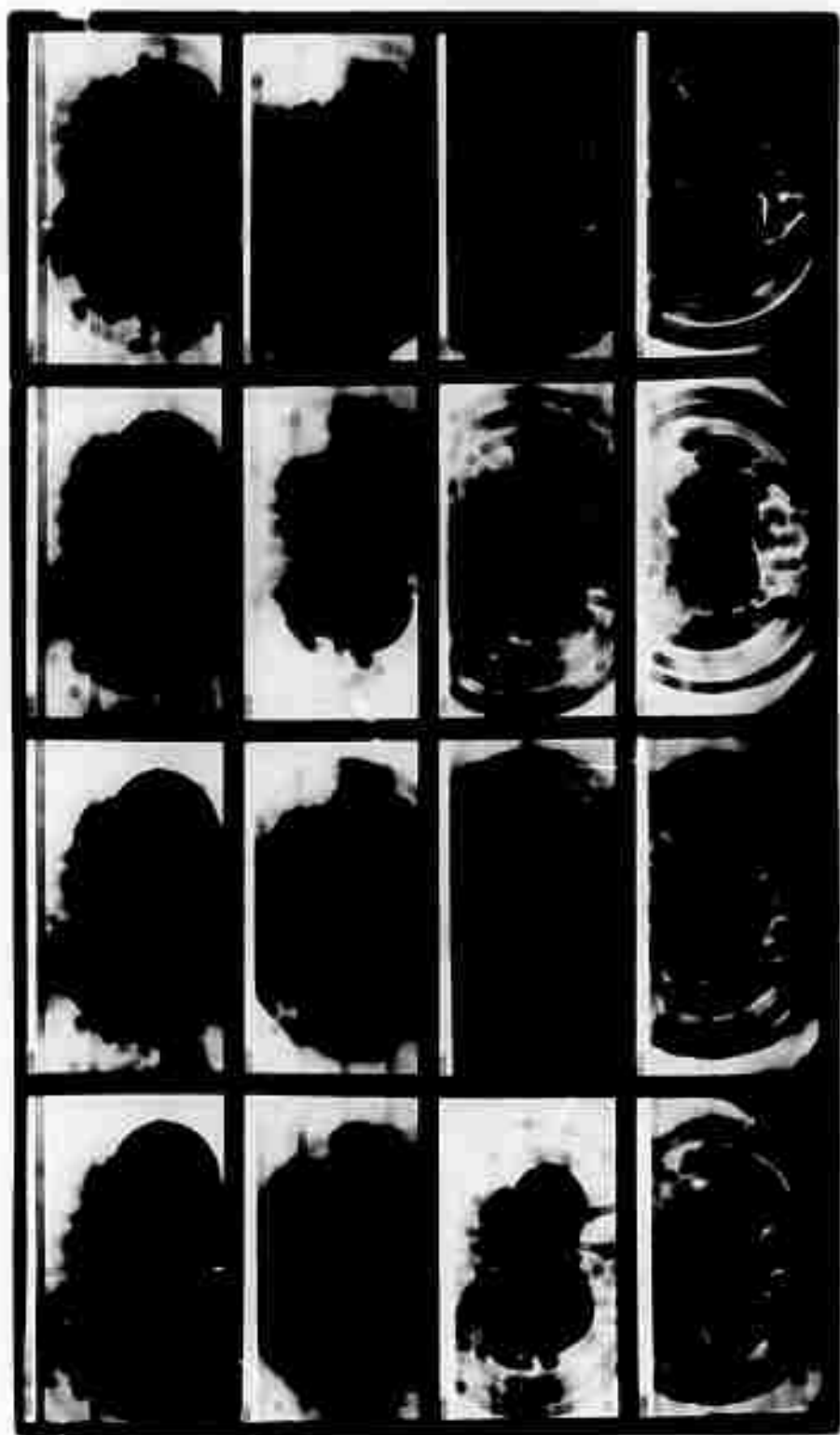


FIG. A-2b 40x 0.02



FIG. A-3 4-27 8-4

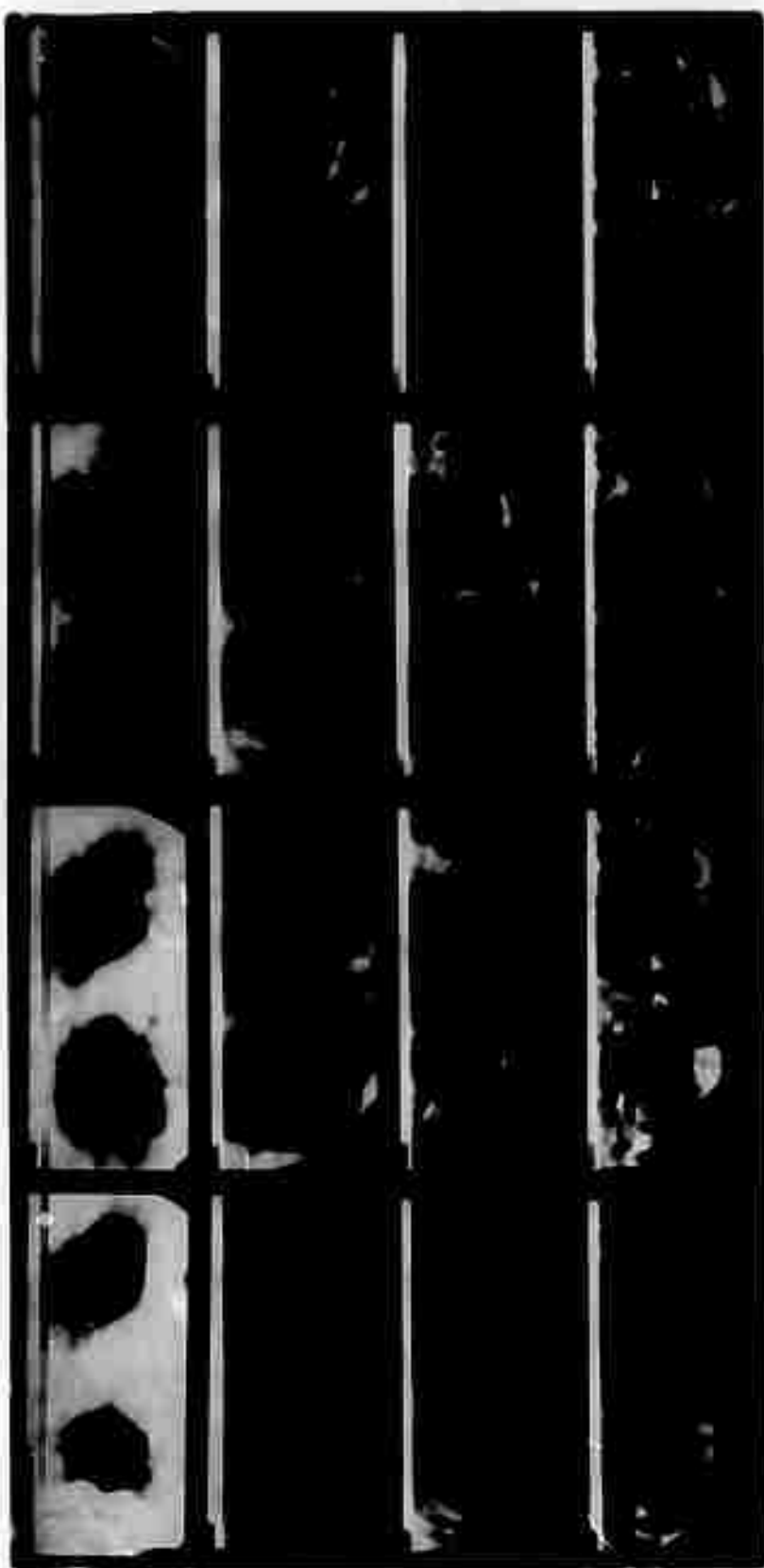


FIG. 2-4 4-2 4-6



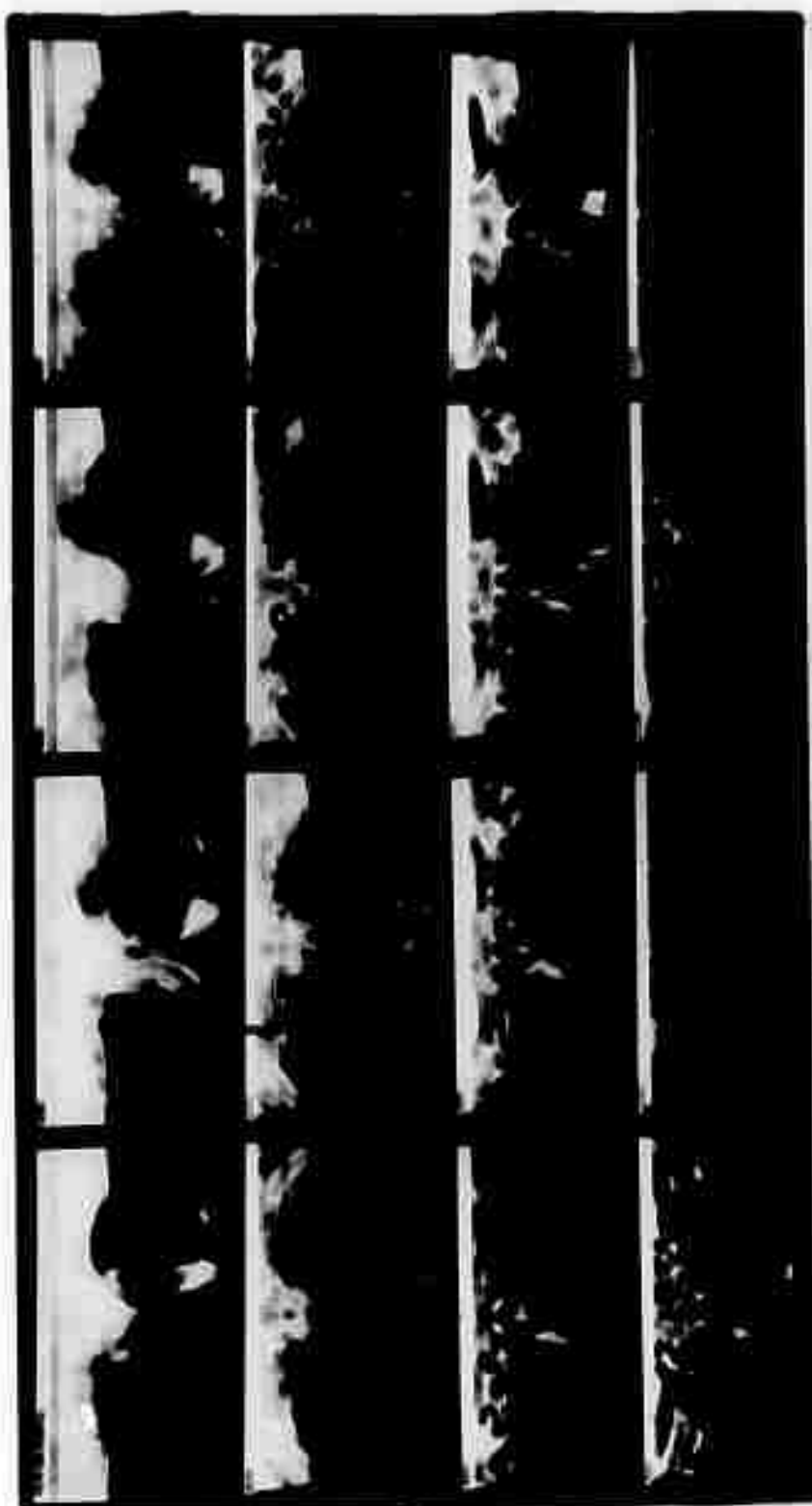
FIG. A-8 4-8 1-8



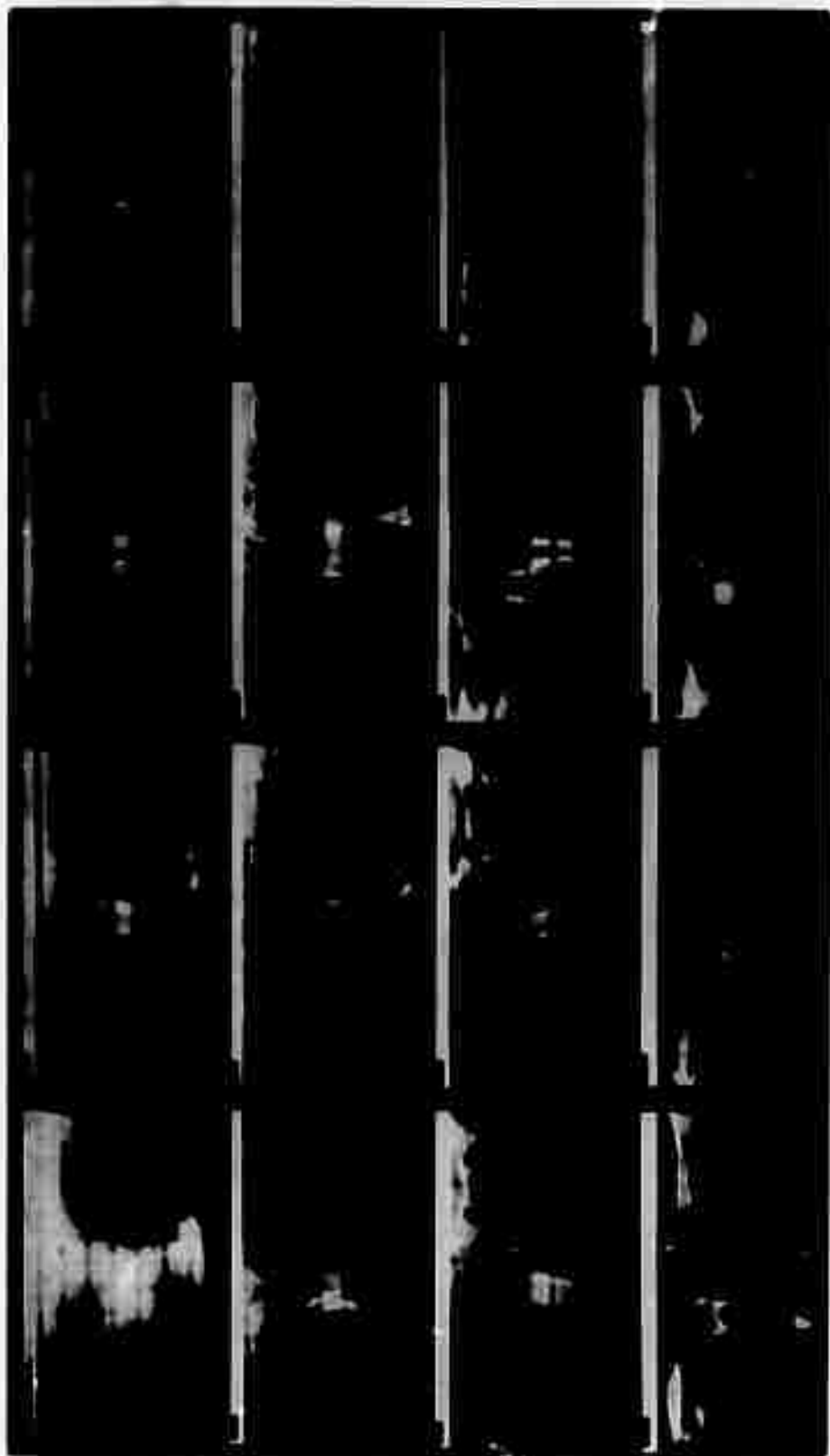
FIG. 2-6 1-1-1 1-1-1



FIG. A-7 h.c. s.c.



713 2-0 2-4 1-5



119 119 119

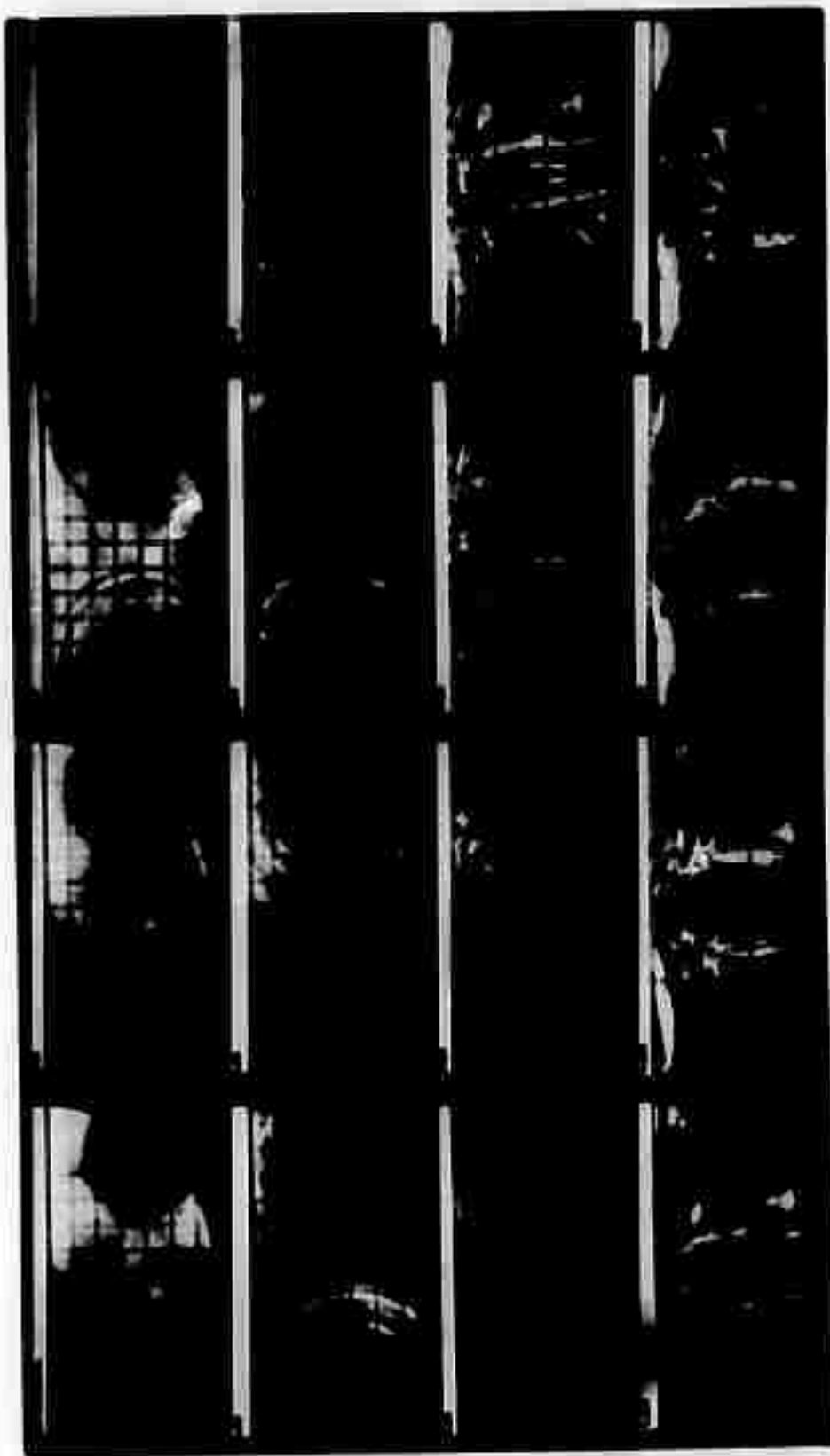


FIG. A-10 1-4 3-10



FIG. A-11 h-4 3-9-2

BIBLIOGRAPHY

- 1.1 Cook, M. A., The Science of High Explosives, ACS Monograph Series, Reinhold Publishing, New York, 1958.
- 1.2 Rinehart, J. S., "Fracturing Under Impulsive Loads", 3rd Symp. Mining Research, Bull. Univ. Missouri School of Mines and Met., 1958, p. 46-83 and "The Role of Stress Waves in the Comminution of Brittle Rocklike Materials", International Symp. on Stress Wave Prop. in Materials, Interscience Publishers, 1960, p. 247-270.
- 2.1 Clark, A. B. J., "Static and Dynamic Calibration of a Photoelastic Model Material - CR 39", Proc. SESA, Vol. 14, No. 1, (1956), p. 195.
- 2.2 Dally, J. W., and Thau, S. A., "Observations of Stress Wave Propagation in a Half-Plane with Boundary Loading", International Journal of Solids and Structures, Vol. 3, May 1967, pp. 293-308.
- 2.3 Dally, J. W., and Riley, W. F., "Stress Wave Propagation in a Half-Plane Due to a Transient Point Load", Developments in Theoretical and Applied Mechanics, Vol. 3, pp. 357-377.
- 2.4 Reinhardt, H. W., and Dally, J. W., "Dynamic Photoelastic Investigation of Stress Wave Interaction with a Bench Face", Trans. Soc. of Mining Engineers, AIME, Vol. 250, March 1971, pp 35-42.
- 3.1 Dally, J. W., and Riley, W. F., Experimental Stress Analysis, McGraw-Hill, New York, 1965, pp. 165-183.